Fluid infiltration and permeability enhancement by mid-crust fracturing during high grade metamorphism

Ph.D. dissertation

Fluid infiltration and permeability enhancement by mid-crust fracturing during high grade metamorphism

高度変成作用中の中部地殻の破壊による流体の浸透と透水率の増進

Tohoku University

Graduate School of Environmental Studies

Diana Mindaleva

August 2020

Contents

Chapter 1
Introduction

1. Introduction

1.1 Research background

Fluid flow in the crust induces mass and heat transport, enhances hydration reactions, modifies mechanical and rheological properties, and has an essential role in ore deposit formation, crustal deformation, and earthquake triggering (Fig. 1), (e.g., Ague, 1994; Cox, 1995; Fournier, 1991; Helgeson, 1964; Sibson, 1994). The timescale of fluid infiltration is a key parameter in understanding the physical processes of such fluid infiltration. Geological records of fluid infiltration range from millions of years for metamorphic devolatization reactions (e.g., Ague and Baxter, 2007; Pollington and Baxter, 2010; Taetz et al., 2018), ≤1 Myr for ore deposit formation (e.g., Goldfarb et al., 1991; Márton et al., 2010; Rohrlach and Loucks, 2005) to tens to hundreds of years for hydrothermal alteration of ophiolite (Beinlich et al., 2020). Analyses of vein systems have shown that a single vein can be related to much shorter timescales of fluid flow from ~200 yr to 1–4 months for eclogitic veins in blueschist (John et al., 2012; Taetz et al., 2018). Quartz veins in an accretionary prism have yielded sealing timescales of 6–60 yr (Saishu et al., 2017) and 1–5 yr (Ujiie et al., 2018).

Recent geophysical observations have revealed a relationship between cyclical fluid infiltration and tremors and slow slip events (e.g., Obara, 2002; Ohmi and Obara, 2002; Shelly et al., 2006). The periodic seismic cycles are explained by the accumulation of fluids, followed by an increase in fluid pressure, and subsequent fracturing. The fracturing enhances permeability and provides further fluid transport pathways leading to seismic events (e.g., Audet and Bürgmann, 2014; Nakajima and Uchida, 2018; Obara and Hirose, 2006; Ujiie et al., 2018; Warren-Smith et al., 2019). The recurrent cyclical fluid pressure increases and seismic events at the plate interface may be controlled by the permeability of the overlying crust (Audet and Bürgmann, 2014; Nakajima and

Uchida, 2018). As such, dynamic changes in the fluid pressure and permeability in the middle–lower crust are key to further understanding the relationship between fluid infiltration and fracturing.

The permeability of the crust exhibits large variations from 10^{-19} m^2 in areas of contact metamorphism (Hanson, 1995) to 10^{-18}–10^{-15} m^2 in geothermal–metamorphic areas (Ingebritsen and Manning, 2010). Recent studies of seismic clustering suggest that enhanced permeability can occur in the crust up to 10^{-15}–10^{-14} m^2 (e.g., Cox, 2016; Nakajima and Uchida, 2018; Okada et al., 2015).

Although there have been numerous *in situ* observations of permeability in the shallow crust (<4 km depth), such data for the middle–lower crust are limited. Manning and Ingebritsen (1999) constrained crustal permeability from analyses of metamorphic rocks. They estimated a Myr-scale "time-averaged permeability" from "time-integrated fluid flux" deduced from the chemical alteration of metamorphic rocks, which were classified according to the duration of metamorphism (1 Myr to ~10–100 Myr) and assumed fluid pressure gradients (i.e., between lithostatic and hydrostatic). Manning and Ingebritsen (1999) showed that the permeability of the ductile region of the crust (>10 km depth) is weakly dependent on depth and has an almost constant value of ~10^{-18} m^2. Higher values (~10^{-16} m^2) were estimated for fault zone metamorphism and metamorphism with pulses of thermal heating (Ingebritsen and Manning, 2010). However, constraints on the permeability of the lower and middle crust are still limited, apart from a few numerical (Saar and Manga, 2004), experimental (Shmonov et al., 2003), and natural metamorphic (Dipple and Ferry, 1992; Ingebritsen and Manning, 2010; Manning and Ingebritsen, 1999) studies at highly variable timescales. To understand fluid infiltration on timescales comparable with geophysical observations

(e.g., Nakajima and Uchida, 2018) it is necessary to constrain permeability changes in geological samples at timescales of ≤10 yr.

Mineral abbreviations follow after Whitney and Evans (2010).Fig. Fi

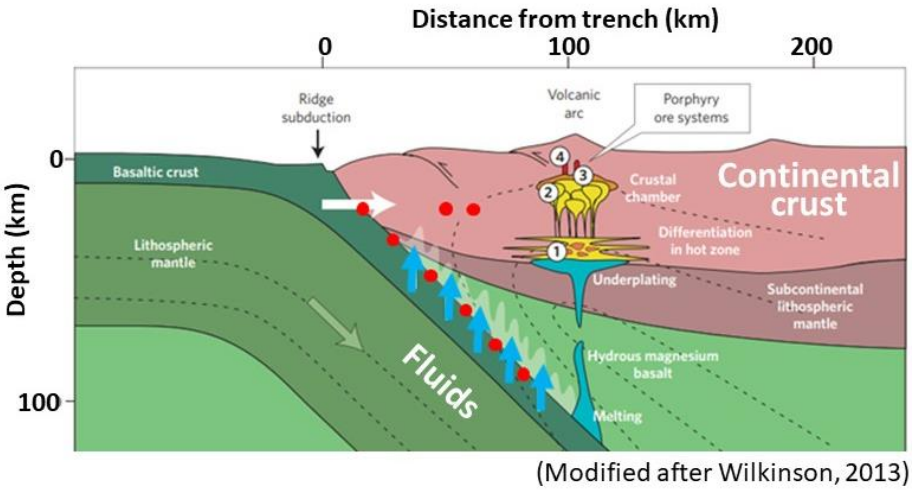

Fig.1 Fluid flow and related geological processes in the continental crust. Blue arrows show fluid infiltration. Red circles show earthquakes.

1.2 Objectives and thesis structure

To understand short, dynamic fluid processes within the crust it is necessary to constrain permeability from geological samples in short timescales. I provide first trial to estimate permeability based on metamorphic processes associated with crustal fractures and developed quantitative fluid infiltration model incorporating general relationships between mineral reactions, fluid flow and element mobilization during fluid–rock interaction.

This thesis consists of six chapters. Chapter 1 is introduction. Fluid flow in the crust responsible for changing of hydrological properties of rocks. Permeability, timescales of fluid infiltration and mass transfer within the crust are interconnected. Understanding about these properties is essential to understand about fluid flow within the crust. For this reason, in the Chapter 1 I introduce summary of previous studies. In the chapter 2 I provide information about geological settings, samples description, mineral chemistry, pressure-temperature conditions, and mass transfer during fluid infiltration. In this study I used samples from the Sør Rondane Mountains (SRM), East Antarctica. Samples are partially hydrated along fractures and hydrous reaction zones formed around fractures. These reaction zones are fingerprinting information about fluid infiltration and I analysed them to understand about mass transfer, fluid infiltration timescales (chapter 3) and permeability (chapter 4). In chapter 3 to constrain timescales of fluid infiltration I analysed fluid mobile elemental profiles and applied reactive transport model with local equilibrium. I further estimated wall rock and fractured crust permeability in chapter 4. To understand these properties I estimated fluid pressure gradient by thermodynamic modeling. Finally, I proposed fluid infiltration model in the crustal conditions in chapter 5. Chapter 6 is conclusion.

In this thesis, I provide unique estimate of lower–middle crustal permeability based on the metamorphic processes associated with crustal fractures. Metamorphic fluid–rock reaction zones along fractures provide geological evidence of fluid infiltration and crustal fracturing, and can be used to estimate fluid pressure gradients and permeability changes. Previous reactive transport analyses on reaction zones along fractures focused on estimation of timescales (John et al., 2012; Taetz et al., 2018) and/or material transfer (Ague and Baxter, 2007; Pollington and Baxter, 2010). However, permeability estimates were limited because of the lack of proper constraints on pressure gradients during the reactions. Thermodynamic analyses on the chemical activity of H_2O can constrain fluid pressures during metamorphic reactions (e.g., Goto and Banno, 1990; Anderson et al., 2005). I show that the combination of thermodynamic analyses of H_2O activity and reactive transport analyses enables permeability estimation on fluid-rock reaction zones.

My results provide unique geological evidence for rapid fluid infiltration in the crust within low-permeability rocks that was driven by a high fluid-pressure gradient.

Chapter 2
Hydration reactions and Cl-bearing fluid activities at middle–lower crustal conditions

2. Hydration reactions and Cl-bearing fluid activities at middle–lower crustal conditions

2.1 Introduction

Fluid activity in the crust induces mass and heat transport, enhances hydration reactions, modifies mechanical and rheological properties of rocks, and play an essential role in crustal deformation, and earthquake triggering (e.g., Ague, 1994; Cox, 1995; Fournier, 1991; Helgeson, 1964; Sibson, 1994). Fluid-rock hydration reactions form reaction zones around fluid pathways (fractures). Formation process is controlled by fluid infiltration pressure-temperature (P-T) conditions, fluid characteristics and host rock initial properties (e.g., Ague, 2011; Uno et al., 2014; Kleine et al., 2016).

Chlorine-bearing fluids have an important role in element fluid solubility, induce significant compositional and mineralogical changes, control mass transfer (e.g., Higashino et al., 2013; Kusebauch et al., 2015), and are excellent tracers of fluids in the crust. Abundant evidence for Cl-bearing fluids in the Sør Rondane Mountains (SRM) region of East Antarctica (e.g., Higashino et al., 2013, 2019a, b; Kawakami et al., 2017; Uno et al., 2017) makes this an ideal area to investigate crustal fluids.

In this chapter I investigated fluid–rock reaction zones in mafic granulite and orthopyroxene–hornblende (opx–hbl) schist samples from Mefjell, southern SRM, and in orthopyroxene–hornblende (opx–hbl) gneiss samples from Brattnipene, northern SRM, East Antarctica. I discuss hydration processes and fluid activity in the SRM. Clear mineralogical and chemical changes are observed in the fluid–rock reaction zones, which was used to analyze P-T conditions of fluid infiltration, mass transport and reaction progress. The implication of these results for Cl-bearing fluid activity at the crustal conditions are discussed.

2.2 Geological setting

The SRM (22°–28°E and 71.5°–72.5°S) were part of the collision zone between East and West Gondwana during the ca. 750–620 Ma East African–Antarctic Orogeny (Jacobs et al., 2003). The SRM are underlain by low- to high-grade metamorphic rocks and various syn-metamorphic intrusive rocks, which are divided into the northeastern (NE) and southwestern (SW) terranes by the Main Tectonic Boundary (Osanai et al., 2013) (Fig. 2).

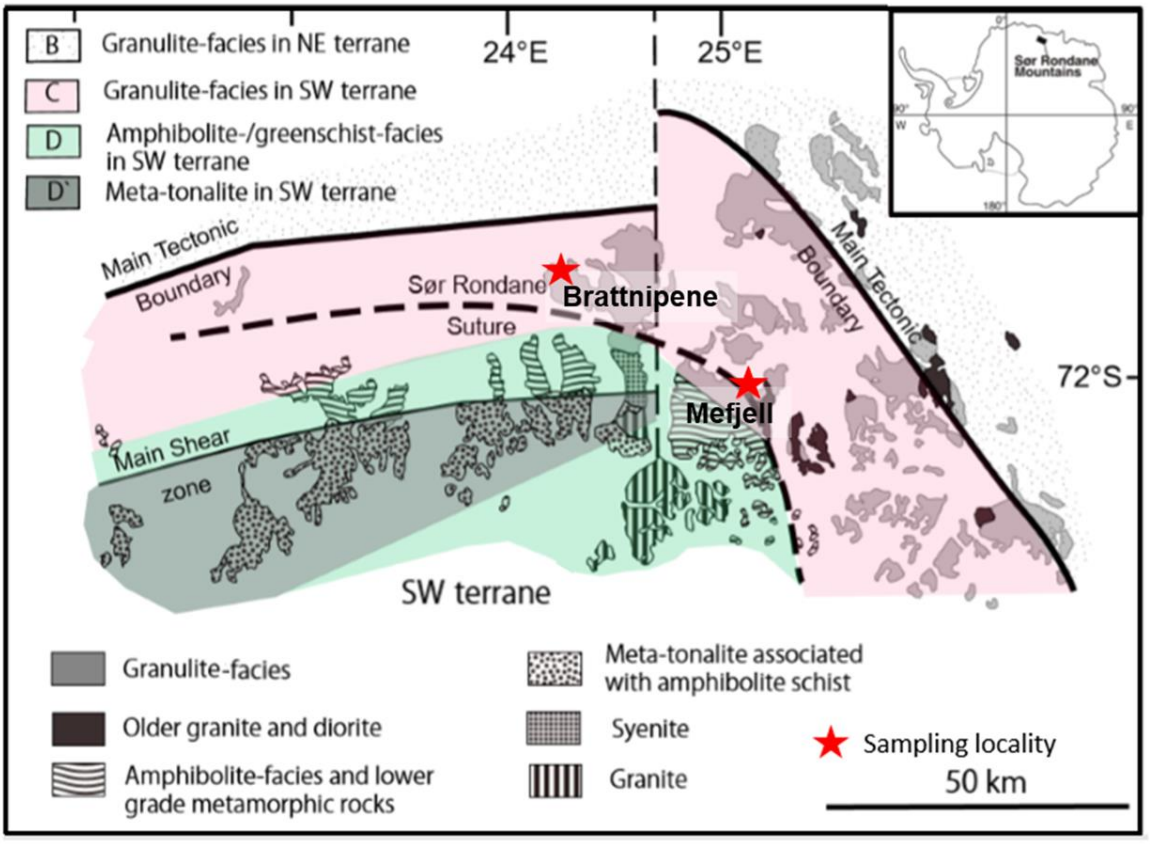

Fig. 2 Geological map of the Sør Rondane Mountains (modified after Ishikawa et al., 2013; Kawakami et al., 2017; Osanai et al., 1992, 2013; Shiraishi et al., 1997, 2008; Toyoshima et al., 2013). The main tectonic boundary is modified after Osanai et al. (2013) and Kawakami et al. (2017). The red stars are the sampling localities.

The NE terrane is composed of granulite-facies pelitic and psammitic rocks and intermediate igneous rocks, while the SW terrane is dominated by amphibolite- to greenschist-facies metamorphic rocks with intermediate to mafic compositions (Osanai et al., 2013; Shiraishi et al., 2008) (Fig. 2). Metamorphic rocks from the NE terrane have an oceanic affinity, whereas rocks from the SW terrane exhibit island or continental arc features (Osanai et al., 2013). In the southwestern part or SRM large east–west trending shear zone (Main Shear Zone) was defined (Kojima and Shiraishi, 1986). It was interpreted to be large-scale late Pan-African strike-slip structure formed around 560–530 Ma and it is an important tectonic boundary in the region (Ruppel et al., 2015).

The NE and SW terranes are subdivided into several units according to metamorphic grade. The NE terrane comprises amphibolite-facies (unit A) and granulite-facies rocks (unit B), and the SW terrane comprises granulite-facies (unit C) and amphibolite- to greenschist-facies rocks (units D and D`). Regional magmatism caused retrograde hydration in the SW terrane, where granulite-facies metamorphic rocks are overprinted by later amphibolite-facies metamorphism (e.g., Adachi et al., 2013; Baba et al., 2012; Osanai et al., 2013). Granulite-facies metamorphism occurred at ca. 650–600 Ma, and subsequent amphibolite-facies metamorphism occurred in both terranes at ca. 570 Ma (Fig. 4) (e.g., Asami et al., 2005; Shiraishi et al., 2008).

Mafic dykes with high K content and late-stage granitic and pegmatitic intrusions were observed and defines as post-tectonic dykes (e.g., Uno et al., 2017). Typical characteristics of oceanic, island arc, and continental margin arc settings was revealed from geochemical analysis of meta-basic igneous rocks in the SRM for some units (Osanai et al., 1992).

The samples used in this study were taken from unit C of the SW terrane (Fig. 2). Unit C is characterized by counter-clockwise *P–T* paths with initial *P–T* conditions of ca. 0.6–0.7 GPa and 800–900°C. Peak metamorphic conditions varied from 0.8–1.0 GPa and 750–900°C. After peak metamorphism, *P–T* conditions decreased to 0.8–0.9 GPa and 650–700°C. The final metamorphic event occurred at 0.2–0.3 GPa and 400–500°C (Fig. 4), (Adachi et al., 2013; Baba et al., 2012).

The Mefjell located in the central part of the SW terrane, SRM. The Mefjell complex consists of plutonic rocks, and forms part of the Sør Rondane Suture Zone. Previous studies (Li et al., 2005) suggested low oxygen fugacity conditions and high temperatures, some iron-rich hydrous mafic minerals and primary ilmenite was observed.

The Brattnipene located in the northern part of the SW terrane, SRM. Orthopyroxene widely distributed in the area. Biotite–hornblende, hornblende, and garnet–biotite gneisses was observed in the Brattnipene area, and these gneisses contain thin layers or blocks of garnet–sillimanite–biotite gneiss, amphibolite, pyroxene-granulite, marble, charnockite, andenderbite. Orthopyroxene-bearing granulite is sparse and occurs either as thin layers or blocks. Adachi et al. (2010) proposed that decomposition of orthopyroxene was controlled by the degree of hydration during retrograde metamorphism in the gneisses of the Brattnipene area.

Previous studies have documented that Cl-rich minerals (e.g., apatite, biotite, and hornblende) are present in felsic and mafic gneisses along large-scale shear zones and tectonic boundaries that extend over 200 km (Fig. 3), (Higashino et al., 2013, 2015, 2019a, b; Kawakami et al., 2017; Uno et al., 2017).

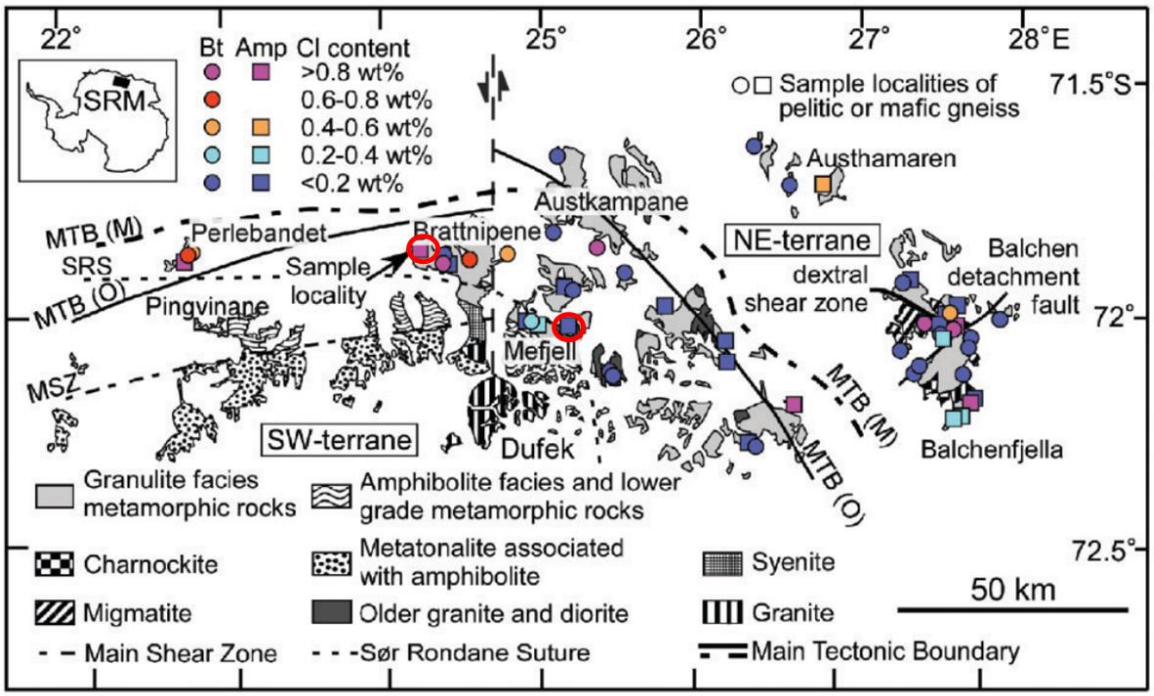

Fig. 3 Simplified geological map of the Sør Rondane Mountains (after Shiraishi et al., 2008) and the sample locations of metapelitic gneisses utilized in the determination of Cl concentration in biotite. The numbers in parentheses on the map represents the highest Cl concentration observed in each sample. PI stands for Pingvinane, L stands for Lunkeryggen, and M stands for Mefjell. SRS stands for the Sør Rondane Suture (Osanai et al., 1992). After Higashino et al., 2013.

Such Cl-rich minerals result from interaction with Cl-rich fluids or melts that were present at near-peak metamorphic conditions and/or in prograde and retrograde *P–T* conditions (Fig. 4) (e.g., Higashino et al., 2013, 2015, 2019a, b; Kawakami et al., 2017; Uno et al., 2017). Some of the Cl-rich fluids are likely to have been derived from mafic rocks (Higashino et al., 2019b) and from the slab and/or granitic magma below the crust (Uno et al., 2017).

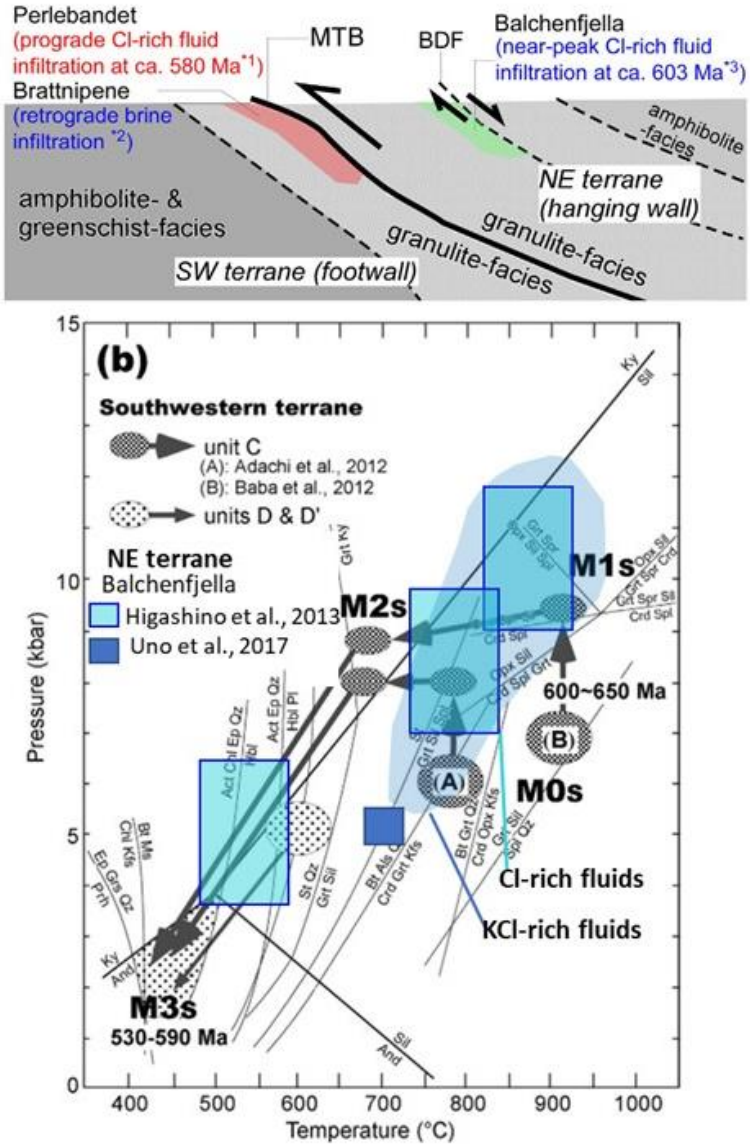

Fig. 4 Upper figure showing simplified tectonic model for the continental collision in the SRM, modified after Osanai et al. (2013). Chlorine-rich fluid infiltration in Brattnipene presumably took place at the under the uppermost part of the footwall of the MBT under the amphibolite and greenschist-facies conditions. After Kawakami et al., 2017. Down figure shows P-T path for the Southwestern terrane. Blue squares show Cl-rich and KCl-rich fluids infiltrations (Adachi et al., 2013; Baba et al., 2012; Higashino et al., 2013; Uno et al., 2017). Modified after Osanai et al. (2013).

Balchenfjella samples from the NE terrane (Higashino et al., 2013) indicates that Cl-rich fluids or melts infiltrated at 603 ± 14 Ma under ca. 800 ◦C and 0.8 GPa. Cl-rich biotite was observed in this samples. It suggested that biotite may have formed regionally under high-grade metamorphic conditions and Cl-rich fluids or melt infiltrated widely in the Sør Rondane Mountains near the peak metamorphism at ca. 600 Ma (Shiraishi et al., 2008). Fluids or melt infiltration during retrograde metamorphism was suggested for the eastern part of the Sør Rondane Mountains (Higashino et al., 2013). Several fluid infiltrations suggested for the Balchenfjella, which is located near large scale shear zone and could be possible fluids source. Brattnipene in the SW terrane is also located on a ductile shear zone and this shear zone also could be from where fluids came. However, fluid source could be possibly different.

In this study, I investigated samples collected during the 51st Japan Antarctic Research Expedition to Mefjell, SRM, East Antarctica (72.049°S and 25.152°E) in 2009–2010. The studied area comprises granulite-facies rocks of the SW terrane (unit C) located close to the Sør Rondane suture (Osanai et al., 1992), which is defined as the boundary between amphibolite-facies and lower grade metamorphic rocks and granulite-facies rocks in the SW terrane (Fig. 2). I investigated mafic granulite (121403A1 and 121403A2), opx–hbl schist samples (121403B, 121403B1, 121403B2) from Mefjell that are partially hydrated along fractures due to hydration reactions. The mafic granulite occurs adjacent to opx–hbl schist in outcrops (Fig. 5 a, b).

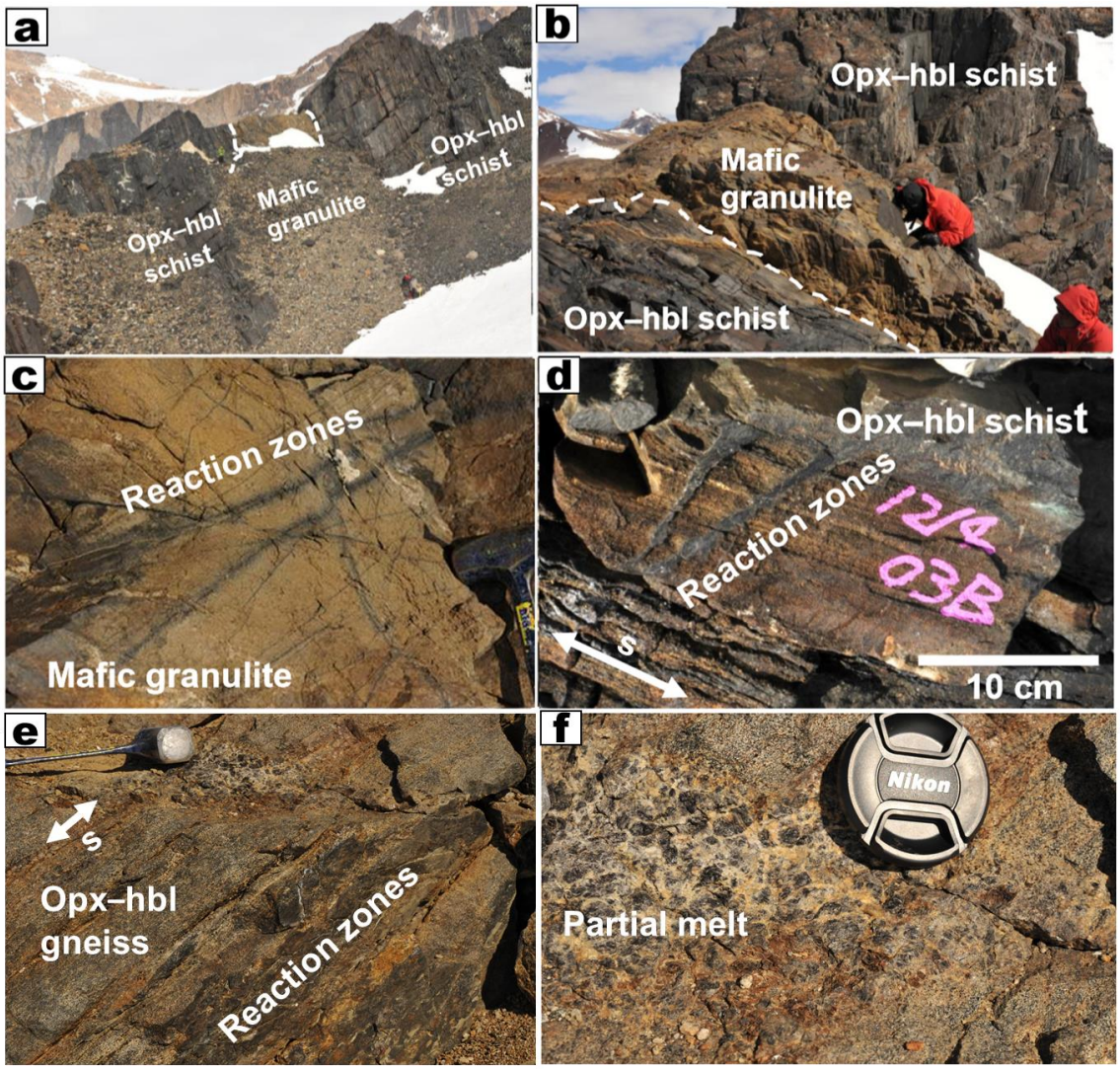

Fig. 5 Photographs of partly hydrated mafic granulite, opx–hbl schist and opx–hbl gneiss. White dashed lines indicate boundaries between mafic granulite and opx–hbl schist. (a) Mafic granulite and opx–hbl schist; (b) close-up of the boundary between mafic granulite and opx–hbl schist; (c) reaction zones in mafic granulite; (d) opx–hbl schist with the white arrow showing the schistosity; (e) reaction zones in the opx–hbl gneiss ; (f) close-up of the partial melt in the opx–hbl gneiss.

The mafic granulite is slightly foliated and is cut by numerous randomly oriented dark-colored reaction zones. The characteristic fracture length is 10–100 m. The width

of the reaction zones varies from several mm to 1–2 cm. In the opx–hbl schist, the schistosity is well developed and parallel to the lithological boundary with the mafic granulite. Dark-coloured reaction zones cut the host rock obliquely and are 10–100 m in length and 0.3–3.0 cm in width. These reaction zones are ubiquitous in the study area over an extent of 100 m to 1 km. Opx–hbl gneiss samples collected from Brattnipene (N09121001A, N09121001B, N09121001C, N09121001D, N09121001E) also partly hydrated or contain partial melt (Fig. 5 e, f). In the opx–hbl gneiss samples schistosity is well developed, reaction zones with different width from several mm to cm crosscut the schistosity. The characteristic length of the fracture is 10–100 m. Some samples (N09121001B, N09121001C, N09121001D,) consist light-colored partial melt with dark-colored inclusions. In the N09121001C sample reaction zone with 4 mm width is passing between partial melt and the host rock,

2.3 Analytical methods

Mineral compositions were determined using an electron probe microanalyzer (EPMA; JEOL JXA-8200) at the Graduate School of Environmental Studies, Tohoku University, Japan, using a 15 kV accelerating voltage and 12 nA beam current. The beam diameter was 3 μm for apatite and 1 μm for other minerals. SiO_2, TiO_2, Al_2O_3, FeO, MnO, MgO, CaO, Na_2O, K_2O, P_2O_5, Cr_2O_3, Cl, and F were analysed. The counting times for the peaks and backgrounds were 30 and 15 s for Cl and F, and 10 and 5 s for the other elements, respectively.

X-ray mapping by EPMA was conducted with a 15 kV accelerating voltage, 120 nA beam current, and dwell time of 20–30 ms. The beam diameter was 1 μm. For the reaction zones and host rock mafic granulite and opx–hbl schist, the X-ray maps were produced for areas that were 1000 × 400 and 1024 × 700 pixels in size, with a pixel size of 5 and 7 μm (Fig. 7). The mapped areas covered the entire region between the reaction zone and host rock in each sample. Mineral phases were identified by combining all the elemental maps using XMapTools (Lanari et al., 2014). Based on the mineral phase maps, modal mineralogy profiles were constructed.

The combination of the modal mineralogy profiles and mineral chemistry allowed elemental profiles to be constructed and used for the estimation of mass transport and water distribution within the reaction zones. H_2O contents along the reaction zone and in the host rock (c_{H_2O} g/cm^3) were determined from the H_2O contents and modes of hydrous minerals using the following equation: $c_{H_2O} = \sum_i M_i \frac{m_{H_2O} X_{H_2O}}{V_i}$, where M_i is the mineral mode expressed as a volume ratio, V_i (cm^3/mol) is the molar volume of hydrous mineral i, and m_{H_2O} (g/mol) is the molecular weight of H_2O. X_{H_2O} is the moles of H_2O per unit formula of hydrous mineral i, as constrained by stoichiometry.

Pseudosection analysis was undertaken to estimate the *P–T* conditions of the host rocks and water activities in the reaction zones. Pseudosections were calculated using Perplex X 6.8.5 (Connolly, 2009) in the Na–Ca–K–Fe–Mg–Al–Si–Ti–H_2O system with the hp02ver.dat dataset (Holland and Powell, 1998), and the internally consistent thermodynamic dataset and equation of state for H_2O of Holland and Powell (1998, revised 2004). Fluids are assumed to be pure H_2O. Bulk compositions used to constrain the pseudosections are listed in Table 1.

The following solid solution models were used: orthopyroxene (Holland and Powell, 1996), clinopyroxene (Holland and Powell, 1996), feldspar (Fuhrman and Lindsley, 1988), biotite (Powell and Holland, 1999), garnet (Holland and Powell, 1998), clinoamphibole (Wei and Powell, 2003), chlorite (Holland and Powell, 1998), epidote (Holland and Powell, 1998), olivine (Holland and Powell, 1998), anthophyllite, mica, brucite, spinel, talc, antigorite, stilpnomelane.

2.4 Petrography and mineral chemistry

Photomicrographs of the samples are shown in Fig. 6, and element maps (Fig. 7), modal mineralogies, and H_2O contents are shown in Fig. 8. Bulk chemical composition, mineral assemblage and mineral chemistry of the reaction zones are listed on Tables 1, 2 and 3, respectively. X_{Mg} was calculated as $X_{Mg} = Mg/(Mg + Fe)$.

The dark coloured reaction zones observed in outcrop correspond to pyroxene decomposition and the formation of amphiboles ± biotite, as described in detail below.

I defined the distance x along the reaction zone as the distance from the fracture centre towards the host rock in a direction perpendicular to the fracture.

Table 1 Bulk chemical composition (wt.%) of the reaction zones and host rock mafic granulite, opx–hbl schist, and opx–hbl gneiss samples.

Zone	*x* [mm]	SiO_2	TiO_2	Al_2O_3	FeO	MnO	MgO	CaO	Na_2O	K_2O	P_2O_5	Cr_2O_3	H_2O
Mafic granulite													
Reaction zone	<2	54.19	3.25	13.45	12.12	0.01	4.86	6.92	3.42	0.65	0.46	-	0.66
Host rock	>2	54.29	2.77	16.66	9.01	0.01	3.86	7.76	4.82	0.39	0.43	-	0.00
Opx–hbl schist													
Act–cum zone	<1.4	48.94	2.12	6.89	11.40	0.05	17.91	9.24	0.62	0.11	0.24	0.11	2.37
Act–opx zone	1.4–3	47.38	2.86	7.84	11.63	0.09	17.69	9.68	0.63	0.12	0.24	0.14	1.69
Host rock	>3	47.49	2.50	8.54	11.99	0.09	17.25	9.29	0.52	0.31	0.40	0.12	1.49
Opx–hbl gneiss													
Partial melt	<1.5	64.2	0.1	19.5	2.4	0.0	1.1	6.3	5.6	0.6	0.1	0.0	0.2
Reaction zone	1.5–5.5	49.0	0.8	15.3	13.0	0.0	6.7	9.1	2.9	1.8	0.0	0.0	1.3
Host rock	>5.5	49.2	0.5	18.1	11.5	0.0	5.5	8.3	4.3	1.4	0.3	0.0	0.9

Table 2 Mineral assemblages in the reaction zones and host rock mafic granulite, opx–hbl schist, and opx–hbl gneiss samples.

.

Zone	*x* [mm]	Qtz	Pl	Kfs	Bt	Mus	Zo	Act	Hbl	Prg	Cum	Cpx	Opx	Mag	Spl	Ilm	Chl	Stp	Brc-Serp	Ap
Mafic granulite																				
Reaction zone	<2	○	○	–	○	–	–	±	○	–	±	–	–	–	–	±	±	–	–	±
Host rock	>2	–	○	±	–	–	–	–	–	–	–	○	○	–	–	±	–	–	–	±
Opx–hbl schist																				
Act–cum zone	<1.4	–	–	–	–	–	–	○	○	–	○	–	–	±	–	±	–	±	±	±
Act–opx zone	1.4–3	–	–	–	–	–	–	○	○	–	–	–	○	–	±	±	–	–	–	±
Host rock	>3	–	±	–	–	±	±	–	○	–	–	±	○	–	±	±	–	–	–	±
Opx–hbl gneiss																				
Partial melt	<1.5	○	○	–	±	–	–	–	–	±	–	±	±	±	–	±	–	–	–	±
Reaction zone	1.5–5.5	±	○	–	±	–	–	–	–	○	±	–	±	±	–	±	–	–	–	±
Host rock	>5.5	±	○	–	±	–	–	–	–	±	–	○	○	±	–	±	–	–	–	±

○: present as a major component, ±: present as a minor component, –: not present, *x*: distance from the reaction zone or act–cum zone centre. Abbreviations: Qtz, quartz; Pl, plagioclase; Kfs, K-feldspar; Bt, biotite; Mus, muscovite; Zo, zoisite; Act, actinolite; Pgs, pargasite; Hbl, hornblende; Cum, cummingtonite; Cpx, clinopyroxene; Opx, orthopyroxene; Mag, magnetite; Spl, spinel; Ilm, ilmenite; Chl, chlorite; Stp, stilpnomelane; Brc–Serp, brucite–serpentine mixture; Ap, apatite.

Table 3 Representative compositions of minerals in the mafic granulite, opx–hbl schist, and opx–hbl gneiss samples.

Mineral	Pl						Kfs	Cpx					Zo
Sample	MG		Opx–hbl schist	Opx–hbl gneiss			MG	MG		Opx–hbl schist	Opx–hbl gneiss		Opx–hbl schist
Zone	R.zone	HR	HR	P.melt	R.zone	HR	HR	R.zone	HR	HR	P.melt	HR	HR
SiO_2	58.24	60.02	40.26	59.11	57.66	57.69	62.14	52.36	52.39	52.70	50.67	50.73	39.62
TiO_2	0.02	0.08	0.02	0.03	0.04	<0.01	0.03	0.20	0.06	0.28	0.26	0.28	0.02
Al_2O_3	26.44	25.24	32.90	25.47	25.62	26.37	18.49	0.87	0.47	1.28	2.52	2.51	32.28
FeO	0.12	0.04	0.27	0.22	0.41	0.16	0.19	12.58	12.23	6.72	12.65	12.00	0.97
MnO	<0.01	<0.01	0.08	<0.01	<0.01	0.05	n.d.	0.27	0.03	0.09	0.44	0.67	0.04
MgO	n.d.	<0.01	0.02	0.03	<0.01	0.02	n.d.	11.26	12.34	16.24	11.51	12.08	0.02
CaO	8.11	6.72	24.71	7.63	7.76	8.17	n.d.	21.81	22.32	22.72	21.09	20.85	24.15
Na_2O	6.72	7.53	0.16	6.83	7.10	7.10	0.57	0.28	0.15	0.03	0.52	0.59	n.d.
K_2O	0.17	0.41	<0.01	0.19	0.22	0.36	16.76	n.d.	n.d.	<0.01	0.02	n.d.	0.01
P_2O_5	n.d.	n.d.	0.01	0.05	n.d.	n.d.	n.d.	n.d.	n.d.	0.14	n.d	n.d.	0.01
Cr_2O_3	n.d.	n.d.	n.d.	n.d.	n.d.	n.d.	n.d.	0.01	0.03	n.d.	n.d	0.04	0.07
F	–	–	–	–	–	–	–	–	–	–	–	–	–
Cl	–	–	–	–	–	–	–	–	–	–	–	–	–
Total	99.81	100.05	98.45*	99.60	98.82	99.94	98.18	99.64	100.02	100.22	99.91	99.73	97.19
# of oxygens			8				8			6			12.5
Si	2.61	2.67	1.94	2.65	2.62		2.95	1.99	1.98	1.95	1.87	1.88	3.03
Ti	<0.01	<0.01	<0.01	<0.01	<0.01		<0.01	0.01	<0.01	0.01	0.01	<0.01	<0.01
Al	1.40	1.33	1.87	1.34	1.37		1.03	0.04	0.02	0.06	0.11	0.11	2.91
Fe^{3+}	–	–	–	<0.01	0.02		–	–	–	–	0.39	0.37	0.06
Fe^{2+}	<0.01	<0.01	0.01	<0.01	<0.01		<0.01	0.40	0.39	0.21	0.01	0.02	–
Mn	<0.01	<0.01	<0.01	<0.01	<0.01		n.d.	0.01	<0.01	<0.01	0.63	0.67	<0.01
Mg	n.d.	<0.01	<0.01	0.37	0.38		<0.01	0.64	0.70	0.89	0.84	0.83	<0.01
Ca	0.39	0.32	1.28	0.59	0.62		n.d.	0.89	0.91	0.90	0.04	0.04	1.98
Na	0.58	0.65	0.02	0.01	0.01		0.05	0.02	0.01	<0.01	<0.01	<0.01	n.d.
K	0.01	0.02	<0.01	<0.01	<0.01		1.02	n.d.	n.d.	<0.01	<0.01	n.d.	<0.01
P	n.d.	n.d.	<0.01	<0.01	n.d.		n.d.	n.d.	n.d.	<0.01	n.d	n.d.	<0.01
Cr	n.d.	n.d.	n.d.	n.d.	n.d.		n.d.	<0.01	<0.01	n.d.	n.d	n.d.	<0.01
F	–	–	–	–	–		–	–	–	–	–	–	–
Cl	–	–	–	–	–		–	–	–	–	–	–	–
Total cations	4.99	5.00	4.75	4.97	4.95		5.05	3.99	4.01	4.02	3.90	3.92	8.00
X_{Ab}	0.59	0.65	0.01	0.61	0.62	0.60	0.05						
X_{Mg}								0.61	0.64	0.81	0.64	0.62	
T [°C]	625				760				856			870	
P [GPa]													

n.d.: not detected, –: not analyzed, *: Total is low because of the very small grain width (<5 μm) of the analyzed region, **: Fe^{3+} in amphibole was calculated according to Holland and Blundy (1994).
Fugacity ratios of fluid are calculated based on Piccoli and Candela (1994) for apatite assuming P-T conditions of reaction zones.

Table 3 (continued)

Mineral	Opx							Bt				Mus
mple	MG		Opx–hbl schist		Opx–hbl gneiss			MG	Opx–hbl gneiss			Opx–hbl schist
Zone	R.zone	HR	Act–opx	HR	P.melt	R.zone	HR	R.zone	P.melt	R.zone	HR	HR
SiO_2	50.80	51.78	53.20	53.94	51.55	51.07	51.28	36.83	35.11	37.82	36.85	46.37
TiO2	0.13	0.09	0.09	0.04	0.12	0.11	0.08	4.57	1.84	0.74	3.88	0.04
Al_2O_3	0.46	0.22	1.61	1.39	0.99	1.12	1.20	15.01	15.81	15.57	14.59	38.13
FeO	31.08	31.94	19.82	19.70	27.07	27.11	27.82	21.60	21.58	15.05	16.37	0.43
MnO	0.54	0.01	0.14	0.29	1.81	1.82	1.17	0.14	0.05	0.10	<0.01	0.01
MgO	15.18	16.14	25.30	24.85	17.93	18.20	18.07	9.10	11.17	16.90	13.98	0.54
CaO	0.96	0.40	0.70	0.58	0.57	0.58	0.73	0.08	0.11	0.04	0.14	0.38
Na_2O	0.05	n.d.	n.d.	0.04	0.04	0.07	0.02	0.04	0.04	0.10	0.09	0.12
K_2O	0.02	n.d.	0.02	<0.01	<0.01	<0.01	<0.01	9.55	9.18	10.53	11.02	9.76
P_2O_5	n.d.	n.d.	0.10	0.03	0.02	<0.01	<0.01	0.03	0.04	<0.01	<0.01	0.10
Cr_2O_3	n.d.	0.02	0.01	0.12	<0.01	0.02	0.04	n.d.	0.03.	0.01	0.02	0.01
F	–	–	–	–	–	–	–	n.d.	0.49	1.12	1.02	–
Cl	–	–	–	–	–	–	–	0.10	0.90	0.50	0.04	–
Total	99.22	100.60	100.99	100.98	100.07	100.11	100.5	97.02	95.93	97.89	97.55	95.89
# of oxygens				6						22		22
Si	2.00	2.00	1.94	1.96	1.98	1.96	1.96	5.58	5.39	5.50	5.45	6.06
Ti	0.00	<0.01	<0.01	<0.01	<0.01	<0.01	<0.01	0.52	0.21	0.08	0.43	<0.01
Al	0.02	0.01	0.07	0.06	0.04	0.05	0.05	2.68	2.86	2.67	2.54	5.87
Fe^{3+}	–	–	–	–	–	0.87	–	–	–	–	–	–
Fe^{2+}	1.02	1.03	0.60	0.60	0.87	0.06	0.89	2.74	2.77	1.83	2.02	0.05
Mn	0.02	<0.01	<0.01	0.01	0.06	1.04	0.04	0.02	0.01	0.01	<0.01	<0.01
Mg	0.89	0.93	1.37	1.35	1.02	0.02	1.03	2.06	2.56	3.67	3.08	0.11
Ca	0.04	0.02	0.03	0.02	0.02	0.01	0.03	0.01	0.02	0.01	0.02	0.05
Na	<0.01	n.d.	n.d.	<0.01	<0.01	<0.01	<0.01	0.01	0.01	0.03	0.02	0.03
K	<0.01	n.d.	<0.01	<0.01	<0.01	<0.01	<0.01	1.85	1.80	1.95	2.08	1.63
P	n.d.	n.d.	<0.01	<0.01	<0.01	<0.01	<0.01	<0.01	0.01	<0.01	<0.01	0.01
Cr	n.d.	<0.01	<0.01	<0.01	<0.01	<0.01	<0.01	n.d.	<0.01	<0.01	<0.01	<0.01
F	–	–	–	–	–	–	–	n.d.	0.24	0.52	0.48	n.d.
Cl	–	–	–	–	–	–	–	0.02	0.23	0.12	0.01	n.d.
Total cations	3.99	3.99	4.02	4.01	4.00	4.01	4.01	15.49	16.10	16.39	16.14	13.81
X_{Ab}												
X_{Mg}	0.47	0.47	0.69	0.69	0.54	0.54	0.54	0.43	0.48	0.67	0.60	
T [°C]		856				870						
P [GPa]												

Table 3 (continued)

Mineral	Act		Hbl				Prg			Cum		
Sample	Opx–hbl schist		MG	Opx–hbl schist			Opx–hbl gneiss			MG	Opx–hbl schist	Opx–hbl gneiss
Zone	Act–cum	Act–opx	R.zone	Act–cum	Act–opx	HR	P.melt	R.zone	HR	R.zone	Act–cum	R.zone
SiO_2	53.83	55.91	45.37	46.57	47.09	47.05	39.96	40.37	42.17	54.09	52.22	50.62
TiO_2	0.18	0.10	0.36	1.38	1.54	1.40	1.20	1.14	1.59	0.01	0.14	0.03
Al_2O_3	3.13	1.33	9.28	10.84	9.57	9.95	12.48	13.04	11.21	0.67	3.73	1.06
FeO	7.54	5.45	18.15	7.92	8.29	8.47	20.10	18.56	15.75	25.77	14.25	27.12
MnO	n.d.	n.d.	0.13	n.d.	0.08	0.09	0.25	0.20	<0.01	0.38	n.d.	0.66
MgO	20.79	21.38	9.67	16.03	16.31	16.14	8.35	8.78	10.82	16.04	20.99	17.41
CaO	10.93	12.39	11.29	12.11	11.79	12.13	11.30	11.64	11.90	1.49	3.37	0.59
Na_2O	0.31	0.11	0.73	0.84	0.85	0.84	1.31	1.18	1.01	<0.01	0.42	<0.01
K_2O	n.d.	n.d.	0.75	0.15	0.17	0.71	2.42	2.65	2.05	0.02	0.04	0.03
P_2O_5	0.04	0.01	n.d.	0.06	n.d.	0.03	<0.01	0.04	<0.01	n.d.	n.d.	n.d.
Cr_2O_3	0.05	0.04	0.05	0.22	0.18	0.20	<0.01	0.02	<0.01	n.d.	0.02	n.d.
F	–	–	–	–	–	–	0.61	0.17	0.47	–	–	–
Cl	–	–	–	–	–	–	1.71	1.37	0.02	–	–	–
Total	96.80	96.73	95.78	96.12	95.86	96.99	99.04	98.77	96.80	97.48	95.19	97.52
# of oxygens	23**			23**				23**			23**	
Si	0.52	7.81	6.88	6.68	6.78	6.74	6.20	6.20	6.43	7.93	7.53	7.61
Ti	7.54	0.01	0.04	0.15	0.17	0.15	0.14	0.13	0.18	<0.01	0.01	<0.01
Al	0.02	0.22	1.66	1.83	1.62	1.68	2.28	2.36	2.01	0.12	0.63	0.19
Fe^{3+}	0.34	0.14	0.30	0.36	0.39	0.28	–	–	–	0.01	0.26	–
Fe^{2+}	0.55	0.50	2.00	0.60	0.62	0.74	2.61	2.39	2.01	3.15	1.47	3.41
Mn	n.d.	n.d.	0.02	n.d.	0.01	0.01	0.03	0.03	<0.01	0.05	n.d.	0.08
Mg	4.34	4.45	2.19	3.43	3.50	3.45	1.93	2.01	2.46	3.51	4.51	3.90
Ca	1.64	1.85	1.83	1.86	1.82	1.86	1.88	1.92	1.94	0.23	0.52	0.09
Na	0.08	0.03	0.21	0.23	0.24	0.23	0.39	0.35	0.30	<0.01	0.12	<0.01
K	n.d.	n.d.	0.14	0.03	0.03	0.13	0.48	0.52	0.40	<0.01	0.01	<0.01
P	<0.01	<0.01	n.d.	0.01	n.d.	<0.01	<0.01	<0.01	<0.01	n.d.	n.d.	n.d.
Cr	0.01	<0.01	0.01	0.03	0.02	0.02	<0.01	<0.01	<0.01	n.d.	<0.01	n.d.
F	–	–	–	–	–	–	0.30	0.08	0.23	–	–	–
Cl	–	–	–	–	–	–	0.45	0.36	0.01	–	–	–
Total cations	15.05	15.02	15.28	15.19	15.18	15.30	15.95	15.91	15.73	15.00	15.08	15.30
X_{Ab}												
X_{Mg}	0.83	0.87	0.49	0.78	0.78	0.77	0.43	0.46	0.55	0.53	0.72	0.53
T [°C]			625					760				
P [GPa]			0.52					0.62				

Table 3 (continued)

Mineral	Mag	Spl	Ilm		Stp	Ap						
Sample	Opx–hbl schist	Opx–hbl schist	MG	Opx–hbl schist	Opx–hbl schist	MG		Opx–hbl schist			Opx–hbl gneiss	
Zone	Act–cum	HR	R.zone	Act–cum	Act–cum	R.zone	HR	Act–cum	Act–opx	HR	R.zone	HR
SiO_2	n.d.	n.d.	<0.01	0.08	43.37	0.15	0.27	0.10	0.07	0.01	n.d.	0.22
TiO_2	0.52	0.01	52.51	53.03	0.04	0.04	0.01	0.01	n.d.	0.02	0.06	n.d.
Al_2O_3	2.63	62.23	n.d.	0.06	1.43	0.02	n.d.	0.01	0.02	n.d.	n.d.	n.d.
FeO	81.00	24.19	45.70	43.91	26.82	0.32	0.11	0.24	0.19	0.30	0.04	0.06
MnO	0.08	0.06	0.80	0.27	0.18	0.06	n.d.	0.03	0.10	0.03	0.13	n.d.
MgO	0.47	10.46	0.10	2.77	8.31	0.01	0.06	n.d.	0.04	0.06	n.d.	0.01
CaO	0.04	0.17	0.03	0.04	1.86	53.70	54.86	53.45	54.15	54.41	55.42	55.62
Na_2O	n.d.	n.d.	0.07	n.d.	n.d.	0.01	n.d.	0.07	0.13	0.04	n.d.	n.d.
K_2O	n.d.	0.01	n.d.	n.d.	0.07	0.02	0.02	n.d.	n.d.	n.d.	n.d.	0.02
P_2O_5	n.d.	n.d.	n.d.	n.d.	0.02	41.10	41.29	41.18	42.51	41.85	41.88	40.96
Cr_2O_3	6.01	n.d.	<0.01	0.20	n.d.	0.01	n.d.	n.d.	n.d.	n.d.	n.d.	0.01
F	n.d.	–	n.d.	n.d.	n.d.	3.31	3.87	1.36	2.02	2.06	2.63	3.74
Cl	n.d.	–	n.d.	n.d.	n.d.	0.14	0.08	1.71	0.45	0.24	0.61	0.10
Total	90.75	97.13	99.21	100.36	82.73	97.44	98.92	97.19	98.72	98.11	99.52	99.14
# of oxygens	4	4	3			12.5						
Si	n.d.	n.d.	<0.01	<0.01		0.01	0.02	0.01	0.01	<0.01	n.d.	0.02
Ti	0.02	<0.01	1.00	0.98		<0.01	<0.01	<0.01	n.d.	<0.01	<0.01	n.d.
Al	0.12	2.01	n.d.	<0.01		<0.01	n.d.	<0.01	<0.01	n.d.	n.d.	n.d.
Fe^{3+}	1.66	–	–	–		–	–	–	–	–	–	–
Fe^{2+}	0.98	0.55	0.97	0.89		0.02	0.01	0.02	0.01	0.02	<0.01	<0.01
Mn	<0.01	<0.01	0.02	0.01		<0.01	n.d.	<0.01	0.01	<0.01	0.01	n.d.
Mg	0.03	0.43	<0.01	0.10		<0.01	0.01	n.d.	<0.01	0.01	n.d.	<0.01
Ca	<0.01	0.01	<0.01	<0.01		4.91	4.96	4.90	4.84	4.91	4.97	5.04
Na	n.d.	n.d.	<0.01	n.d.		<0.01	n.d.	0.01	0.02	0.01	n.d.	n.d.
K	n.d.	<0.01	n.d.	n.d.		<0.01	<0.01	n.d.	n.d.	n.d.	n.d.	<0.01
P	n.d.	n.d.	n.d.	n.d.		3.01	2.99	3.02	3.04	3.02	3.00	2.97
Cr	0.19	n.d.	<0.01	<0.01		<0.01	n.d.	n.d.	n.d.	n.d.	n.d.	<0.01
F	n.d.	–	n.d.	n.d.		0.89	1.03	0.37	0.53	0.55	0.70	1.00
Cl	n.d.	–	n.d.	n.d.		0.02	0.01	0.25	0.06	0.03	0.09	0.01
Total cations	3.00	3.00	2.00	2.00		7.97	7.99	7.96	7.94	7.97	7.99	8.03
$log(f_{HCL}/f_{H2O})$						-3.35		-3.67	-4.32		-2.69	
X_{Mg}	0.03	0.44	<0.01	0.10								
T [°C]	438											
P [GPa]												

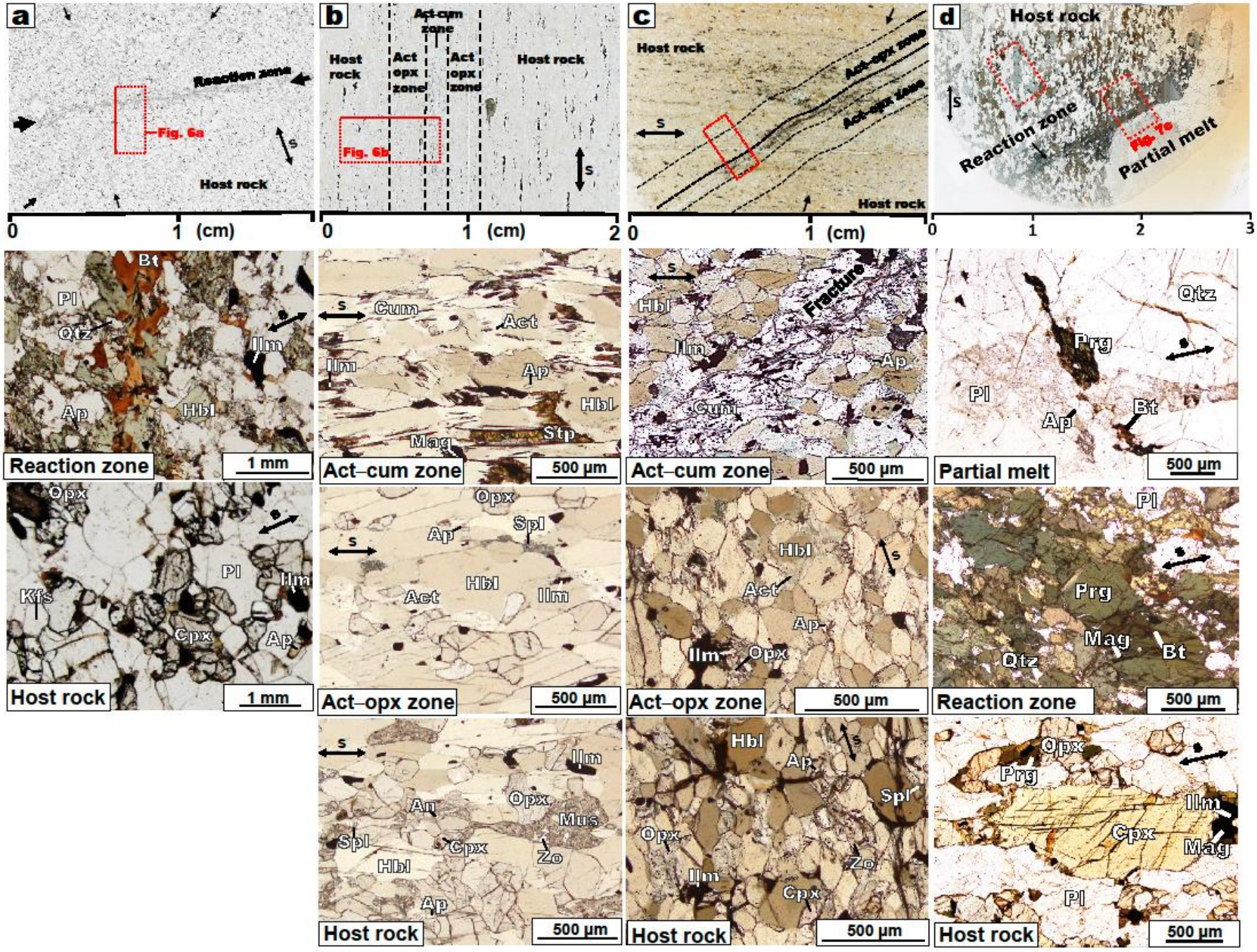
a
Reaction zone
Fig. 6a
Host rock
s
0
1 (cm)
b
Act-cum zone
Host rock
Act opx zone
Act opx zone
Host rock
Fig. 6b
s
0
1 (cm)
2
c
Host rock
Act-opx zone
Act-opx zone
s
Host rock
0
1 (cm)
d
Host rock
s
Reaction zone
Fig. 7c
Partial melt
0
1
2
3
Bt
Pl
Qtz
Ilm
Ap
Hbl
Reaction zone
1 mm
s
Cum
Act
Ilm
Ap
Hbl
Mag
Stp
Act–cum zone
500 μm
s
Hbl
Fracture
Ilm
Ap
Cum
Act–cum zone
500 μm
Qtz
Prg
Pl
Ap
Bt
Partial melt
500 μm
Opx
Pl
Ilm
Kfs
Cpx
Ap
Host rock
1 mm
Opx
Spl
Ap
s
Hbl
Act
Ilm
Act–opx zone
500 μm
Hbl
Act
Ap
Ilm
Opx
Act–opx zone
500 μm
Pl
Prg
Mag
Bt
Qtz
Reaction zone
500 μm
s
Ilm
Ap
Opx
Mus
Spl
Cpx
Zo
Hbl
Ap
Host rock
500 μm
Hbl
Ap
s
Spl
Opx
Zo
Ilm
Cpx
Host rock
500 μm
Opx
Prg
Ilm
Cpx
Mag
Pl
Host rock
500 μm

Fig. 6 Thin-section scans and photomicrographs of (a) mafic granulite; (b) opx–hbl schist (normal to schistosity and parallel to lineation); (c) opx–hbl schist (normal to schistosity and lineation); (d) opx–hbl gneiss showing mineralogical and microstructural changes in the reaction zones and host rocks with increasing extent of hydration. Arrows with "s" indicate schistosity. Red dotted squares indicate the elemental areas maps.

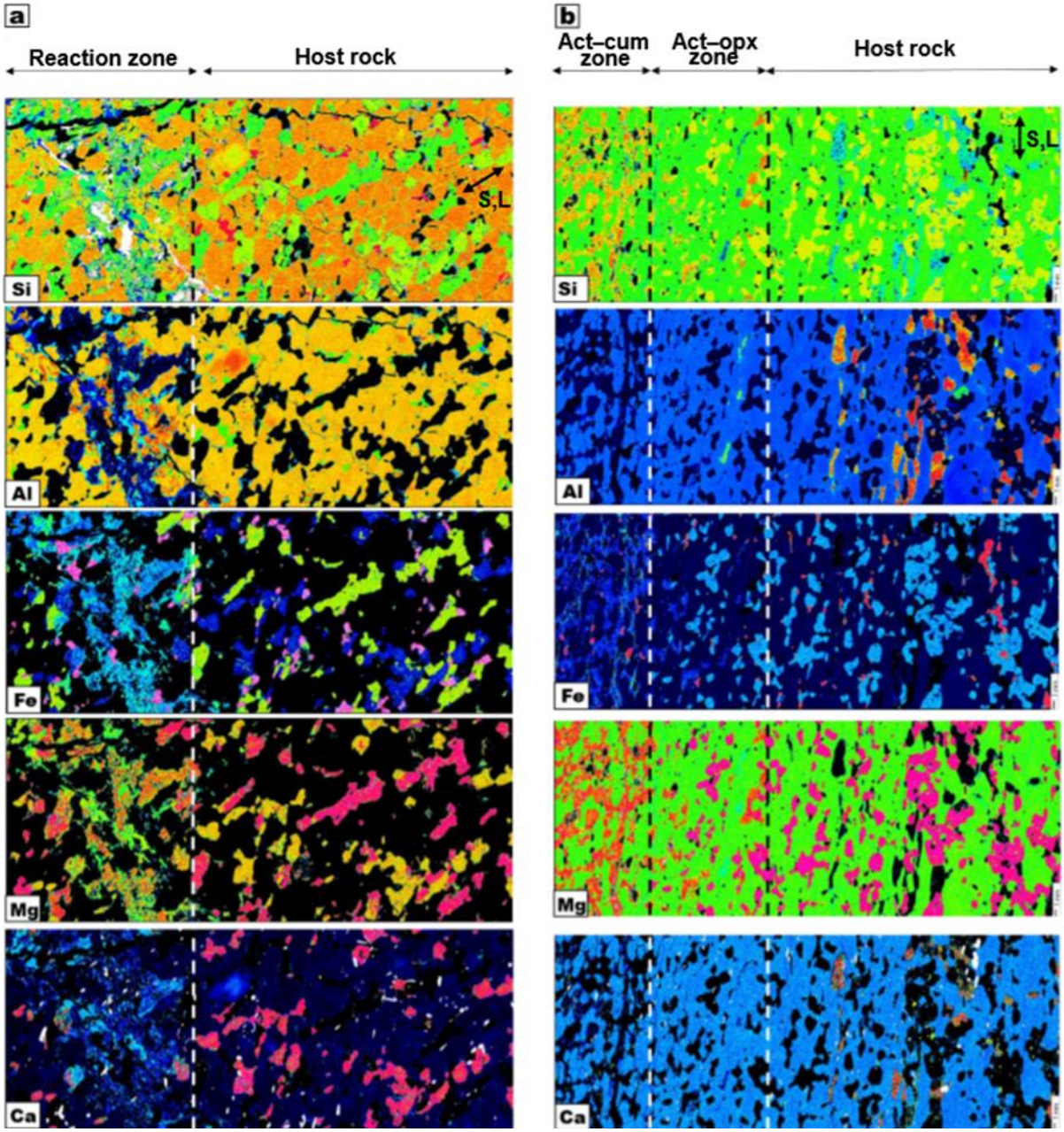

Fig. 7 Si, Al, Fe, Mg, Ca elemental map of (a) mafic granulite and (b) opx–hbl schist showing a clear difference between reaction zones and host rock. Arrows with "S, L" indicate schistosity and lineation.

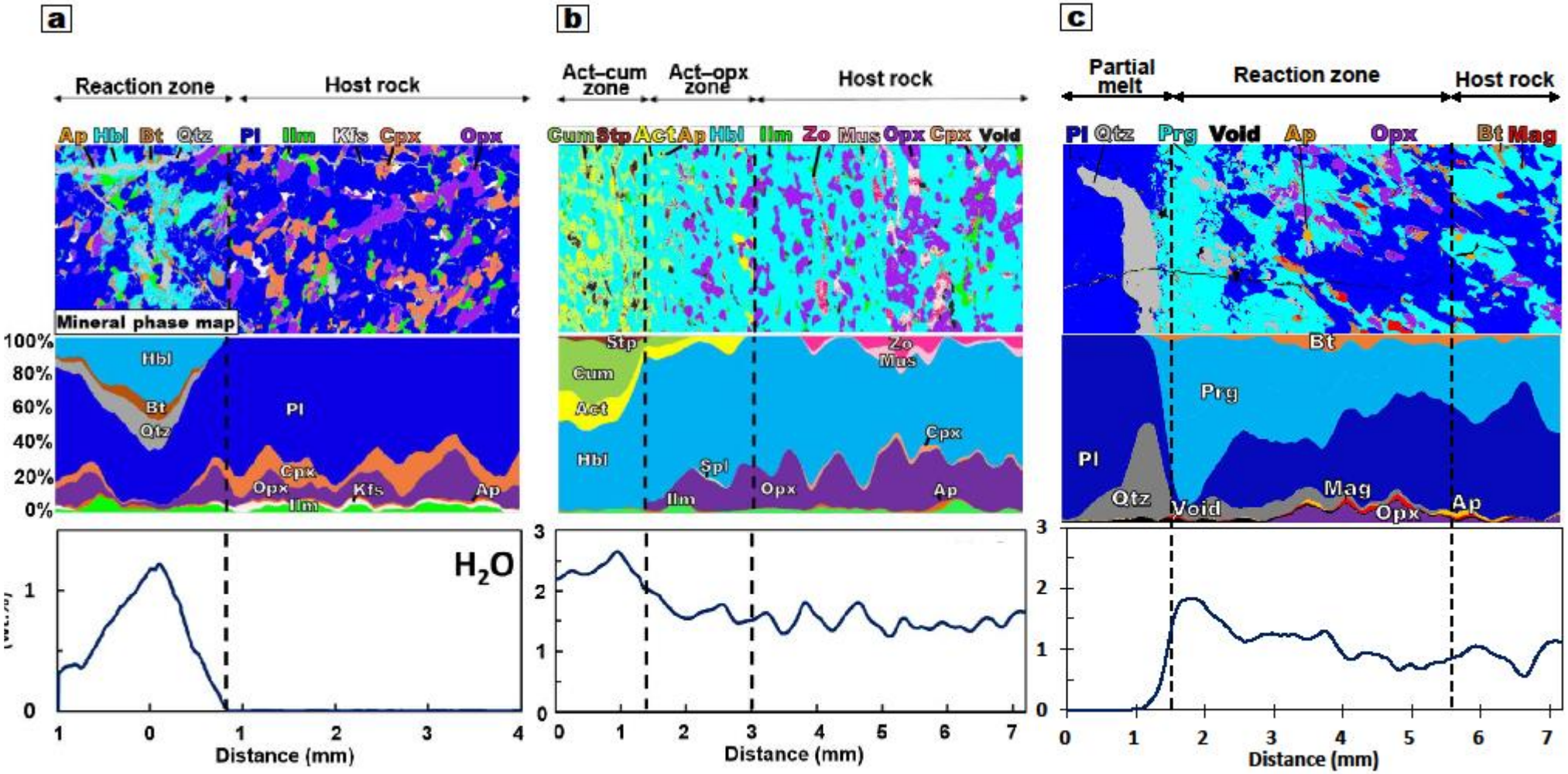

Fig.8 Elemental and mineral phase maps, modal mineralogy profiles, and H_2O content variations in the (a) mafic granulite, (b) opx–hbl schist and (c) opx–hbl gneiss. The mineral phase maps were made with XmapTools (Lanari et al., 2014).

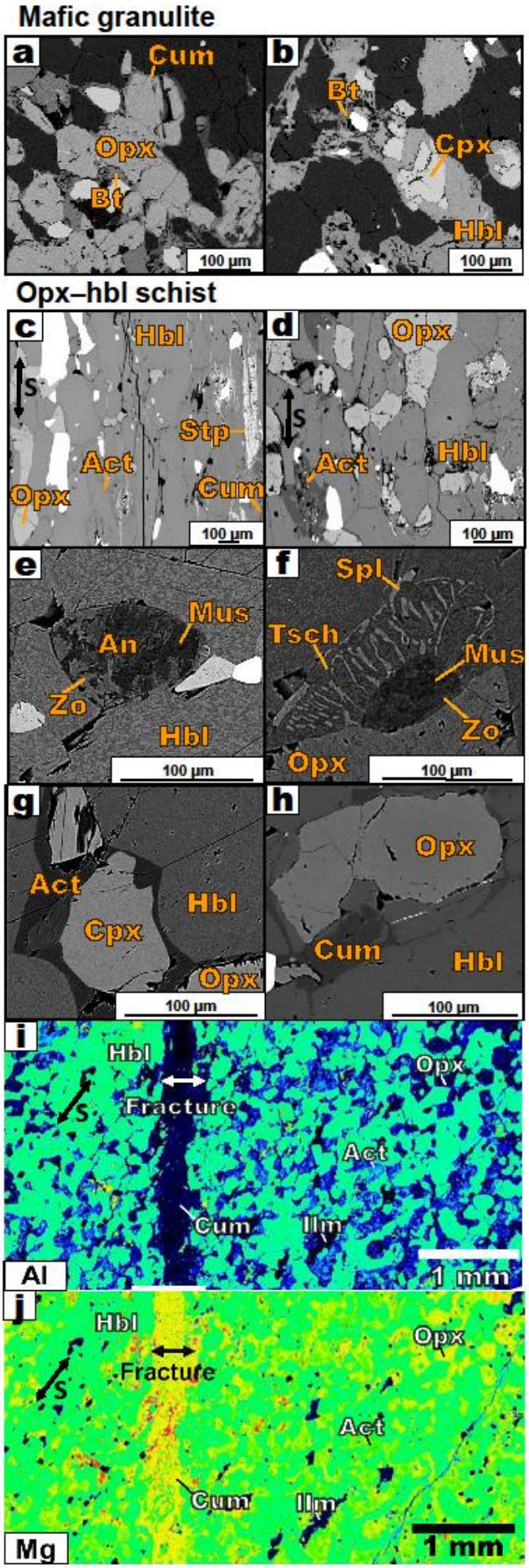
Mafic granulite
a
Cum
Opx
Bt
100 µm
b
Bt
Cpx
Hbl
100 µm
Opx–hbl schist
c
Hbl
S
Stp
Act
Opx
Cum
100 µm
d
Opx
S
Act
Hbl
100 µm
e
Mus
An
Zo
Hbl
100 µm
f
Spl
Tsch
Mus
Zo
Opx
100 µm
g
Act
Hbl
Cpx
Opx
100 µm
h
Opx
Cum
Hbl
100 µm
i
Hbl
S
Fracture
Opx
Act
Cum
Ilm
Al
1 mm
j
Hbl
S
Fracture
Opx
Act
Cum
Ilm
Mg
1 mm

Fig. 9 Replacement and symplectite textures in reaction zones in the mafic granulite (a–b) and opx–hbl schist (c–j). (a–b) Orthopyroxene and clinopyroxene partly replaced by hornblende and biotite in mafic granulite. (c) Boundary between actinolite–cummingtonite zone (right) and actinolite–orthopyroxene zone (left) (d) Boundary between actinolite–orthopyroxene zone (left) and opx–hbl shist host rock (right). (e) Symplectite of zoisite and muscovite after anorthite in the opx–hbl schist host rock. (f) Zoisite–muscovite surrounded by a symplectite of tschermakite–spinel in the actinolite–orthopyroxene zone. (g) Clinopyroxene rims partly replaced by actinolite. (h) Orthopyroxene rims partly replaced by cummingtonite. (i–j) Elemental map of Al and Mg showing a fracture filled with cummingtonite, surrounded by actinolite–cummingtonite reaction zone. Arrows with "s" indicate schistosity.

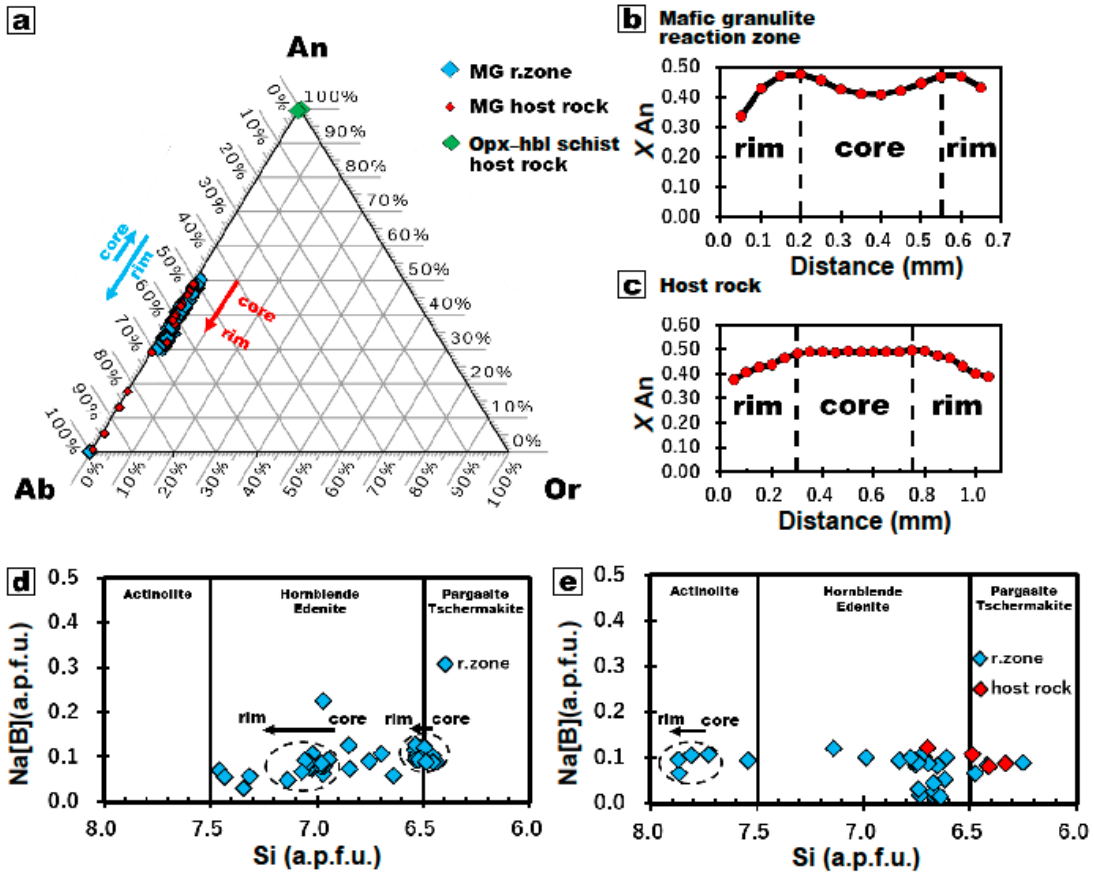

Fig. 10 (a) Albite (Ab)–anorthite (An)–oligoclase (Or) ternary diagram for the mafic granulite and opx–hbl schist. Anorthite content (X_{An} = Ca/[Ca + K + Na]) variations in

single plagioclase grains in the (b) mafic granulite reaction zone and (c) its host rock. Compositional variations of amphibole shown as Na (a.p.f.u) in the B site versus Si (a.p.f.u.) for the reaction zones in the (d) mafic granulite and (e) opx–hbl schist.

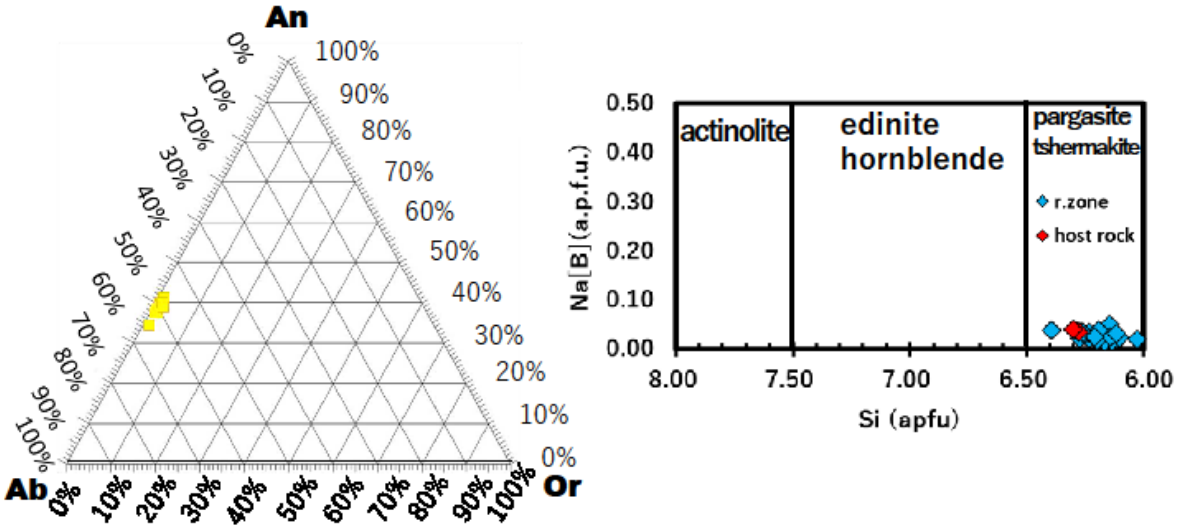

Fig. 11 (a) Albite (Ab)–anorthite (An)–oligoclase (Or) ternary diagram for the opx–hbl gneiss. Compositional variations of amphibole shown as Na (a.p.f.u) in the B site versus Si (a.p.f.u.) for the reaction zones in the opx–hbl gneiss.

2.4.1 Mafic granulite

In the mafic granulite, dark coloured reaction zones crosscut the host rock (Fig. 2). Mafic granulite is holocrystalline with an equigranular texture. Two zones were identified in the mafic granulite samples (Figs. 3a and 4a): (i) reaction zones (1–2 mm thick); and (ii) mafic granulite host rock.

2.4.1.1 Mafic granulite host rock

The host rock consists dominantly of plagioclase (70.1 vol.%), orthopyroxene (12.2 vol.%), and clinopyroxene (11.2 vol.%), with minor amounts of ilmenite (3.2 vol.%), K-

feldspar (2.1 vol.%), and apatite (1.1 vol.%) (Table 2; Fig. 6 a).

Plagioclase and K-feldspar are euhedral to subhedral and 50–500 and 20–50 μm in size, respectively. Clinopyroxene and orthopyroxene are euhedral to subhedral and 100–500 μm and 100 μm to 1 mm in size, respectively. Ilmenite are present as minor minerals and are 100–300 μm in size. Apatite is elongate with lengths of 10–50 μm and widths of 5–30 μm. Alignment of orthopyroxene and clinopyroxene defines the gneissosity within the host rock, which are obliquely cut by the reaction zones (Fig. 6 a)

2.4.1.2 Reaction zone

The reaction zone consists mainly of plagioclase (47.2 vol.%), hornblende (22.4 vol.%), and quartz (9.3 vol.%), with minor amounts of orthopyroxene (8.4 vol.%), biotite (4.2 vol.%), ilmenite (3.6 vol.%), clinopyroxene (2.8 vol.%), apatite (1.2 vol.%), K-feldspar (0.4 vol.%), and chlorite (0.2 vol.%). Amphibole is anhedral and 20–300 μm in size.

Biotite is euhedral–subhedral, acicular or fibrous, and 20–200 μm in size. Quartz is anhedral and 20–300 μm in size. Ilmenite are present as minor minerals and are 100–300 μm in size. Apatite is present as an accessory mineral with lengths of 10–50 μm and widths of 5–30 μm. Clinopyroxene and orthopyroxene are partly or completely replaced by hornblende or cummingtonite, respectively, with biotite present at the pyroxene crystal rims (Fig. 9 a, b). There is no preferred orientations for biotite or amphiboles.

The presence of clinopyroxene, orthopyroxene, plagioclase, and K-feldspar is mostly limited to the host rock. In contrast, the reaction zones are characterised by the occurrence of hydrous minerals such as biotite, cummingtonite, and hornblende. Pyroxene replacement textures (Fig. 9 a, b) suggest that the pyroxenes have decomposed to these hydrous minerals. No significant grain size differences or modal variations were observed for apatite between the different zones.

2.4.1.3 Mineral chemistry of Mafic granulite

Most of the plagioclase grains in the host rock are depleted in Ca ($X_{an} < 0.35$) as compared with the plagioclase in the reaction zone (Table 3; Fig. 10 a). Some plagioclase grains in the host rock exhibit compositional zoning with higher anorthite contents in the core ($X_{an} \approx 0.5$) than the rim ($X_{an} \approx 0.35$), whereas plagioclase grains in

the reaction zone show increasing anorthite content from the core ($X_{an} \approx 0.40$) to the mantle ($X_{an} \approx 0.50$), which then decreases towards the rim ($X_{an} \approx 0.35$), (Fig. 10 b, c). The anorthite-rich plagioclase ($X_{an} \approx 0.45$) in the reaction zone is in contact with the tschermakite rim of zoned hornblende. K-feldspar is also present in the reaction zone and the host rock ($X_{or} = 0.93–0.96$).

The amphiboles show large variations in Si contents, with the type of amphibole varying from hornblende to tschermakite (Fig. 10 d, e). The most common amphibole is hornblende. Si contents show variations from 6.4 to 7.5 atoms per formula unit (a.p.f.u.), and Na contents in the B site vary from 0.01–1.5 a.p.f.u. The amphibole grains are zoned and Si contents in individual grains vary by up to 0.3 a.p.f.u. (Fig. 10 d).

X_{Mg} values of clinopyroxene in the reaction zones ($X_{Mg} = 0.58–0.63$) and host mafic granulite ($X_{Mg} = 0.59–0.64$) are almost identical. Orthopyroxene X_{Mg} values are similar in the host mafic granulite ($X_{Mg} = 0.46–0.48$) and reaction zones ($X_{Mg} = 0.45–0.47$).

Apatite is ubiquitous in the reaction zones and host rocks, and is the main host of Cl and F. Cl contents vary significantly from 0.38 wt.% in the reaction zones to 0.05 wt.% in the host mafic granulite (Fig. 12 a). In contrast, apatite F contents increase from the reaction zone (1.46 wt.%) to the host rock (3.46 wt.%).

The highest Cl contents in apatite are observed in the grains in the reaction zone, and gradually decrease moving into the host rocks. Apatite Cl concentrations are uniform at $x < 2$ mm from the centre of the reaction zones, whereas at $x > 2$ mm the apatite Cl concentrations decrease. No significant compositional zoning was observed for Cl and F concentrations within single apatite grains.

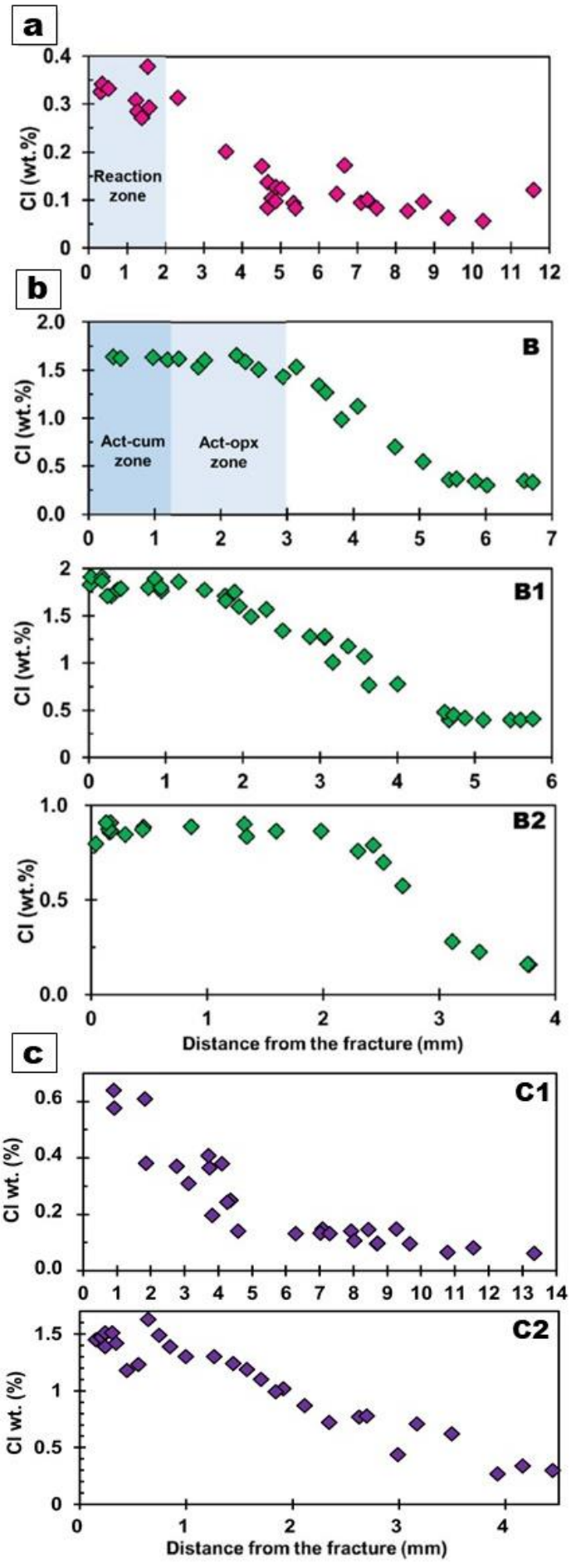
a
Cl (wt.%)
Reaction zone
b
B
Act-cum zone
Act-opx zone
B1
B2
Distance from the fracture (mm)
c
C1
C2
Cl wt. (%)
Distance from the fracture (mm)

Fig. 12 Chlorine profiles in individual apatite grains from the (a) mafic granulite, (b) opx–hbl schist, and in apatite and pargasite grains in (c) opx–hbl gneiss. In (a), the blue coloured area shows the reaction zone. In (b), the blue coloured area shows the stp–act–cum zone and the light blue coloured area shows the act–opx zone. (C1) is the profile measured in apatite grains and (C2) in pargasite grains in the reaction zone in opx–hbl gneiss

2.4.2 Opx–hbl schist

The opx–hbl schist is fine-grained with a schistose structure. Some of the opx–hbl schist samples contain narrow (<0.4 mm) fractures identified by depletion of Na, Ca, and Al, and enrichment of Si and Mg in elemental maps (Fig. 9 i, j). Based on the local mineral assemblages, grain size variations, occurrence of minerals and symplectites, the opx–hbl schist samples can be divided into (Figs. 6 b, c and 9 c, d): (i) actinolite–cummingtonite (act–cum) zones (1.4 mm thick); (ii) actinolite–orthopyroxene (act–opx) zones (1.6 mm thick); and (iii) host rock. Actinolite–cummingtonite zones are surrounded by actinolite–orthopyroxene zones, which in turn gradually zone into the host rock. Rare microfractures radiate from the centre of the fracture in a direction sub-perpendicular to the reaction zone, and cut the reaction zone ± host rock (Fig. 13). Narrow hydration zones (<0.03 mm thick) occur along the microfractures (Fig. 13 d).

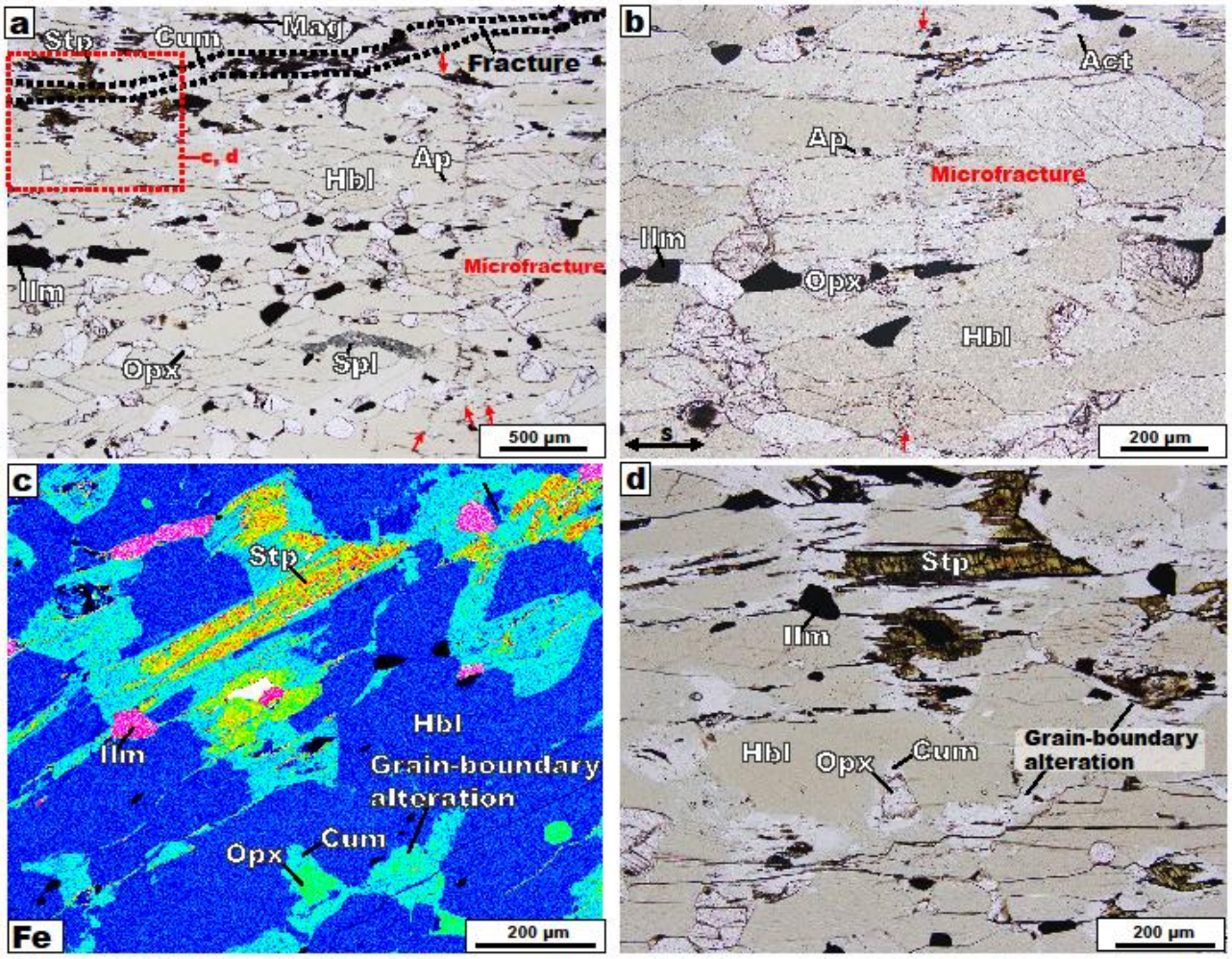

Fig. 13 Microfracture distribution and occurrence in reaction zones in opx–hbl schist. Red arrows indicate microfracture locations. (a) Microfractures emanating from the main fracture and cutting the reaction zones and schistosity. (b) Microfractures located farther from the main fracture with narrow hydration zones. (c) Fe X-ray map of the area located farther from the microfracture showing orthopyroxene to cummingtonite alteration along grain boundaries. (d) Photomicrograph of the X-ray map area showing grain–boundary alteration. The scale bars are 500 and 200 µm in length.

2.4.2 Petrography of opx–hbl schist

2.4.2.1 Host rock

The host rock consists dominantly of hornblende (62.9 vol.%) and orthopyroxene (25.2 vol.%), with minor amounts of zoisite (4.0 vol.%), muscovite (2.5 vol.%), ilmenite (1.9 vol.%), clinopyroxene (1.5 vol.%), apatite (0.9 vol.%), anorthite, and spinel. The modal abundance of amphiboles is the lowest and that of pyroxenes the highest as compared with the other zones (Fig. 8 b).

Hornblende is euhedral–subhedral and 500 μm to 1.5 mm in size. Orthopyroxene is euhedral–subhedral and 100 μm to 1 mm in size. Alignment of hornblende defines the schistosity and lineation. Apatite is elongate with lengths of 20–50 μm and widths of 5–30 μm.

Ilmenite is a minor phase and 100–300 μm in size. Anorthite is replaced by zoisite and muscovite symplectites (Fig. 9 e) that are 50–130 μm in size. Clinopyroxene is partly replaced by actinolite (Fig. 9 g). Only anorthite-rich plagioclase ($X_{an} > 0.98$) is present in the host rock (Fig. 10 a).

2.4.2.2 Actinolite–orthopyroxene zone

The mineral mode of amphibole, including hornblende (71.9 vol.%) and actinolite (5.1 vol.%), increases in the actinolite–orthopyroxene zone as compared with the host rock. The orthopyroxene mode is lower (18.9 vol.%), and minor amounts of ilmenite (2.3 vol.%), apatite (0.5 vol.%), and spinel (0.5 vol.%) were observed in the actinolite–orthopyroxene zone (Fig. 4 b).

Hornblende is euhedral–subhedral and 500 μm to 1.5 mm in size. Actinolite is subhedral–anhedral and 20–100 μm in size. Orthopyroxene is euhedral–subhedral and 50–100 μm in size. Apatite is acicular with lengths of 20–50 μm and widths of 5–30 μm. Ilmenite is 100–400 μm in size. Pseudomorphic textures of orthopyroxene partly replaced by cummingtonite are present (Fig. 9a).

Anorthite, zoisite, and muscovite symplectites further reacted with surrounding hornblende, and are surrounded by tschermakite–spinel symplectites (Fig. 9 f), which are 50–200 μm in size.

2.4.2.3 Actinolite–cummingtonite zone

The actinolite–cummingtonite zone is fine-grained as compared with the other zones (Fig. 6 c). The total amphibole mode is highest in this zone (>88.4 vol.%), and includes hornblende (57.3 vol.%), cummingtonite (19.7 vol.%), and actinolite (11.4 vol.%). Minor amounts of stilpnomelane (3.2 vol.%), orthopyroxene (4.7 vol.%), ilmenite (1.1 vol.%), apatite (0.6 vol.%), and spinel (0.02 vol.%) are present in this zone (Fig. 8 b).

Hornblende is euhedral–subhedral and 500 μm to 1 mm in size. Actinolite is subhedral and 400–800 μm in size. Orthopyroxene is almost entirely decomposed, subhedral, and 50–150 μm in size. Cummingtonite occur along the grain boundaries between hornblende and decomposed orthopyroxene (Fig. 13 c and d). Elongated cummingtonite and/or fibrous stilpnomelane occur in the centre of fractures (Fig. 6 b and c; Fig. 9 i and j), are elongate along the fracture orientation or show epitaxial growth on hornblende grains adjacent to the fracture, and are 50 μm to 1 mm in size. Apatite is 20–40 μm in width and 5–30 μm in length. Ilmenite and magnetite are 50–500 μm in size (Fig. 6 b, c).

The actinolite content decreases with increasing distance from the actinolite–cummingtonite zone to the host rock. In contrast to actinolite, orthopyroxene and clinopyroxene contents increase with distance from the actinolite–cummingtonite zone (Fig. 8 b). In addition, stilpnomelane, magnetite, and brucite–serpentine are only observed in the actinolite–cummingtonite zone.

2.4.2.4 Microfractures

Small-scale microfractures are observed locally in the reaction zones ± host rock (Fig. 13 a, b). They radiate from the main fracture and cut the reaction zones and schistosity (Fig. 13 a). Hornblende grains are partly altered to actinolite along the microfractures (Fig. 13 b). The width of actinolite alteration (<30 μm) is dependent on the distance from the main fracture: microfractures near the main fracture typically have a wider hydration reaction zone (Fig. 13 a) than those in the reaction zones, which show little hydration (Fig. 13 b). The lengths of the microfractures vary from ~1.0 to 3.5 mm.

2.4.2.5 Mineral chemistry of opx-hbl schist

Amphiboles show large variations in Si contents from 6.3 to 6.7 a.p.f.u. in the host rock and 6.3 to 7.9 a.p.f.u. in the reaction zones, with the type of amphibole varying from actinolite to tschermakite (Fig. 10 d, e). The most common amphibole is hornblende. Na contents in the B site are 0.8–1.2 a.p.f.u. in the host rocks and 0.01–1.5 a.p.f.u. in the reaction zones (Fig. 10 e). Si contents in zoned actinolite grains vary by up to 0.2 a.p.f.u. (Fig. 10 e). Cummingtonite is also present in the reaction zones, and has Si contents of 7.3–7.5 a.p.f.u. and X_{Mg} of 0.72–0.73.

X_{Mg} values of orthopyroxene vary from 0.69–0.72. Clinopyroxene has higher X_{Mg} (0.79–0.86).

Apatite is main host of Cl and F, and ubiquitous in the reaction zones and host rocks. Cl contents increase from 0.1 wt.% in the host rock to 1.66 wt.% in the actinolite–cummingtonite zone (Fig. 12 b). Apatite F contents decrease from the host rock to the actinolite–cummingtonite zone (2.30–0.25 wt.%). All the analysed profiles have almost constant apatite Cl concentrations at x < 2–3 mm from centre of the actinolite–cummingtonite zone, which decrease abruptly at x = 2–6 mm (Fig. 12 a, b). Apatite Cl contents are almost constant (~1 wt.%) in areas close to the microfractures, regardless of the distance from the main fracture, and are similar to those in the actinolite–cummingtonite zone. No significant compositional zoning was observed for Cl and F concentrations within single apatite grains (Fig. 14).

2.4.3 Opx-hbl gneiss

The opx–hbl gneiss is fine-grained with a schistose structure. Some of the opx–hbl schist samples contain partial melt with small opx, pgs, bt inclusions (Fig. 6 d).

Based on the local mineral assemblages, grain size variations, occurrence of minerals and replacement textures, reaction progress and trace elements profiles the opx–hbl gneiss samples can be divided into (Figs. 6 d and 8 c): (i) partial melt (1.5 mm thick); (ii) reaction zone zones (4 mm thick); and (iii) host rock. Partial melt is surrounded by reaction zone, which in turn gradually into the host rock.

2.4.3.1 Host rock

The opx–hbl gneiss host rock consist mainly of plagioclase (52.4 vol.%), clinopyroxene (15.0 vol.%), orthopyroxene (6.6 vol.%), and pargasite (19.9 vol.%) with minor amounts of biotite (1.0 vol.%), quartz (2.5 vol.%), apatite (0.4 vol.%), ilmenite

(0.5 vol.%), magnetite (1.8 vol.%). The modal abundance of amphiboles is the lowest and that of pyroxenes the highest as compared with the other zones (Fig. 8 c).

Plagioclase is subhedral, 100 μm to 500 μm in size, orthopyroxene and clinopyroxene are euhedral to subhedral and 100–2 mm in size. Alignment of orthopyroxene and clinopyroxene defines the gneissosity within the host rock, which are obliquely cut by the reaction zones (Fig. 6 c). Pargasite is subhedral to anhedral, 100–500 μm in size.

Biotite is minor phase, 50–100 μm in size. Quartz is euhedral, mostly surrounds orthopyroxene and clinopyroxene, 20–100 μm in size. Apatite is subhedral, 20–100 μm in size. Ilmenite and magnetite are 50–100 μm in size.

2.4.3.2 Partial melt

The partial melt consists dominantly of plagioclase (67.3 vol.%) and quartz (20.5 vol.%), with minor amount of orthopyroxene (62.9 vol.%), pargasite (9.1 vol.%), biotite (1.0 vol.%), apatite (0.1 vol.%).

Plagioclase within the partial melt is subhedral to anhedral, 200 μm to 3 mm in size, quartz is subhedral to anhedral and 100 μm to 3 mm in size. Orthopyroxene is anhedral, 100–500 μm in size. Accessory minerals are mostly decomposed (fully reacted) in the partial melt. Pargasite is subhedral to anhedral, 100–500 μm in size. Biotite is anhedral, 50–400 μm in size. Apatite is present as minor mineral and are 20–100 μm in size.

2.4.3.3 Reaction zone

The opx–hbl gneiss reaction zone consists mainly of pargasite (62.9 vol.%), plagioclase (24.0 vol.%), with minor amount of orthopyroxene (1.0 vol.%), biotite (2.8 vol.%), quartz (7.4), apatite (0.1 vol.%), ilmenite (0.2 vol.%), magnetite (0.1 vol.%). The modal abundance of amphiboles is the highest as compared with the other zones (Fig. 8 c)

Pargasite is subhedral, 50 μm to 500 μm in size Plagioclase is subhedral to anhedral, 30 μm to 500 μm in size, orthopyroxene is subhedral and 50–500 μm in size. Biotite is present as minor phase, 10–100 μm in size. Quartz is subhedral, 50–400 μm in size. Apatite is subhedral and 20–50 μm in size. Ilmenite and magnetite are anhedral,

20–80 μm in size.

2.4.3.4 Mineral chemistry of opx-hbl gneiss

Amphiboles show variations in Si contents from 6.2 to 6.3 a.p.f.u. in the host rock and 6.1 to 6.4 a.p.f.u. in the reaction zones, with the type of amphibole varying from cummingtonite to pargasite (Fig. 11). The most common amphibole is pargasite. This type of amphibole can incorporate significant amount of chlorine. Na contents in the B site are almost same, 0.04 a.p.f.u. in the host rocks and 0.02–0.05 a.p.f.u. in the reaction zones (Fig. 11). Al content in pargasite varies 2.06–2.43 in reaction zone, and 2.09–2.16 in host rock. Most grains in reaction zone have Mg–rich cores, in the host rock no compositional zonings have observed. Pargasite is one of the main host of Cl, and ubiquitous in the reaction zones and host rocks. Cl contents increase from 0.27 wt.% in the host rock to 1.63 wt.% in the reaction zone (Fig. 12 c). Biotite X_{Mg} values vary from 0.49–0.67. Cl contents vary 0.27 wt.% in the host rock to 1.08 wt.% in the reaction zone. Highest content corresponds to the reaction zone.

X_{Mg} values of orthopyroxene vary from 0.53–0.55. Clinopyroxene has higher X_{Mg} (0.66–0.67). Some clinopyroxene grains in the host rock have Mg–rich rim compare to the core.

Apatite is ubiquitous in the reaction zones and host rocks and contains Cl and F. Cl contents increase from 0.1 wt.% in the host rock to 0.64 wt.% in the reaction zone (Fig. 12 c). Apatite F contents decrease from the host rock to the reaction zone (4.29–2.11 wt.%). No significant compositional zoning was observed for Cl and F concentrations within single apatite grains.

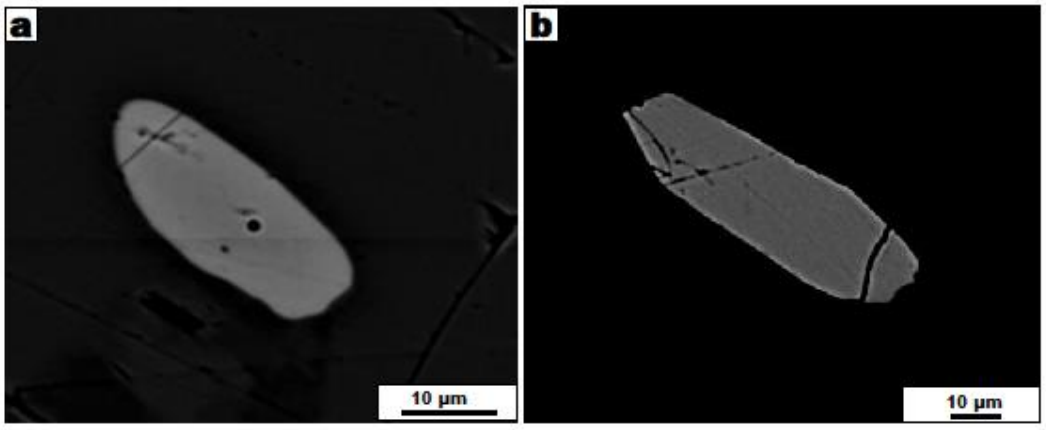

Fig. 14 Backscattered electron images showing absence of zoning in the apatite grains in the (a) reaction zone and (b) host rock.

2.5 P–T conditions of fluid infiltration

The *P–T* conditions of the reaction zones, host rocks and partial melt were determined using geothermobarometry. All samples represent unit C of SW terrane. The host mafic granulite yielded a temperature of 850 ± 50°C from two-pyroxene thermometry (Lindsley, 1983). The reaction zones in the mafic granulite yielded *P–T* conditions of 0.55 ± 0.05 GPa and 620 ± 60°C from Al-in-hornblende geobarometry (Anderson and Smith, 1995) and hornblende–plagioclase geothermometry (Holland and Blundy, 1994).

For the opx–hbl schist, the temperature of the actinolite–cummingtonite zone was estimated to be ~450°C from the magnetite–ilmenite thermometer (Powell and Powell, 1977; Lepage, 2003).

For the opx–hbl gneiss, the temperature of host rock was estimated to be 760-870 °C from two-pyroxene thermometry (Lindsley, 1983). The reaction zones yielded *P–T* conditions of 0.54 – 0.62 GPa and 720-740 °C from Al-in-hornblende geobarometry (Anderson and Smith, 1995) and hornblende–plagioclase geothermometry (Holland and Blundy, 1994). Based on these results, the *P–T* conditions of fluid infiltration are constrained as 0.54 – 0.62 GPa and 720-760 °C in the opx–hbl gneiss, 0.55 ± 0.05 GPa and 620 ± 60°C in the mafic granulite, and ~450°C in the opx–hbl schist (Fig. 15).

The SW terrane metapelite sample of unit D from Mefjell recorded a nearly isothermal P–T path from 0.41 GPa and 500°C to a peak *P–T* condition of 0.56 GPa and 700 °C, followed by retrogression (0.42 GPa, 620°C) at ca. 700–540 Ma (Tsubokawa et al., 2017). By contrast, the unit-C part of SW terrane yielded a counter-clockwise *P–T* path for granulite-facies rocks (e.g., Adachi et al., 2013; Baba et al., 2012). The pre-collision stage had *P–T* conditions of 0.6–0.7 GPa and 800–900°C (e.g., Adachi et al., 2013; Baba et al., 2012), which was followed by peak metamorphism at 0.8–0.9 GPa and 800–900°C (e.g., Adachi et al., 2013; Baba et al., 2012) at ca. 630–620 Ma. The *P–T* conditions of the host mafic granulite (>0.5 GPa; 800–900 °C) and host opx–hbl gneiss (>0.5 GPa; 760–870 °C) correspond to pre-collision stage or the peak metamorphic conditions of unit C. The hydrous reaction zones in the opx–hbl gneiss (0.54 – 0.62 GPa and 720-740 °C) was formed during compression followed by peak metamorphic stage. Reaction zone in the mafic granulite formed due to fluid infiltration

during decompression and cooling, which was followed by further cooling to ~400°C at ca. 590–530 Ma (Osanai et al., 2013).Therefore, the *P–T* conditions of reaction zone formation in the opx–hbl schist (~450°C) correspond to the last stage of metamorphism of unit C.

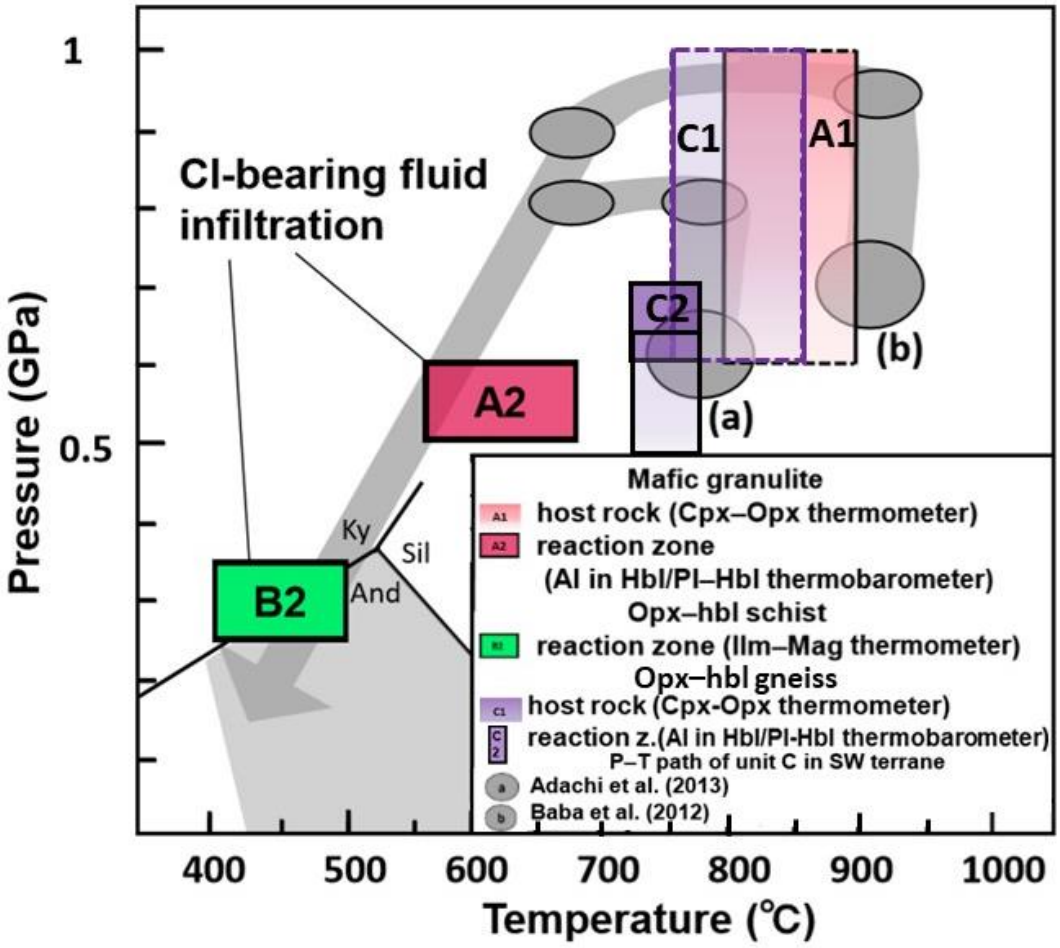

Fig. 15 *P–T* conditions of unit C in the southwestern (SW) terrane. Estimated *P–T* conditions are shown in pink for the mafic granulite, green for the opx–hbl schist, and purple for the opx–hbl gneiss. Metamorphic paths are shown by the grey fields and arrow, and extend from the pre-subduction to final metamorphic stage (taken from Adachi et al. (2013) and Baba et al. (2012)). Reaction z = reaction zones.

2.6 Mass transfer during fluid infiltration

Clear differences in chemistry between the host rocks and reaction zones are observed for several elements, such as Al, K, and H_2O (Fig. 16 a, b, Fig 17). For example, in the mafic granulite, H_2O, K_2O, and to a lesser extent FeO are enriched in the reaction zones as compared with the host rock, whereas Al_2O_3 and Na_2O are depleted in the reaction zones. The Al and Na variations can be explained by removal of Al_2O_3 and Na_2O from the reaction zones, whereas H_2O and K_2O have been added to the reaction zone by fluid infiltration (Fig. 16 a).

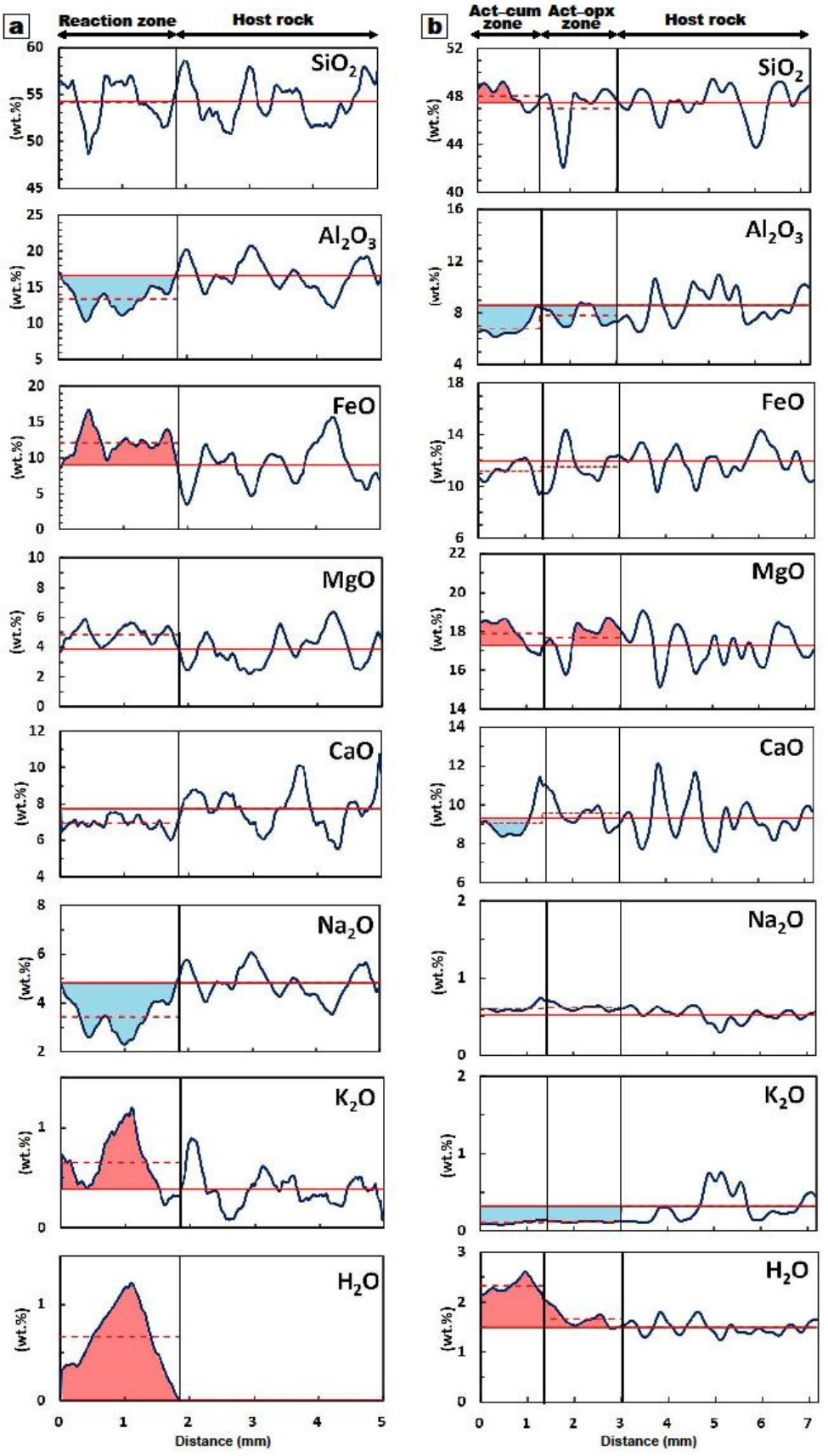
a
Reaction zone
Host rock
b
Act–cum zone
Act–opx zone
Host rock
SiO2
Al2O3
FeO
MgO
CaO
Na2O
K2O
H2O
(wt.%)
Distance (mm)

Fig. 16 Elemental profiles from the centre of the reaction zones into the (a) mafic granulite and (b) opx–hbl schist. The red solid lines are the average element contents calculated for the host rocks and the dotted lines are the averages for each reaction zone. Pink and blue areas indicate element addition and removal during hydration reactions, respectively.

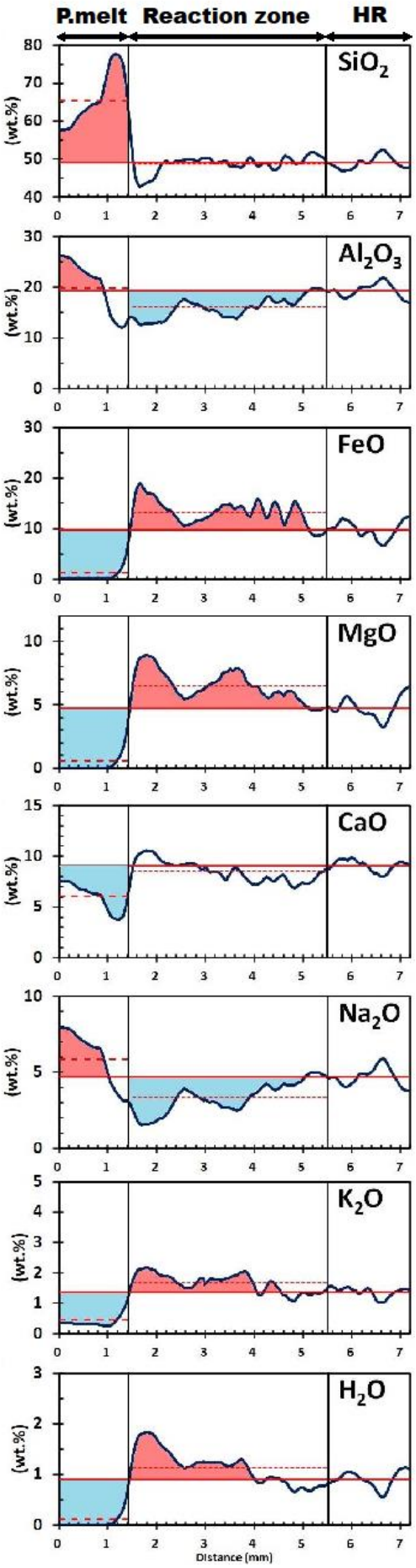
P.melt
Reaction zone
HR
SiO2
Al2O3
FeO
MgO
CaO
Na2O
K2O
H2O
(wt.%)
Distance (mm)

Fig. 17 Elemental profiles from the partial melt into the opx–hbl gneiss. The red solid lines are the average element contents calculated for the host rocks and the dotted lines are the averages for each reaction zone. Pink and blue areas indicate element addition and removal during hydration reactions, respectively.

In the opx–hbl schist, SiO_2, MgO, and H_2O are slightly enriched in the actinolite–cummingtonite zone, whereas K_2O and Al_2O_3 are depleted in the actinolite–cummingtonite and actinolite–orthopyroxene zones. CaO is slightly depleted in the actinolite–cummingtonite zone (Fig. 16 b). These results reveal that H_2O was added from outside the system into the actinolite–cummingtonite and actinolite–orthopyroxene zones. K_2O, CaO, and Al_2O_3 were removed from the actinolite–cummingtonite and actinolite–orthopyroxene zones (Fig. 16 b).

In the opx–hbl gneiss, in the partial melt SiO_2, Al_2O_3, and Na_2O are enriched, whereas FeO, MgO, CaO, K_2O, and H_2O are depleted. FeO, MgO, H_2O, and to a lesser extent K_2O are enriched in the reaction zones as compared with the host rock, whereas Al_2O_3 and Na_2O are depleted in the reaction zones (Fig. 17). The Al and Na variations can be explained by removal of Al_2O_3 and Na_2O from the reaction zones, whereas H_2O and K_2O have been added to the reaction zone by fluid infiltration (Fig. 17).

Mass transfer in the mafic granulite, opx–hbl schist and opx–hbl gneiss was different during fluid infiltration: Al_2O_3 and Na_2O were removed and K_2O was added in the mafic granulite and opx–hbl gneiss, and K_2O and CaO were removed in the opx–hbl schist (Fig.16a, b; Fig. 17).

2.7 Reactions during fluid infiltration

2.7.1 Mafic granulite

Decomposition of pyroxenes in the reaction zones is clearly evident from changing modal ratios of opx + cpx/opx + cpx + hornblende (Fig. 18 a). From microtextural observations (Fig. 9 a, b) and modal mineralogy variations (Fig. 8 a), the following decomposition reactions for clinopyroxene and orthopyroxene are inferred:

(1) Breakdown of orthopyroxene and plagioclase to cummingtonite, biotite, and quartz (Fig. 9 a), which was associated with K^+ input from fluid (Fig. 16 a) and/or breakdown of K-fs:

$$Opx + Pl + H_2O + K^+ \pm \text{K-fs} \rightarrow Cum + Bt + Qtz + Ca^{2+} + Na^+ \quad \text{(Rx. 1)}$$

(2) Breakdown of clinopyroxene to hornblende and biotite, which was also associated with K^+ input from the fluid and/or breakdown of K-feldspar (Fig. 16 a):

$$Cpx + K^+ \pm \text{K-fs} + H_2O \rightarrow Hbl + Bt \pm H^+ \quad \text{(Rx.2)}$$

(3) As there is no Ca depletion at the reaction zone compared to the host rock (Fig. 16 a), Ca^{2+} produced by Rx. 1 was consumed for forming Ca-rich plagioclase (X_{an} > 0.35) (Fig. 16 a). A final reaction:

$$Opx + Cpx + \text{Pl (Ca-poor)} + \text{K-fs} + K^+ + H_2O$$
$$\rightarrow Hbl + Cum + Bt + Qtz + \text{Pl (Ca-rich)} + Na^+ + H^+ \quad \text{(Rx. 3)}$$

The extent of these reactions (Fig. 18 a), the mass transport of K_2O, Na_2O and H_2O (Fig. 16 a) and Cl profile in apatite (Fig. 12 a) all coincide with the distance of x = 0–1mm. This suggests that the fluid infiltration, mass transport of K, Na, Cl and H_2O, and replacement reactions of pyroxene and apatite are coupled processes.

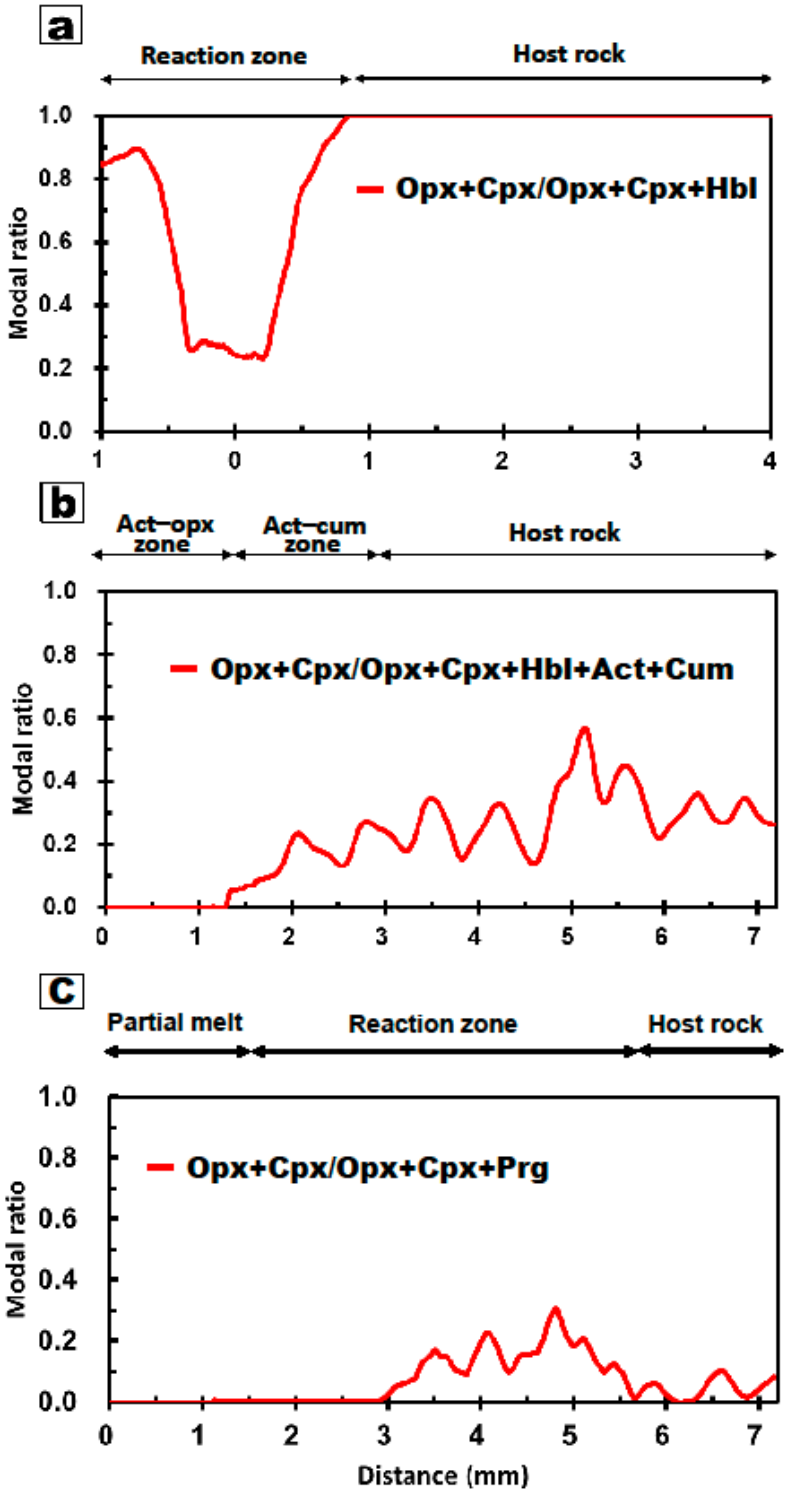

Fig. 18 Pyroxene and amphibole modal variations in the (a) mafic granulite, (b) opx–hbl schist and (c) opx–hbl gneiss showing the hydration reaction progress.

2.7.2 Opx–hbl schist

In the opx–hbl schist, anorthite–muscovite–zoisite replacement textures are common in the host rock (Fig. 9 e) and may record the primary hydration stage:

$An + K^+ + H_2O \rightarrow Zo + Mus + H^+$ (Rx. 4)

From the host rock to the actinolite–cummingtonite zone, the modal content of pyroxenes decreases and those of hornblende, actinolite and cummingtonite increase (Fig. 18 b). In addition, actinolite occurs between clinopyroxene and hornblende and cummingtonite forms rims around orthopyroxene (Fig. 9 g, h). These modal changes and textures suggest later infiltration of H_2O from the fracture caused breakdown of pyroxenes via the two following reactions:

$Cpx + H_2O \rightarrow Act$ (Rx. 5)

$Opx + H_2O \rightarrow Cum$ (Rx. 6)

The formation of spinel–tschermakite symplectites around anorthite–zoisite–muscovite (Fig. 5e, f) was associated with removal of K (Fig. 16 b). Formation of symplectites in the actinolite–orthopyroxene zone occurred as follows:

$Zo + Mus + Hbl + H^+ \rightarrow Spl + Tsch + K^+$ (Rx. 7)

The Rx. 5 reaction occur at $x \sim 3$ mm, and Rx. 6–7 reactions occur from $x = 3$ mm and complete at $x = 1.3$ mm (Fig. 18 b). The transport distance of Al, Mg K, H_2O and Cl (~3 mm) and Ca (~1.3 mm) coincide with these reactions (Fig. 16 b and 18 b). These observations show that hydration reactions, apatite replacement reactions, mass transfer, and fluid infiltration were coupled processes.

2.7.3 Opx–hbl gneiss

In the opx–hbl gneiss, decomposition of pyroxenes in the reaction zones is common (Fig. 9 e). Replacement textures observed in the reaction zone (Fig. 9 a, b) and modal ratios variations opx + cpx/opx + cpx + pargasite (Fig. 18 c) are showing the evidences for the hydration process. From these observations, fluid infiltration derived from the nearby melt and/or from the fracture caused breakdown of pyroxenes and amphibole formation as result of the hydration reaction.

From the host rock to reaction zone, the modal content of pyroxenes decreases and the modal content of pargasite is increase (Fig. 8 c). In addition, some cummingtonite was observed in the reaction zone, and pargasite often occurs around clinopyroxene grains, forming rims around it (Fig. 9 g, h). These modal changes and textures suggest infiltration of H_2O caused breakdown of pyroxenes via the two following reactions:

$$Cpx + H_2O \rightarrow Prg \quad \text{(Rx. 8)}$$

$$Opx + H_2O \rightarrow Cum \quad \text{(Rx. 9)}$$

2.8 Conclusion

In this chapter, I describe hydration processes in the partly hydrated mafic granulite, opx–hbl schist, and opx–hbl gneiss from SRM, East Antarctica. Based on petrological and microtextural observations samples were divided into the host rock, reaction zones, ± partial melt for the opx–hbl gneiss. Existence of Cl-bearing aqueous fluids previously described in the study area.

I estimated P-T conditions for each sample using geothermobarometry (two-pyroxene thermometry, Al-in-hornblende geobarometry, hornblende–plagioclase geothermometry). Fluid infiltration conditions are constrained as 0.54 – 0.62 GPa and 720-760 °C in the opx–hbl gneiss, 0.55 ± 0.05 GPa and 620 ± 60°C in the mafic granulite, and ~450°C in the opx–hbl schist.

Next, elemental distribution and mineral modes variations was analised. Each sample shows tendency to increase hydrous minerals modes moving from the host rock to the reaction zone, while pyroxenes and plagioclase modes are highest in the host rock. Clear differences in elemental distribution for several elements, such as Al, K, and H_2O between the host rocks and reaction zones are observed. Elemental transfer with fluid infiltration in the mafic granulite, opx–hbl schist and opx–hbl gneiss was different: Al_2O_3 and Na_2O were removed and K_2O was added in the mafic granulite and opx–hbl gneiss, and K_2O and CaO were removed in the opx–hbl schist. Cl concentration in apatite and pargasite individual grains was measured and distribution profiles for the reaction zones were constrained. Significant difference between host rocks and reaction zones was observed. Cl concentration gradually decrease from the center of reaction zones to the host rock.

Reaction texters observed in the hydrous reaction zones, modal variation between pyroxene and amphibole and elemental transfer provide information about hydration reactions. Pyroxenes decomposition by Cl-bearing fluids infiltration reaction is common for the all samples. Amphiboles ± micas are pyroxenes hydration products.

Chapter 3
Timescales of fluid infiltration

3. Timescales of fluid infiltration

3.1 Introduction

The timescales of fluid infiltration are essential to understanding the physical properties of fast and transient geological processes. The timescales of fluid-rock interactions remain largely unknown, fluid–rock interactions probably occur on timescales ranging from millions of years for metamorphic devolatilization reactions (e.g., Ague and Baxter, 2007; Pollington and Baxter, 2010), to tens to hundreds of years for single vein (Beinlich et al., 2020). (John et al., 2012; Taetz et al., 2018; Saishu et al., 2017) and 1–5 yr (Ujiie et al., 2018).

Further, distinguishing single short fluids infiltration from multiple fluid infiltrations remains challenging. Thus, to constrain duration of single fluid–rock interaction, reliable tool clarify times of fluid infiltration and mass transport mechanism should be applied.

In this chapter, to quantify single fluid–rock interaction duration, I applied a reactive transport model based on the diffusion–advection equation with local equilibrium (e.g., Baumgartner and Rumble, 1988; Bickle and McKenzie, 1987; John et al., 2012; Philpotts and Ague, 2009) to the observed trace elements profiles in the reaction zones. Dominant mass transport mechanism was decided, and duration of fluid infiltration was calculated. Results suggest rapid infiltration of Cl-bearing fluids (~hours).

Clear mineralogical and chemical changes are observed in the fluid–rock reaction zones, which were subjected to reactive transport modelling to constrain the duration of fluid infiltration, dominant mass transport mechanism, fluid pressure gradient, and permeability at crustal P–T conditions.

3.2 Reactive transport modelling of Cl in apatite

A reactive transport model based on the diffusion–advection equation with local equilibrium (e.g., Baumgartner and Rumble, 1988; Bickle and McKenzie, 1987; John et al., 2012; Philpotts and Ague, 2009) was applied to the observed tracers profiles such as Cl in individual apatite grains in the Mefjell samples. In addition, Sr, La, Ce, Nd in the opx–hbl schist samples were analysed. To analyse opx–hbl gneiss samples Cl profiles measured in apatite and pargasite grains were used (Fig. 12). Apatite was chosen for the Mefjell samples modelling because it is main host of Cl. Since the concentration of Cl in amphibole and biotite is minor (Table 3), I assume that Cl profiles are mainly controlled by the partition between fluid and apatite, and not by other minerals. As the mode of apatite along reaction zones is relatively constant (Fig. 8), I assume constant fluid/rock partition coefficients along the profile. Lack of chemical zoning in apatite for Cl and F is consistent that local chemical equilibrium had been achieved during partitioning of these elements between fluid and apatite. However, in case of opx–hbl gneiss Cl is incorporated mostly into pargasite and apatite (Table 3). Since partitioning between fluid and minerals is not proportional among apatite and pargasite, I applied cumulative partitioning coefficient. I calculated Cl cumulative partitioning coefficient considering changes in the modes and describe the procedure further.

The following equation accounts for chemical reactions with the assumption of local equilibrium, and describes the element concentration in minerals as a function of distance and time (e.g., Philpotts and Ague, 2009):

$$\frac{\partial C_s}{\partial t} \approx -K_v V_x \varphi \frac{\partial C_s}{\partial x} + K_v D_e \frac{\partial^2 C_s}{\partial x^2} \qquad (Eq.\,1)$$

where C_s is the concentration of chemical species s, t (s) is time, K_v ([mol/cm^3 in fluid] / [mol/cm^3 in rock]) is the equilibrium fluid/solid partition coefficient by volume, V_x (m/s) is the average fluid velocity of infiltration, φ is the porosity under crustal conditions (2×10^{-4} to 2×10^{-5} at 300–500 MPa; Saito et al., 2016), x (m) is the distance from the fracture, D_e (m^2/s) is the effective diffusion coefficient defined as $D_e = \tau\varphi D^i_0$, τ is the tortuosity factor, and D^i_0 is the aqueous tracer diffusion coefficient from Oelkers and Helgeson (1988). τ was assumed to be 0.3–0.7, which is the typical range for metamorphic rocks (Ague and Rudnick, 2003; Bear, 1988). Given the length and width scale of the flow path considered in this study (mm-scale) is within one order of

magnitude of the grain scale (~100 μm), and is not large enough for significant mechanical dispersion (e.g., Bijeljic et al., 2004; Neuman, 1995), I assumed that mechanical dispersion was minor in the observed profiles.

As the concentration of trace elements in apatite or pargasite is not variable at the fracture ($x = 0$) I assume that concentration of fluid in the fracture was constant during the fluid infiltration. Assuming the constant boundary condition, the analytical solution of the differential equation in the case of low porosity is (Ogata and Banks, 1961):

$$c_s{}^{x,t} = c_s{}^0 + (c_s{}^B - c_s{}^0)\frac{1}{2}\left(erfc\left[\frac{x - K_v V_x \varphi t}{2\sqrt{K_v D_e t}}\right]\right.$$

$$\left. + exp\left[\frac{K_v V_x \varphi x}{K_v D_e}\right] erfc\left[\frac{x + K_v V_x \varphi t}{2\sqrt{K_v D_e t}}\right]\right) \qquad (Eq.\,2)$$

where $c_s{}^B$ is the boundary fluid concentration at $x = 0$, $c_s{}^o$ is the initial fluid concentration at $x > 0$ and $t = 0$, $c_s{}^{x,t}$ is the concentration of s at position x and time t, and *erfc* is the complimentary error function erfc(y) = 1 – erf(y). Using the above equation, parameter fitting was conducted with four unknown parameters: $C_s{}^o$ and $C_s{}^B$ to specify boundary conditions, and a and d to specify the mass transport distance for advection and diffusion, respectively, where $a = K_v V_x \varphi t$ and $d = \sqrt{K_v D_e t}$. Geometrically, a represents the distance from the boundary to the centre of the slope of the Cl profile, and d represents the "width" of the slope in which trace elements profile gradually decreases. $C_s{}^o$ and $C_s{}^B$ correspond to the heights of the profile at both ends. The standard deviation of the fitting parameters was estimated by the trust region method (e.g., Moré and Sorensen, 1983).

The self-diffusion coefficients in aqueous fluids (D_i^0) were taken from the calibrated theoretical model of Oelkers and Helgeson (1988) (up to 1000°C and 0.5 GPa) for the calculated *P*–*T* conditions. For the mafic granulite and opx–hbl schist, I used Cl self-diffusion coefficients of 40.0 ± 4.9 × 10^{-9} m^2/s (620 ± 60°C and 0.50 ± 0.05 GPa) and 33.3 ± 5.5 × 10^{-9} m^2/s (450 ± 50°C and 0.30 ± 0.05 GPa), respectively. For the Sr self-diffusion coefficients in the opx–hbl schist, I applied 18.4 ± 2.4 × 10^{-9} m^2/s (450 ± 50°C and 0.30 ± 0.05 GPa). For the opx–hbl gneiss, I used Cl self-diffusion coefficients of 46.1 × 10^{-9} m^2/s (730 ± 10°C and 0.58 ± 0.04 GPa).

The apatite/fluid partition coefficient for Cl (K_d = 2.3) was taken from Kusebauch et al. (2015), which was determined at crustal conditions (400–700°C and 0.2 GPa) in an experimental study. As *P*–*T* dependencies of the partition coefficient were not resolvable from the experimental data, I assumed a constant value of K_d for both the mafic granulite and opx–hbl schist reaction zones. The uncertainty of K_d was estimated as being within one order of magnitude, based on its variation in the apatite–fluid–melt system in the pressure range of 50–200 MPa (Doherty et al., 2014; Webster et al., 2017, 2009). The fluid/rock partition coefficients (K_v) were calculated from K_d values as $K_v = \frac{\rho_f}{\rho_s K_d M_{ap}}$, where ρ_f is the fluid density, ρ_s is the rock density, and M_{ap} is the apatite mode (1.1 vol.% for the mafic granulite and 0.8 vol.% for the opx–hbl schist). K_v values of 11.0 (3.5–34.9) and 15.3 (4.8–48.2) were calculated for the mafic granulite and opx–hbl schist, respectively (Table 6).

In case of opx–hbl gneiss, cumulative Cl partition coefficient was calculated as $K_v = \frac{\rho_f}{\rho_{ap} {K_d}^{ap/f} M_{ap} + \rho_{prg} {K_d}^{prg/f} M_{prg}}$, where ρ_f is the fluid density, ρ_{ap} and ρ_{ap} are apatite and pargasite density, and M_{ap} is the apatite mode and M_{prg} is the pargasite mode (Fig. 19). ${K_d}^{ap/f}$ is apatite/fluid apatite/fluid partition coefficient for Cl (K_d = 2.3) from Kusebauch et al. (2015), ${K_d}^{prg/f}$ is pargasite/fluid partition coefficient for Cl (K_d = 0.045) calculated from Chan et al., 2016 (Fig. 19).

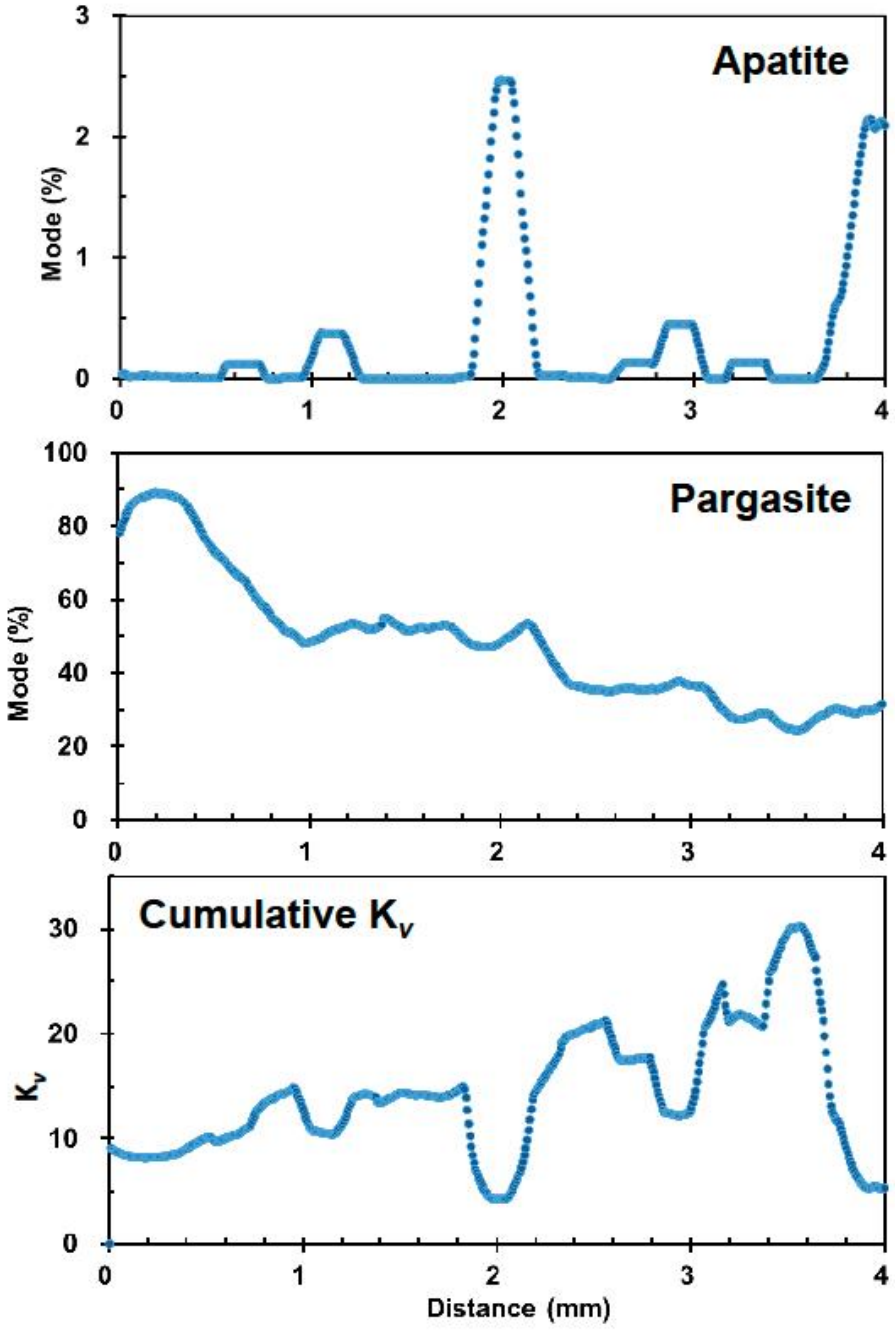

Fig. 19 Apatite and pargasite modes variation with distance in the opx–hbl gneiss reaction zone, and cumulative partitioning coefficient profile.

K_v average value of 14.2 (4.5–44.9) were calculated and used for further calculations, respectively (Table 5).

The Péclet number (*Pe*) was calculated from *a* and *d* as follows (e.g., Lasaga, 1998; Philpotts and Ague, 2009):

$$P_e = \frac{V_x \varphi L}{D_e} = \frac{aL}{d^2} \qquad (Eq. 3)$$

where *L* (m) is the characteristic length of the reaction zone. Based on the obtained *a* and *d* values, the timescale of fluid infiltration (*t*) and average fluid velocity (V_x) were estimated from published K_v and D_e values (Table 5).

For the mafic granulite, the initial and boundary conditions in apatite were fitted as C_s^B = 0.32 ± 0.02 wt.% and C_s^o = 0.10 ± 0.02 wt.% for Cl, respectively, for a profile length (*L*) of 12 mm. The parameters *a* (mm) and *d* (mm), which represent length-scale of advection, diffusion, and mechanical dispersion, yielded values of 3.51 ± 0.33 mm and 0.63 ± 0.21 mm. *Pe* was calculated to be 107 ± 73. Although the Cl concentration data are scattered, the model may explain the general trend of the data (Fig. 20).

For the opx–hbl schist profile, the initial and boundary conditions were defined as C_s^B = 0.2–1.6 wt.% and C_s^o = 0.03–0.30 wt.%, respectively, for a profile length of 4–6 mm. This yielded *a* = 2.75–4.04 mm and *d* = 0.27–0.91 mm. *Pe* varies from 22 to 149 for the three analysed samples.

For the opx–hbl gneiss profile, the initial and boundary conditions were defined as C_s^B = 1.47 ± 0.05 wt.% and C_s^o = 0.27 ± 0.14 wt.%, respectively, for a profile length of 4 mm. This yielded *a* = 1.93 ± 0.23 mm and *d* = 0.93 ± 0.31 mm. *Pe* was calculated to be 9 ± 6.

The Cl concentration profiles are well explained by the model, suggesting advective transport was dominant for all samples, with diffusive transport occurring at the reaction front (Fig. 20). Based on these results, the timescales of fluid infiltration are constrained to be ~8 h for the mafic granulite, ~1–14 h for the opx–hbl schist, and ~12 h for the opx–hbl gneiss (Table 5).

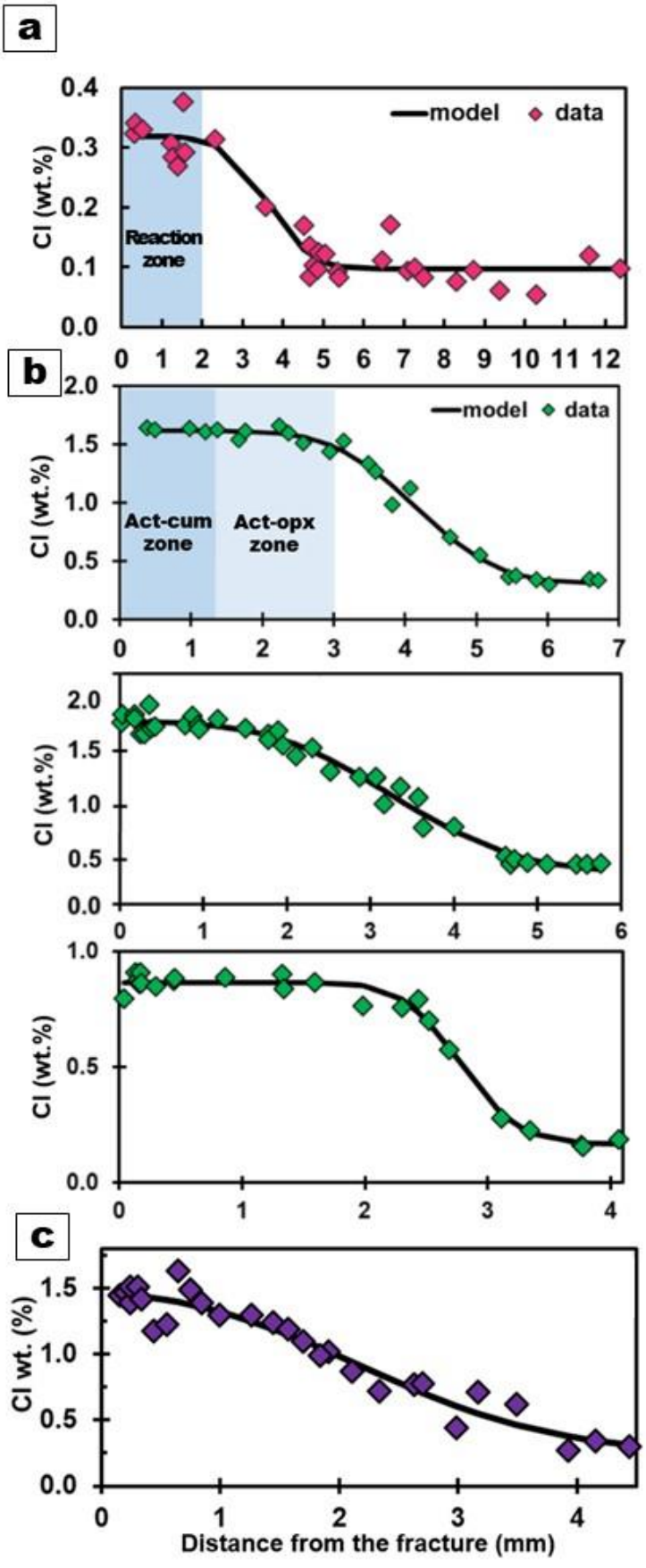
a
model
data
Cl (wt.%)
Reaction zone
b
Act-cum zone
Act-opx zone
Cl wt. (%)
Distance from the fracture (mm)

Fig. 20 Chlorine profiles in apatite from the (a) mafic granulite, (b) opx–hbl schist and in pargasite (b) opx–hbl gneiss. The black lines are modelled fits by reactive transport modelling (Eq. 2).

3.3 Mechanisms and timescales of apatite equilibration with Cl-bearing fluids

Based on existing models of apatite replacement, there are two possible mechanisms for Cl incorporation into apatite: (a) F–Cl–OH exchange by intracrystalline diffusion or (b) replacement of fluorapatite by Cl-bearing hydroxyl-fluorapatite via a dissolution–precipitation mechanism as a result of fluid-induced reactions. However, in the case of F–Cl–OH exchange by intracrystalline diffusion, the diffusion coefficient is too low to lead to Cl transport on such short timescales. The F–Cl–OH diffusion coefficient varies from 10^{-17} m^2/s (700°C and 1 GPa) to 10^{-19} m^2/s (700°C and 1 atm), and is lower at lower temperatures (Cherniak, 2010). These diffusion coefficients are several orders smaller than the effective diffusion coefficients of the matrix ($D_e = \tau\varphi D_0 \sim 10^{-12}$ m^2/s), and cannot result in complete homogenization of the chemistry of the apatite grains (~5–30 μm) within the timescales of diffusion in the matrix on a mm-scale.

Interface-coupled dissolution–precipitation is another possible mechanism that can explain the Cl incorporation into apatite (Kusebauch et al., 2015; Pedrosa et al., 2016). Experimental studies at temperatures close to those of the reaction zones of this study (450–620°C) suggest possible short timescales for replacement: apatite replacement is observed over a distance of ~100 μm from a ~200–350-μm-sized grain at 500–600°C over 300–400 h, and with a 5–10 wt.% NaCl solution (Kusebauch et al., 2015). The smaller grains of apatite in this study (5–30 μm in width) would be replaced for a further shorter timescale (~tens of hours). Therefore, interface-coupled dissolution–precipitation of apatite grains is a plausible mechanism that can explain incorporation of Cl into apatite within the timescale estimated from Cl profiles across the reaction zones (i.e., tens of hours).

The systematic variation of the Cl contents of apatite implies that the fluids coexisted with them possibly changed HCl fugacity. The f_{HCl}/f_{H2O} ratio calculated from the apatite composition and P-T conditions of reaction zones of Cl-bearing fluids (Piccoli and Candela, 1994) decreases with distance from the fracture (Table 3), suggesting that Cl-bearing fluids changed its composition as it reacted with the wall-rock and Cl from the fluids incorporated into apatite.

3.4 Assumptions of the reactive-transport model from the perspective of reaction rate and fluid infiltration rate

The reactive-transport model adopted in this study (Eq. 2) assumes local equilibrium between fluid and solid. As the main Cl-bearing phase is apatite in both the mafic granulite and opx–hbl schist, local equilibrium between fluid and apatite is assumed. This assumption of local equilibrium requires that the surface reaction rate is higher than the transport rate (e.g., Lasaga, 1998; Philpotts and Ague, 2009).

If the surface reaction rate is lower than the transport rate, the reaction only proceeds on the surface of the mineral grains, and the reaction front propagates along the grain boundaries, leaving partly reacted, zoned grains in the reaction zones (e.g., Jonas et al., 2014; Nakatani and Nakamura, 2016; Pedrosa et al., 2016). However, the apatite grains in this study show no detectable chemical zoning (Fig. 14). This texture suggests that the apatite–fluid reaction rate is much higher than the Cl-bearing fluid transport rate. This inference is supported by the rapid apatite replacement by interface-coupled dissolution–precipitation (e.g., Kusebauch et al., 2015).

I suggest that the apatite–fluid surface reaction was effectively faster than the Cl and fluid transport, and local equilibrium was achieved during the apatite–fluid reactions. As such, if the Cl-bearing fluid was present on the apatite grain boundary, then the apatite–fluid reaction is chemically recorded in the apatite grains. Therefore, the timescale estimated from the Cl profiles corresponds to the duration of Cl-bearing fluid activity on an intergranular scale in the reaction zones.

3.5 Effect of microfractures on Cl profiles and fluid transport into the wall rock

Microfractures occur adjacent to the main fracture (Fig. 13 a, b). However, these microfractures are limited in spatial frequency (<1 microfracture/several mm) and were not the main fluid pathway. Hydration along microfractures was limited to widths of 10–30 μm (Fig. 13 b). In contrast, the hydration reactions in the reaction zones occurred mainly along grain boundaries (Figs. 6 and 13 c, d). Therefore, it is suggested that the grain boundaries were the main fluid pathways during formation of the reaction zone. From these observations, advective fluid flow along grain boundaries is inferred to have been the main fluid infiltration mechanism, with minor and localized contributions of rapid advection along microfractures. Therefore, I consider that the timescale obtained from Cl profiles (i.e., tens of hours) corresponds to the duration of fluid activity along grain boundaries. This timescale is not necessarily the same as the timescale of brittle fracturing. Rather, the estimated timescale corresponds to the duration of fluid infiltration into the wall rock, which began during propagation of the main fracture and continued during the formation of the reaction zone.

3.6 Cl incorporation into apatite and amphibole and origin of Cl-bearing fluids.

To constrain fluid composition, I apply composition of apatite in the reaction zones and close to the boundary with the host rock and calculated fugacity ratio and molality from the P-T conditions.

The following equation describes the fugacity ratio as a function of apatite composition and P-T (Piccoli and Candela, 1994):

$$\frac{f_{HCl}^{aq}}{f_{H_2O}^{aq}} = \frac{X_{ClAp}^{Ap}}{X_{HAp}^{Ap} 10^{[0.04661+\frac{2535.8}{T}-\frac{0.0303(P-1)}{T}]}} \quad ,$$

where $\frac{f_{HCl}^{aq}}{f_{H_2O}^{aq}}$ is the fugasity ratio, X_{ClAp}^{Ap} is the Cl content (a.p.f.u) in apatite, $X_{HAp}^{Ap}\rho_f$ is the H content (a.p.f.u) in apatite, and P-T is pressure and temperature estimated for the reaction zone. Next, m_{Cl}^{aq} molality was estimated as (Piccoli and Candela, 1994):

$$m_{Cl}^{aq} = \frac{\frac{X_{ClAp}^{Ap}}{X_{HAp}^{Ap} 18\times 10^{[0.04661+\frac{2535.8}{T}-\frac{0.0303(P-1)}{T}]}}1000}{10^{(-0.63-P\times 0.00035)}}$$

Table 4 fugacity ratio and molality of Cl bearing fluids estimated for the apatite.

	Mafic granulite	Opx-hbl schist		Opx-hbl gneiss	
Parameters	Reaction zone	Act–cum zone	Act–opx zone	Reaction zone	Host rock
$\log\frac{f_{HCl}^{aq}}{f_{H_2O}^{aq}}$	-3.35	-3.67	-4.32	-2.77	-3.38
m_{Cl}^{aq}	7.0	0.6	0.1	59	14

The f_{HCl}/f_{H2O} initial ratio and molality (act–opx zone for the opx-hbl schist and boundary between host rock and reaction zone for the opx-hbl gneiss) calculated from the apatite composition and P-T conditions of reaction zones of Cl-bearing fluids is lower compare to the ratios and molalities near the fractures. Molality variations from 0.1 to 0.6 m for the opx-hbl schist and from 14 to 59 m for the opx-hbl gneiss suggest that apatite changed composition as it reacted with the Cl-bearing fluids and Cl from the fluids incorporated into apatite (Table 4). Calculated molalities were compared to halite

saturation at reaction zone P-T conditions (Aranovich and Newton, 1996) and to the molalities of the altered oceanic crust and seawater (Reynard, 2016; Reynard et al., 2011). Mafic granulite (7 m) and opx–hbl schist (0.1-0.6 m) molalities are comparable to the seawater and altered oceanic crust, while opx–hbl gneiss (14-59 m) is possibly may be related to magmatic fluids (Fig.21). Hydrous fluids transported from the subduction zone may be the origin of Cl-bearing fluids in the mafic granulite and opx–hbl schist, and hydrous magmatic fluids or melt possibly the source in case of the opx–hbl gneiss.

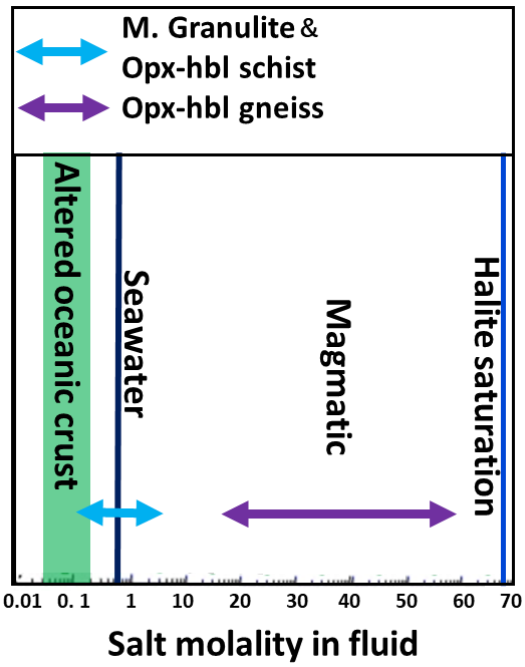

Fig. 21 Molalities of mafic granulite and opx–hbl schist (light blue arrow) and opx–hbl gneiss (purple arrow) compared to halite saturation (light blue line), seawater (dark blue line) and altered oceanic crust (green region).

Mafic granulite, opx–hbl schist and opx–hbl gneiss are located close to the Sør Rondane Suture (Osanai et al., 2013, 1992), which is a shear zone in the SW terrane. It is suggested that Cl-bearing fluids possibly came from the shear zone located nearby (Higashino et al., 2013, 2019a; Kawakami et al., 2017) or from solidified granitic melt (Uno et al., 2017). Cl content measurements in the apatite in the partial melt (0.06-0.08 wt.%) and in the reaction zone (0.13 wt.%) in the opx–hbl gneiss samples, suggest that partial melt is unlikely been the source of Cl-bearing fluid infiltration. This suggests that the Cl-bearing fluids might have migrated from the nearby solidifying granite and/or

shear zones via fractures, which may have formed as a result of a short seismic event.

3.7 Conclusion

In this chapter, I constrained timescales of fluid infiltration by analysing fluid mobile elemental profiles and applied reactive transport model with local equilibrium. First, dominant reactive transport mechanism was identified by the model. I described assumptions of the reactive-transport model from the perspective of reaction rate and fluid infiltration rate. For all analysing profiles advection was the dominant fluid infiltration mechanism, with diffusive transport occurring at the reaction front. Then, Cl partition coefficient for the opx–hbl gneiss was determined because Cl was incorporated into apatite and pargasite and modal variation could not be ignored. I recalculate Cl partitioning coefficient for apatite and pargasite and applied it to estimate timescales. In case of mafic granulite and opx–hbl schist Cl was mostly incorporated into only apatite, therefore partition coefficients from the literature were used. Based on these results, the timescales of fluid infiltration are constrained to be ~8 h for the mafic granulite, ~1–14 h for the opx–hbl schist, and ~12 h for the opx–hbl gneiss. This timescale corresponds to the duration of fluid infiltration into the wall rock, which began during propagation of the main fracture and continued during the formation of the reaction zone. Mechanism and timescales of the equilibration with cl-bearing fluids are suggested. Interface-coupled dissolution–precipitation of apatite grains is a plausible mechanism that can explain Cl incorporation of into apatite for the mafic granulite and opx–hbl schist. Timescale estimated from the tracers profiles corresponds to the duration of Cl-bearing fluid activity on an intergranular scale in the reaction zones.

Chapter 4
Permeability during fluid infiltration

4. Permeability during fluid infiltration

4.1 Introduction

Permeability of crustal rocks is heterogeneous, exhibits large variations from 10^{-19} m^2 in areas of contact metamorphism (Hanson, 1995) to 10^{-18}–10^{-15} m^2 in geothermal–metamorphic areas (Ingebritsen and Manning, 2010). However, recent studies suggest permeability evolution with time during fluid infiltration events, describing processes starting from fluid pressures rising and leading to increase of permeability and formation of fluids pathways, following by sealing and repeated decreasing of permeability (Nakajima and Uchida, 2018; Taetz et al., 2018). For example, seismic clustering can enhanced crustal permeability up to 10^{-15}–10^{-14} m^2 (e.g., Cox, 2016; Nakajima and Uchida, 2018; Okada et al., 2015). Dynamic changes in the fluid pressure and permeability in the middle–lower crust are important to further understanding the relationship between fluid infiltration and fracturing and explaining crust deformation.

In this chapter, I describe methodology connecting fluid infiltration timescales and fluid pressure gradients to estimate permeability from fluid-rock reaction zones by reactive-transport modeling of trace element profiles. First step is to estimate fluid pressure gradients from water activities of reaction zones by pseudosection analysis. Next, I describe how to estimate permeability if fluid pressure gradients are known. Finally, I suggest permeability estimations for fractures and time-averaged permeability of fractured crust. I provide numerical estimations for the different stages of permeability evolution cycle and describe how short time fluid infiltration is possible in low-permeable rocks.

4.2. Permeability of the host rock

Permeability in the reaction zones was estimated based on Darcy's Law as follows:

$$J_{ave} = V_x\phi = -\frac{\kappa}{\eta}\left(\frac{\Delta P}{\Delta x}\right) \qquad (Eq.4)$$

where κ is the permeability (m^2), η is the viscosity (Pa s), Δx is the width of the hydration reaction zone estimated from Cl profiles (m), and $\frac{\Delta P}{\Delta x}$ is the pressure gradient (Pa/m). Viscosities of aqueous fluids were derived from the pure H_2O viscosity of the 2008 IAPWS formulation (up to 1 GPa and 900°C; Huber et al., 2009). Under the assumed *P–T* conditions, the values are 1.10 ± 0.08 $\times 10^{-4}$ Pa·s for mafic granulite (620 ± 60°C and 0.50 ± 0.05 GPa) and 1.09 ± 0.13 $\times 10^{-4}$ Pa·s for opx–hbl schist (450 ± 50°C and 0.30 ± 0.05 GPa). Addition of solutes (i.e., SiO_2; Hack and Thompson, 2011) has only a minor effect on aqueous fluid viscosity in the *P–T* ranges considered in this study.

Fluid pressures between the reaction zones and host mafic granulite, between the actinolite–orthopyroxene zones and host opx–hbl schist, and between the reaction zone and host opx–hbl gneiss were calculated from the fugacity (*f*) and estimated H_2O activity (Fig. 22 a) with following equation (e.g., Anderson, 2005; Goto and Banno, 1990):

$$\frac{f(P_f, T)}{f(P_l, T)} = a_{H_2O}, \qquad (Eq.5)$$

where P_f is the fluid pressure, P_l is the lithostatic pressure, T is the reaction zone temperature, and a_{H_2O} is the H_2O activity. To constrain the H_2O activity from pseudosections, I used bulk rock compositions for the mafic granulite, actinolite–orthopyroxene zone, and opx–hbl schist (Table 1; Fig. 23). For the mafic granulite, I constrained the H_2O activity from the lower a_{H2O} bound of amphibole stability field, because the reaction front of the reaction zone is characterized by the appearance of amphibole (Fig. 23). The calculated H_2O activity is ca. 0.18 (Fig. 23). For the opx–hbl schist, the upper a_{H2O} bound of orthopyroxene stability field representing the boundary between the actinolite–cummingtonite and actinolite–orthopyroxene zones was used, because orthopyroxene is almost replaced by actinolite in the actinolite–cummingtonite zone (Fig. 24). The calculated H_2O activity is ca. 0.06 (Fig. 24 b). I also used the upper

a_{H2O} bound of clinopyroxene stability field between the actinolite–orthopyroxene zone and host rock, because clinopyroxene is only present in the host rock (Fig. 9 g). The calculated H_2O activity is ca. 0.03 at the pressure of interest (Fig.24 c). For the opx–hbl gneiss, I constrained the H_2O activity from the upper a_{H2O} bound of orthopyroxene stability field representing the boundary between the reaction zone and the host rock, because in the reaction zone orthopyroxene is almost replaced by amphibole (Fig. 8). The calculated H_2O activity is ca. 0.32 (Fig. 25). To constrain fluid pressure gradient, I also used the water activity of the stable mineral assemblages of the reaction zone constrained for the estimated P-T conditions (Fig. 26). The calculated H_2O activity is ca. 0.79- 1.00. However, presence of Cl in the fluid in the reaction zone may influence activity and lowering it. For now, it is impossible to input Cl into present solution models, for this reason calculations may represent higher water activity compare to real numbers (Figs. 25, 26).

For the opx–hbl schist, the fluid pressure gradient was calculated as the difference between the fluid pressure of upper a_{H2O} bound of the orthopyroxene stability field (P_f^0) and that of the clinopyroxene stability field (P_f^1), which corresponds to the estimated H_2O activity.

For the opx–hbl gneiss, the fluid pressure gradient was calculated as the difference between the fluid pressure of upper a_{H2O} bound of the reaction zone stability field (P_f^1) and that of the orthopyroxene stability field (P_f^0).

The final equation for the fluid pressure gradient $\frac{\Delta P}{\Delta x}$ (Pa/m) is:

$$\frac{\Delta P}{\Delta x} = \frac{P_f^0 - P_f^1}{\Delta x} \qquad (Eq. 6)$$

In the case of the mafic granulite, the permeability for the boundary between the hydrous–anhydrous zones is $8.8^{+31.8}_{-6.9} \times 10^{-22}$ m^2, and in the opx–hbl schist it is 2.1 × 10^{-22} to 4.0 × 10^{-20} m^2, while in the opx–hbl gneiss it is $6.8^{+23.2}_{-5.3} \times 10^{-24}$ m^2 (Table 6).

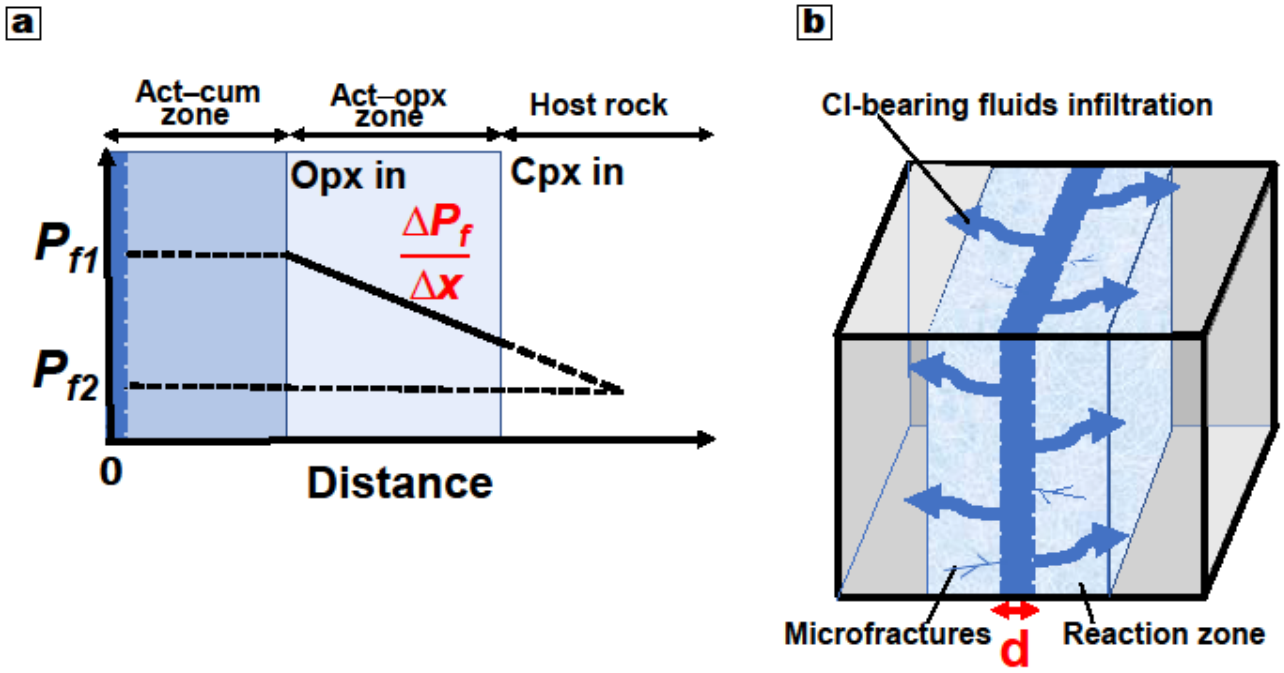

Fig 22 Schematic model used for the estimation of permeabilities in the (a) reaction zones and (b) fractures. P_{f1} and P_{f2} are the fluid pressures defined by the stability of orthopyroxene and clinopyroxene, respectively.

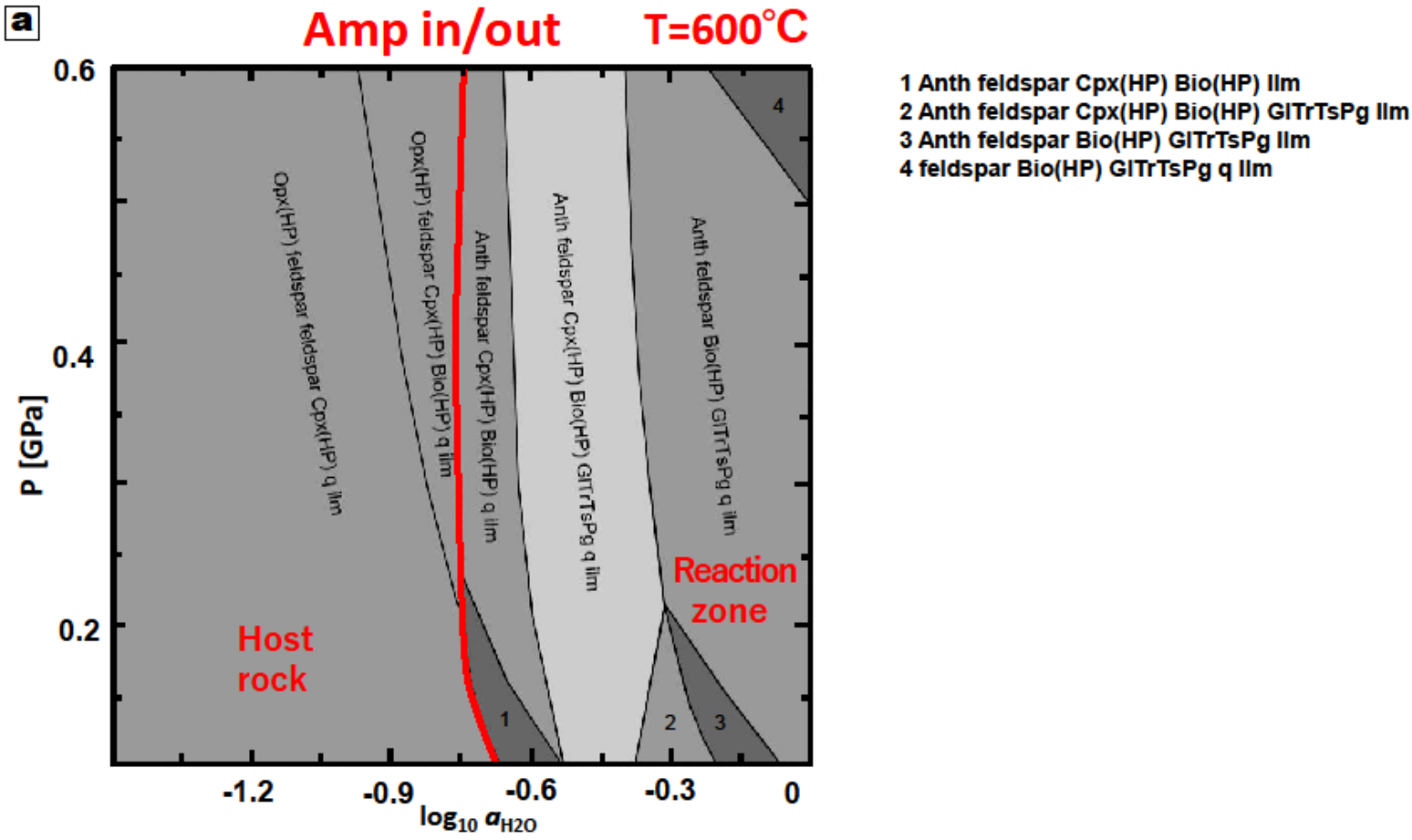

Fig 23 Pseudosections (P versus $\log_{10}$ [a_{H2O}]) for the (a) mafic granulite.

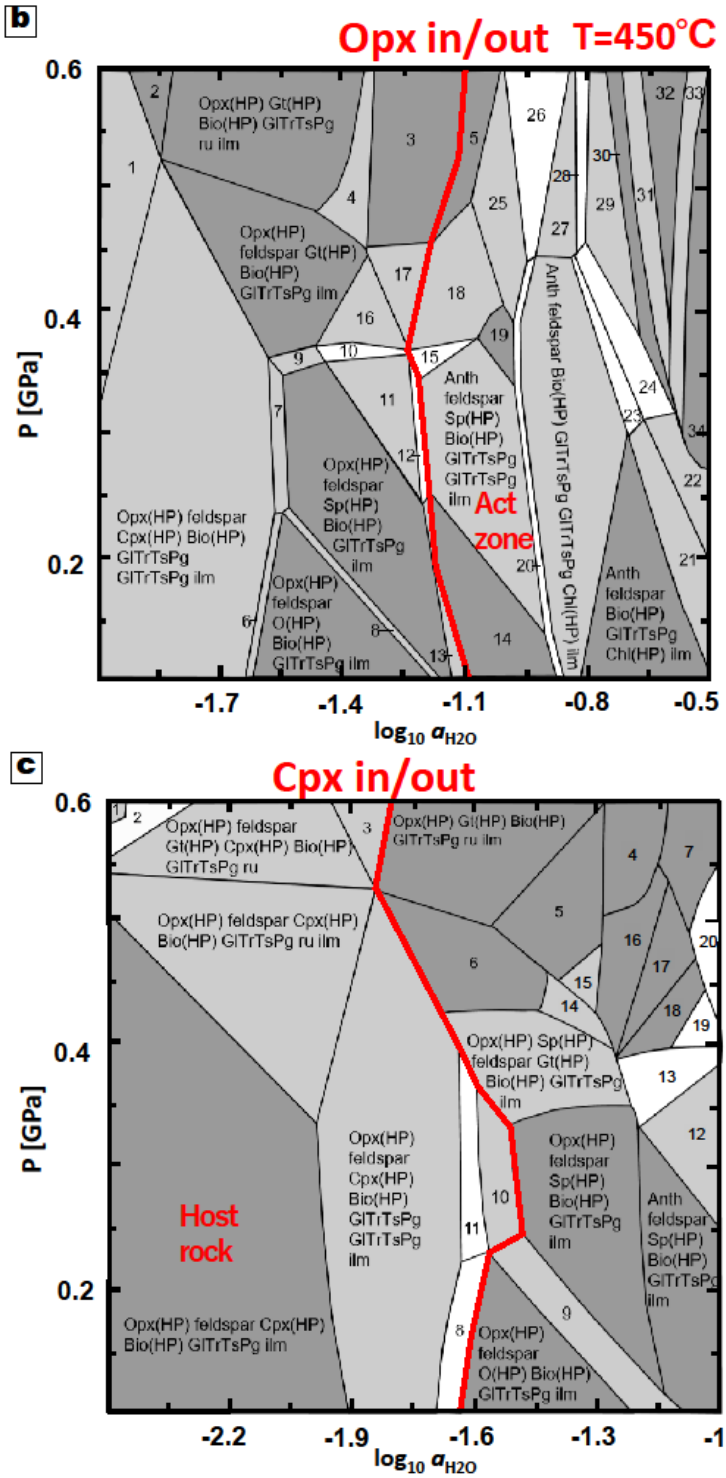

1 Opx(HP) feldspar Cpx(HP) Bio(HP) GlTrTsPg GlTrTsPg ru
2 Opx(HP) Gt(HP) Cpx(HP) Bio(HP) GlTrTsPg ru
3 Opx(HP) Anth Gt(HP) Bio(HP) GlTrTsPg ilm
4 Opx(HP) Anth Gt(HP) Bio(HP) GlTrTsPg ky ilm
5 Anth Gt(HP) Bio(HP) GlTrTsPg Chl(HP) ilm
6 Opx(HP) feldspar O(HP) Cpx(HP) Bio(HP) GlTrTsPg ilm
7 Opx(HP) feldspar Sp(HP) Cpx(HP) Bio(HP) GlTrTsPg ilm
8 Opx(HP) feldspar O(HP) Sp(HP) Bio(HP) GlTrTsPg ilm
9 Opx(HP) feldspar Sp(HP) Gt(HP) Bio(HP) GlTrTsPg ilm
10 Opx(HP) feldspar Sp(HP) Gt(HP) Bio(HP) GlTrTsPg GlTrTsPg ilm
11 Opx(HP) feldspar Sp(HP) Bio(HP) GlTrTsPg GlTrTsPg ilm
12 Opx(HP) Anth feldspar Sp(HP) Bio(HP) GlTrTsPg GlTrTsPg ilm
13 Opx(HP) Anth feldspar Sp(HP) Bio(HP) GlTrTsPg ilm
14 Anth feldspar Sp(HP) Bio(HP) GlTrTsPg ilm
15 Anth feldspar Sp(HP) Gt(HP) Bio(HP) GlTrTsPg GlTrTsPg ilm
16 Opx(HP) feldspar Gt(HP) Bio(HP) GlTrTsPg GlTrTsPg ilm
17 Opx(HP) Anth Gt(HP) Bio(HP) GlTrTsPg GlTrTsPg ilm
18 Anth Sp(HP) Gt(HP) Bio(HP) GlTrTsPg GlTrTsPg ilm
19 Anth Sp(HP) Bio(HP) GlTrTsPg GlTrTsPg ilm
20 Anth feldspar Sp(HP) Bio(HP) GlTrTsPg GlTrTsPg Chl(HP) ilm
21 Anth feldspar Bio(HP) GlTrTsPg Chl(HP) ilm
22 Anth feldspar Bio(HP) GlTrTsPg Chl(HP) ru ilm
23 Anth feldspar Bio(HP) GlTrTsPg Chl(HP) ilm
24 Anth feldspar Bio(HP) GlTrTsPg GlTrTsPg Chl(HP) ru ilm
25 Anth Gt(HP) Bio(HP) GlTrTsPg GlTrTsPg Chl(HP) ilm
26 Anth Gt(HP) Bio(HP) GlTrTsPg GlTrTsPg Chl(HP) ky ilm
27 Anth Bio(HP) GlTrTsPg GlTrTsPg Chl(HP) ky ilm
28 Anth Bio(HP) GlTrTsPg GlTrTsPg Chl(HP) ky ru ilm
29 Anth Bio(HP) GlTrTsPg GlTrTsPg Chl(HP) ru ilm
30 Anth Bio(HP) GlTrTsPg GlTrTsPg Chl(HP) ru
31 Anth Bio(HP) GlTrTsPg GlTrTsPg Chl(HP) q ru
32 Anth Bio(HP) GlTrTsPg Chl(HP) q ru
33 Anth Bio(HP) GlTrTsPg Chl(HP) q ru ilm
34 Bio(HP) GlTrTsPg Chl(HP) q ru ilm

1 Opx(HP) feldspar Gt(HP) Cpx(HP) GlTrTsPg ky ru
2 Opx(HP) feldspar feldspar Gt(HP) Cpx(HP) Bio(HP) GlTrTsPg ru
3 Opx(HP) Gt(HP) Cpx(HP) Bio(HP) GlTrTsPg GlTrTsPg ru
4 Opx(HP) Anth Gt(HP) Bio(HP) GlTrTsPg ilm
5 Opx feldspar Gt(HP) Bio(HP) GlTrTsPg ky ilm
6 Opx feldspar Gt(HP) Bio(HP) GlTrTsPg ilm
7 Anth Gt(HP) Bio(HP) GlTrTsPg Chl(HP) ilm
8 Opx(HP) feldspar O(HP) Cpx(HP) Bio(HP) GlTrTsPg GlTrTsPg ilm
9 Opx(HP) feldspar O(HP) Sp(HP) Bio(HP) GlTrTsPg ilm
10 Opx(HP) feldspar Sp(HP) Cpx(HP) Bio(HP) GlTrTsPg ilm
11 Opx(HP) feldspar Sp(HP) Cpx(HP) Bio(HP) GlTrTsPg GlTrTsPg ilm
12 Anth feldspar Sp(HP) Bio(HP) GlTrTsPg GlTrTsPg ilm
13 Anth feldspar Sp(HP) Gt(HP) Bio(HP) GlTrTsPg GlTrTsPg ilm
14 Opx(HP) feldspar Gt(HP) Bio(HP) GlTrTsPg cor ilm
15 Opx(HP) Gt(HP) Bio(HP) GlTrTsPg ky cor ilm
16 Opx(HP) Anth Gt(HP) Bio(HP) GlTrTsPg cor ilm
17 Anth Sp(HP) Gt(HP) Bio(HP) GlTrTsPg ilm
18 Anth Sp(HP) Gt(HP) Bio(HP) GlTrTsPg GlTrTsPg ilm
19 Anth Sp(HP) Gt(HP) Bio(HP) GlTrTsPg GlTrTsPg cor ilm
20 Anth Gt(HP) Bio(HP) GlTrTsPg GlTrTsPg Chl(HP) cor ilm

Fig 24 Pseudosections (P versus $\log_{10}$ [a_{H2O}]) for the (b) actinolite–cummingtonite zone in opx–hbl schist and (c) host rock in opx–hbl schist.

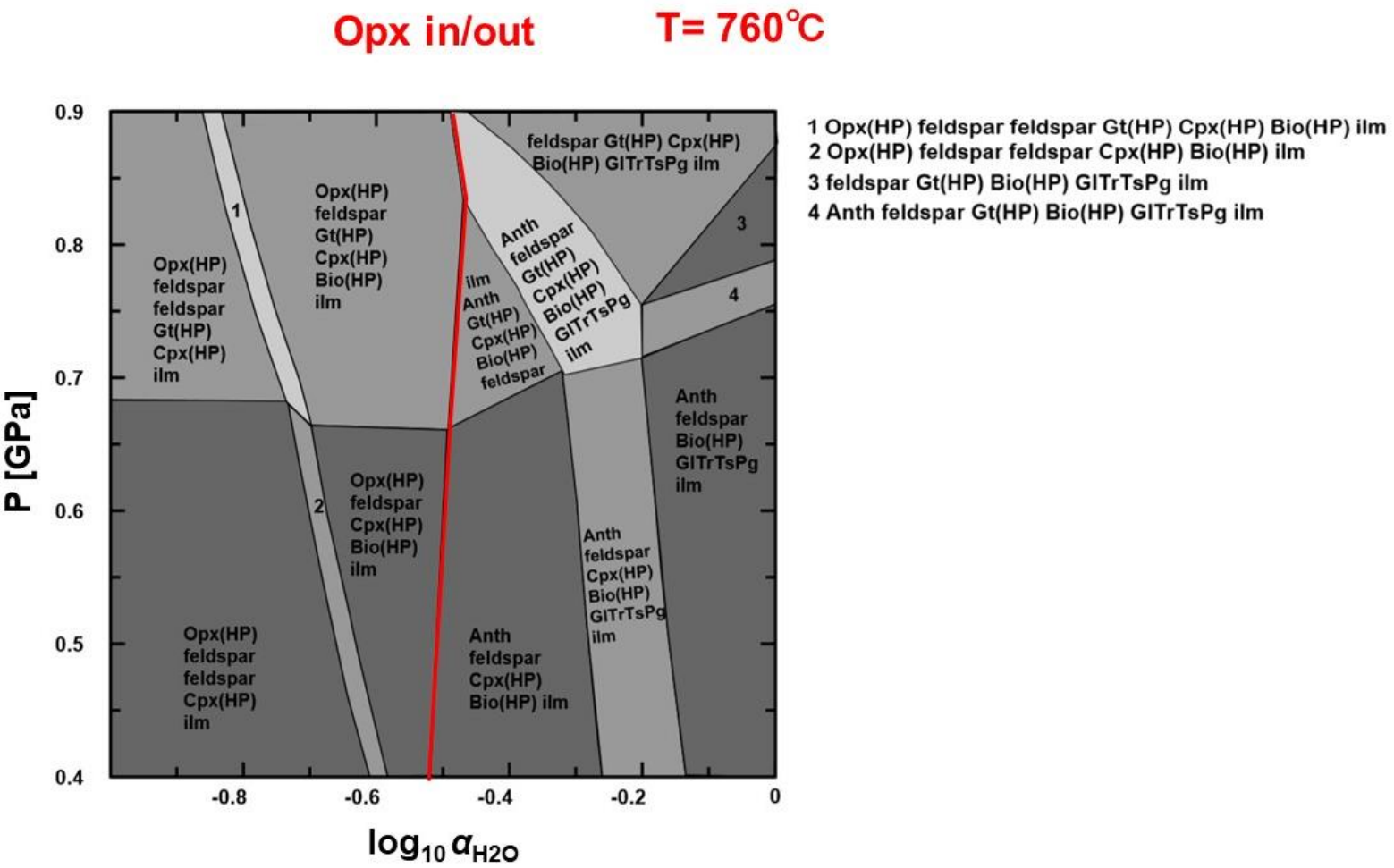

Fig 25 Pseudosections (P versus $\log_{10}$ [a_{H2O}]) for the host rock in opx–hbl gneiss.

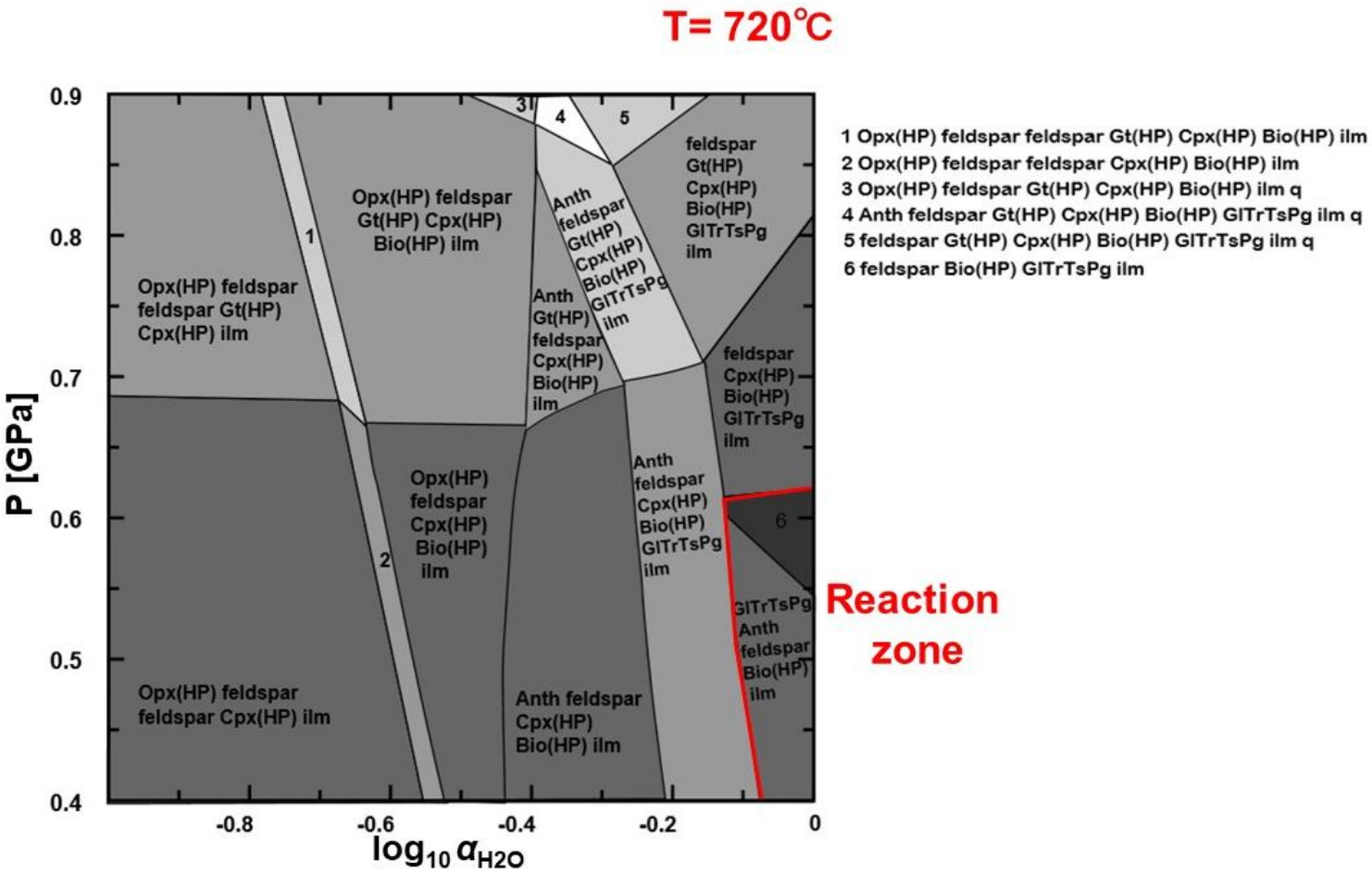

Fig 26 Pseudosections (P versus $\log_{10}$ [a_{H2O}]) for the reaction zone in opx–hbl gneiss.

Table 5 Calculated permeabilities of the host rock mafic granulite, opx–hbl schist, and opx–hbl gneiss. Parameters and constants used in these calculations.

	Mafic granulite	Opx–hbl schist			Opx–hbl gneiss
Parameters	**A**	**B**	**B1**	**B2**	**C**
a [mm]	3.51 ± 0.33	4.04 ± 0.07	3.09 ± 0.11	2.75 ± 0.04	1.93 ± 0.23
d [mm]	0.63 ± 0.21	0.66 ± 0.07	0.91 ± 0.13	0.27 ± 0.04	0.93 ± 0.31
L [mm]	12	6	6	4	4
C_b [wt.%]	0.32 ± 0.01	1.62 ± 0.02	0.24 ± 0.00	0.86 ± 0.01	1.47 ± 0.05
C_0 [wt.%]	0.10 ± 0.01	0.31 ± 0.04	0.03 ± 0.01	0.17 ± 0.02	0.27 ± 0.14
Pe#	107 ± 73	56 ± 12	22 ± 6	149 ± 41	9 ± 6
t [h]	$7.9\ ^{+40.5}_{-6.6}$	$7.4\ ^{+33.1}_{-6.0}$	$14.4\ ^{+65.2}_{-11.8}$	$1.3\ ^{+5.7}_{-1.1}$	$11.6\ ^{+58.9}_{-9.7}$
V_x [m/s]	$1.8 \pm 1.4 \times 10^{-4}$	$1.6 \pm 0.8 \times 10^{-4}$	$6.2 \pm 3.2 \times 10^{-5}$	$6.2 \pm 3.2 \times 10^{-4}$	$5.1 \pm 4.0 \times 10^{-5}$
J_{ave} [m/s]	$1.1\ ^{+3.5}_{-0.8} \times 10^{-8}$	$1.0\ ^{+2.5}_{-0.7} \times 10^{-8}$	$3.9\ ^{+9.9}_{-2.6} \times 10^{-9}$	$3.9\ ^{+9.9}_{-2.6} \times 10^{-8}$	$3.3\ ^{+9.7}_{-2.5} \times 10^{-9}$
P_{fluid}^0 [MPa]	–	5.5±0.9	5.5±0.9	5.5±0.9	485±31
P_{fluid}^1 [MPa]	93±23	2.7±0.3	2.7±0.3	2.7±0.3	278±25
ΔP [MPa]	2.8±0.9	2.8±0.9	2.8±0.9	2.8±0.9	210±65
Δx [mm]	2 ± 1	6 ± 4	6 ± 4	6 ± 4	4 ± 2
$\Delta P/\Delta x$ [MPa/mm]	1.4±0.8	0.5±0.3	0.5±0.3	0.5±0.3	52.5±26.3
k [m^2]	$8.8\ ^{+31.8}_{-6.9} \times 10^{-22}$	$2.3\ ^{+7.7}_{-1.8} \times 10^{-21}$	$9.1\ ^{+30.7}_{-7.0} \times 10^{-22}$	$9.2\ ^{+30.7}_{-7.1} \times 10^{-21}$	$6.8\ ^{+23.2}_{-5.3} \times 10^{-24}$
Constants					
D_0 [m^2/s]	$4.0 \pm 0.5 \times 10^{-8}$		$3.3 \pm 0.6 \times 10^{-8}$		$4.6 \pm 0.5 \times 10^{-8}$
K_v	$11.0\ ^{+24}_{-7.5}$		$15.3\ ^{+32}_{-10.5}$		$14.2\ ^{+30.7}_{-9.7}$
φ	$6\ ^{+14}_{-4} \times 10^{-5}$		$6\ ^{+14}_{-4} \times 10^{-5}$		$6\ ^{+14}_{-4} \times 10^{-5}$
τ	0.5 ± 0.2		0.5 ± 0.2		0.5 ± 0.2
η [Pa s]	$1.10 \pm 0.08 \times 10^{-4}$		$1.09 \pm 0.13 \times 10^{-4}$		$1.10 \pm 0.08 \times 10^{-4}$

4.3. Permeability of the fractures

The surface topography of fractures is complex (Watanabe et al., 2008) and here I assumed that the fracture surfaces were parallel and planar. A schematic illustration of the fracture and reaction zone is shown in Fig. 22 b.

Permeability of the fracture was estimated based on the Poiseuille law as follows:

$$k = \frac{d^2}{12} \qquad \text{(Eq. 7)}$$

where d (mm) is the fracture aperture. Fracture width varies from 0.30 to 0.40 mm for the mafic granulite, 0.15 to 0.30 mm for the opx–hbl schist, and 0.20 to 0.40 mm for the opx–hbl gneiss. The fracture permeability varies from ~10^{-9} to 10^{-8} m^2 for all samples. The permeability of the microfractures in the opx–hbl schist is lower (~10^{-12} to 10^{-11} m^2). The calculated parameters are summarized in Table 6.

4.4. The overall permeability of the crust

The overall permeability of the crust is determined by the permeability of single fractures and the spatial frequency of such fractures per assumed cross-section. For example, a single fracture with a 0.1 mm aperture (d) and permeability of 10^{-9} m^2 (k_{frac}) with spacing (s) of 100 m will give a spatially averaged crustal permeability as follows: $k_{ave} = k_{frac}\left(\frac{d}{s}\right) + k_{wallrock}\left(1 - \frac{d}{s}\right) = \sim 10^{-15}\mathrm{m}^2$. This means that the overall crustal permeability is ~10^{-15} m^2 under the assumption of a 100 m fracture spacing. This demonstrates the importance of fractures and their networks in the crust in terms of permeability fluctuations. Given that fractures observed in outcrops (mm- to cm-scale spacing; Fig. 27) may have formed at different times, it is difficult to estimate the spacing of fractures that were active during a certain period of fluid activity. Nevertheless, a spacing of active fractures in the order of 0.1–1000 m would be a reasonable assumption. Irrespective of the spacing of fractures in the range of 0.1–1000 m, the generation of fractures can significantly enhance the permeability of the local crust (~100 m to km-scale) by several orders of magnitude (k_{ave} ~ 10^{-16}–10^{-10} m^2).

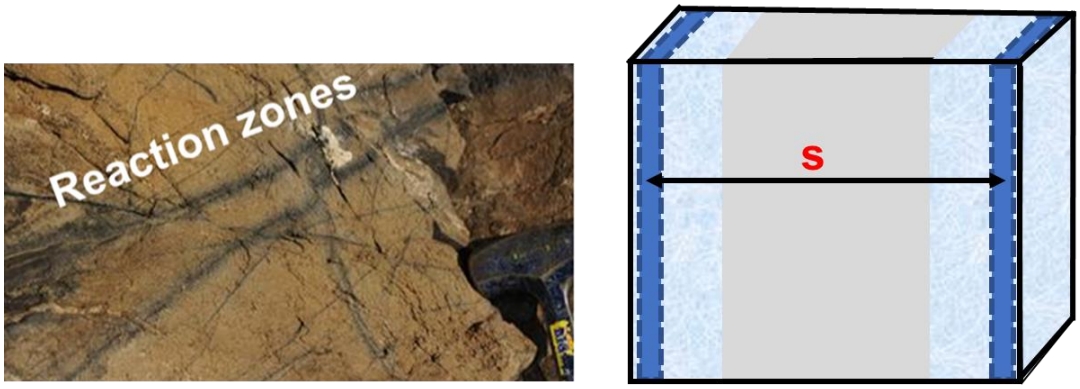

Fig. 27 Schematic model used for the estimation of overall permeability of the crust.

4.5. Time integrated fluid flux through reaction zone and fracture

Time-integrated fluid fluxes through the reaction zone Q_{hyd} (m) and $Q_{cl\ tr}$ (m) were estimated and compared to time-integrated fluid flux through the fracture Q_{fr} (m) to understand how much fluids were transported by them.

Estimation of time-integrated fluid flux requires the reaction zone volume $V_{r.z}$ (L_1 L_2 d) to be assumed, where L_1 (m) is the fracture length, L_2 (m) is the fracture height, and d (m) is the reaction zone width. The fracture length and height were based on outcrop photographs. I used 10–100 × 10–100 m for all samples (Fig. 28 a).

The time-integrated fluid flux was estimated applying Darcy's Law. I assumed that the total amount of fluid flux passing through the cross-section area in the direction toward the host rock parallel to the fracture. (Fig. 28 a) The time-integrated hydration fluid flux equivalent to the volume of fluid consumed to form reaction zones along the fractures. The time-integrated hydration fluid flux is estimated from the volume of the reaction zone ($V_{r.z}$) as:

$$Q_{hyd} = \frac{V_{r.z} C_{H_2O} \Delta t}{L_1 L_2 \rho_{H_2O} \Delta t} = \frac{C_{H_2O} d}{\rho_{H_2O}} \qquad \text{(Eq. 8)}$$

where c_{H_2O} (g/cm^3) is the average H_2O content of the reaction zone (Fig. 28 a) calculated from the hydrous mineral mode, ρ_{H_2O} is H_2O density (g/cm^3), and Δt is the estimated fluid infiltration time.

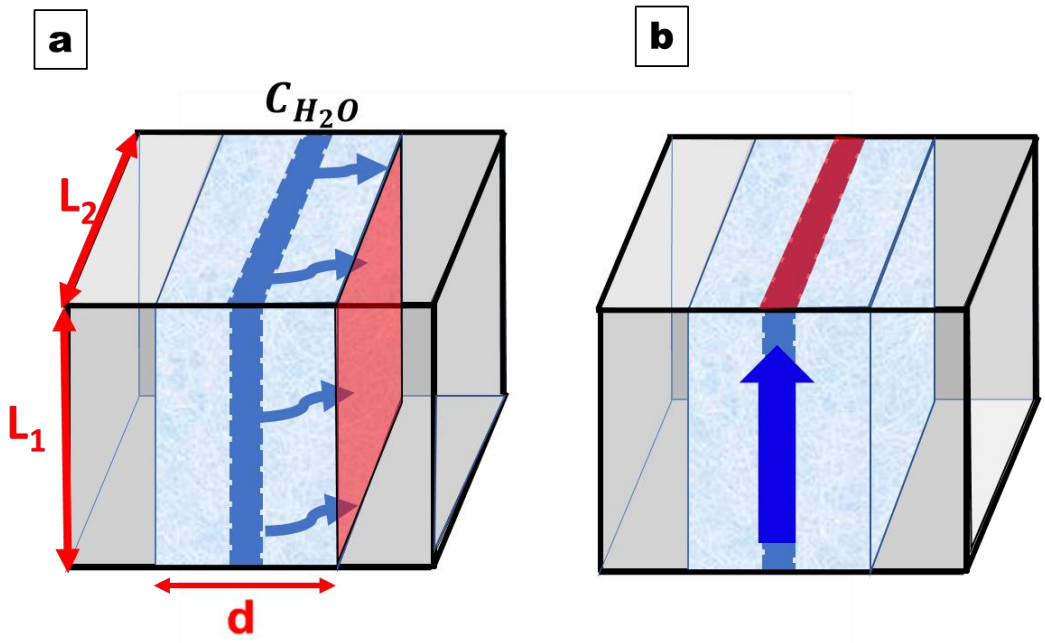

Fig. 28 Schematic model used for the estimation of time-integrated fluid flux through the reaction zone (a) and through the fracture (b).

Next, flux required for Cl transport was calculated as:

$$Q_{cl\,tr} = \mathrm{V_x}\phi\Delta t \qquad \text{(Eq. 9)}$$

Finally, I estimated fluid flux in the direction of the fracture propagation Q_{fr} (Fig. 28 b) as:

$$Q_{fr} = t\frac{k_{fr}}{\eta}\left(\frac{\Delta \mathrm{P}}{\Delta \mathrm{x}}\right) \qquad \text{(Eq. 10)}$$

Time-integrated fluid fluxes log Q_{hyd} are -4.2 m for the mafic granulite, -3.8 m for the hbl–opx schist, and -3.3 m for the hbl–opx gneiss (Table 7). Flux required for Cl transport log $Q_{cl\,tr}$ are same order compare to Q_{hyd}, -3.5 m for the mafic granulite, -3.6 – -3.7 m for the hbl–opx schist, and -3.9 – -4.7 m for the hbl–opx gneiss. Time-integrated fluid flux through the fracture is much higher, suggesting that much amount of fluid was transported through the fracture, and much less was stored in the reaction zones (Fig 29). The calculated parameters are summarized in Table 7 and fig. 29.

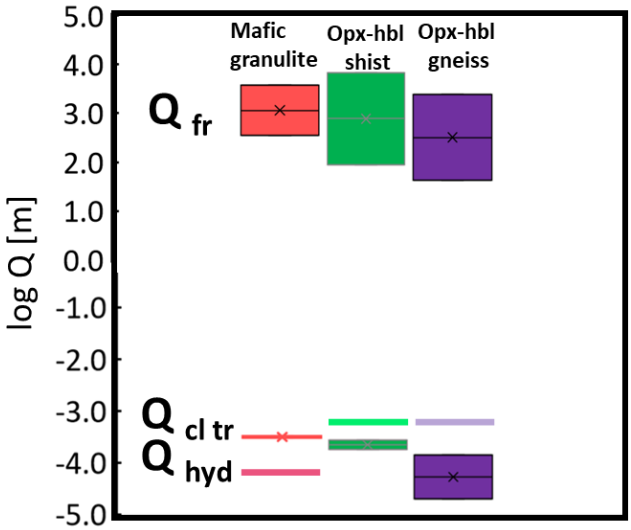

Fig. 29 Time integrated hydration fluid flux Q_{hyd} and flux required for Cl transport $Q_{cl\ tr}$ through the reaction zone compared to time-integrated fluid flux through the fracture Q_{fr}

Table 6 Calculated permeabilities of fractures (k_{fr}) and spatio-averaged fractured crust (k_{ave}) in the mafic granulite, opx–hbl schist, and opx–hbl gneiss and the parameters and constants used in these calculations.

Parameters	Mafic granulite	Opx–hbl schist	Opx–hbl gneiss
δ [mm]	0.30–0.40	0.15–0.30	0.20–0.40
s [m]	0.1–1000	0.1–1000	0.1–1000
k_{frac} [m^2]	7.5–13×10^{-9}	1.9–7.5×10^{-9}	3.3–13×10^{-9}
$k_{wallrock}$ [m^2]	$8.8^{+31.8}_{-6.9} \times 10^{-22}$	$0.2-40 \times 10^{-21}$	$6.8\ ^{+23.2}_{-5.3} \times 10^{-24}$
k_{ave} [m^2]	2.3×10^{-15}–5.3×10^{-11}	2.8×10^{-16}–2.3×10^{-11}	6.7×10^{-16}–5.3×10^{-11}

Table 7 Calculated hydration flux (Q_{hyd}), flux required for Cl transport ($Q_{cl\ tr}$) and flux through the fracture (Q_{fr}) in the mafic granulite, opx–hbl schist, and opx–hbl gneiss , and the parameters and constants used in these calculations.

Parameters	Mafic granulite	Opx–hbl schist	Opx–hbl gneiss
L_1 [m]	10–100	10–100	10–100
L_2 [m]	10–100	10–100	10–100
d [mm]	2.0	4.0	4.0
V_{rz} [m^3]	0.2–20	0.4–40	0.4–40
C_{H2O} [g/cm^3]	3.0×10^{-2}	8.0×10^{-2}	0.12
log Q_{hyd} [m^3/m^2]	-4.2	-3.8	-3.3
log $Q_{cl\ tr}$ [m^3/m^2]	-3.5	-3.6 – -3.7	-3.9 – -4.7
log Q_{fr} [m^3/m^2]	2.5 – 3.6	1.9 – 3.8	1.6 – 3.4

4.6 Conclusion

In this chapter I describe how to estimate fluid pressure gradient by thermodynamic modeling and apply them to calculate wall rock permeability. I also provide estimations for the single fracture and spatially averaged crustal permeabilities for short timescales of fluid infiltration to explain dynamical changes and fracturing in the crust. Finally I estimated time-integrated fluid fluxes through the reaction zone (hydration flux Q_{hyd} and flux required for Cl transport $Q_{cl\ tr}$) and compared them to the time-integrated fluid fluxes through the fracture. Thermodynamic modelling and Darcy's law are main methods applied. In the case of the mafic granulite, the wall rock permeability is $8.8^{+31.8}_{-6.9} \times 10^{-22}$ m^2, and in the opx–hbl schist it is 2.1×10^{-22} to 4.0×10^{-20} m^2, while in the opx–hbl gneiss it is $6.8\,^{+23.2}_{-5.3} \times 10^{-24}$ m^2. Permeability of the fractures is several orders higher, varies from ~10^{-9} to 10^{-8} m^2 for all samples. I also provide overall permeability of the crust which was determined by the permeability of single fractures and the spatial frequency of such fractures per assumed cross-section resulting in 10^{-16}–10^{-10} m^2. Time-integrated hydration flux and flux required for Cl transport are same order, much lower than time-integrated fluid flux through the fracture Q_{fr} suggesting much more amount of H_2O transported through the fracture compare to the reaction zone.

Chapter 5
Dynamic permeability evolution in the crust

5. Dynamic permeability evolution in the crust

5.1 Introduction

In this chapter I discuss relationship between trace elements transport distance, hydration reactions progress, and elemental mass transfer and suggest reaction zone formation mechanism in relation to Cl-beraing fluid infiltration. Hydration reactions also can be controlled by fluid pressure. I suggest that increasing Cl transport distances is correspond to hydration reactions and consistent with the simultaneous formation of Cl profiles, and transfer of major elements. Next, I describe spatiotemporal evolution of reaction zone formation and provide evidence to support idea that fractures were main pathways for fluids, and that permeability evolution from low-permeable wall rock to the higher permeable crust is exist in the crust. I describe fluid cycle starting from accumulation of fluids in the low-permeability rocks leading to an increase in fluid pressure (i.e., the pre-fracturing stage) and fracturing (i.e., the fracturing stage). The fluid flux may have been limited resulting in a short duration of fluid infiltration as suggested from the fluid fluxes estimations. After fracturing, the permeability increases, and the fluid pressure drops. Final stage is permeability decreasing due to sealing by mineral reactions. Previous estimates of the permeability in the middle–lower crust fall within the range of the host rock and fracture permeabilities.

5.2 Formation mechanism of the hydration reaction zone

The distances of Cl transport (Fig. 12), hydration reaction progress (Fig. 18), and mass transfer of major elements (Figs. 16, 17) were examined to assess the relationships between hydration reaction zone formation, apatite Cl profiles, and estimated timescales. The advective Cl transport distance is larger than the distance of hydration reactions and mass transfer of major elements. In the mafic granulite, the advective Cl transport distance is 3.5 mm (Table 5), and the distance of hydration reactions (Fig. 18) and mass transfer of major elements is ~1 mm (Figs. 16 and 17). In the opx–hbl schist sample B, the advective Cl transport distance is 4.0 mm (Table 5), and the distance of hydration reactions and mass transfer is ~3 mm (Figs. 18 and 16, 17). Given that Cl is relatively compatible in a fluid, the distance of Cl transport is almost equivalent to the infiltration distance of the fluid. The advancement of Cl and fluid transport distances from hydration reactions and mass transport distances can be explained by: (a) differences in transport distances between Cl and major elements; or (b) hydration reactions that controlled by the transport of major elements and/or fluid pressure. As Cl is more compatible in a fluid than are other major elements, it is likely that Cl is transported farther than the other major elements. As the extent of hydration reactions and mass transport distances of major elements are the same, it is suggested that these processes are coupled with each other. In this case, hydration reactions can be rate-limited by the transport of major elements (e.g., Fukuyama et al., 2006; Lichtner et al., 1986). In addition, hydration reactions can be controlled by fluid pressure (e.g., Bröcker, 1990; Jamtveit et al., 1990; Schliestedt and Matthews, 1987), as suggested by a_{H2O} analyses from the pseudosection (Figs. 22, 23, 24, 25). In any case, increasing Cl transport distances as compared with hydration reactions is consistent with the simultaneous formation of Cl profiles, hydration reactions, and transfer of major elements (e.g., Bégué et al., 2019).

The reaction front of opx decomposition is abrupt in both the mafic granulite and opx–hbl schist (Fig. 8). The abrupt and systematic change in mineral assemblage from the fracture to the host rock implies a high reaction rate as compared with the transport rate, and local equilibrium (e.g., Fukuyama et al., 2006; Lichtner et al., 1986). Such a high reaction rate compared with the transport rate is also predicted for low-porosity rocks, based on kinetic analyses of hydrothermal experiments (Oyanagi et al., 2020).

Although hydration reactions on timescales as short as tens of hours are relatively fast compared with previous hydration experiments (e.g., Yardley et al., 2014), the reaction rate is dependent not only on pressure and temperature, but also on fluid chemistry and crystal defects, and can vary significantly, over orders of magnitudes. Water–rock reactions on timescales as short as days to hours have been reported from hydrothermal experiments on the hydration of basalt, serpentinization, carbonation of peridotite, and hydration of periclase (e.g., Gerdemann et al., 2007; Kuleci et al., 2016; Nakatani and Nakamura, 2016; Passarella et al., 2017). Fluid flow can further accelerate water–rock reactions (e.g., Hara and Tsuchiya, 2005; Passarella et al., 2017). Based on the textural observations discussed above, I suggest a high reaction rate as compared with the transport rate and local equilibrium in the reaction zones. Therefore, I estimated local fluid pressure from H_2O activities, and subsequently obtained the fluid pressure gradients in the reaction zones.

5.3 Spatiotemporal evolution of reaction zone formation

Reactions zones in the mafic granulite are ubiquitous on an outcrop scale and crosscut the host rock in planar form (Fig. 5). This suggests that hydration of the mafic granulite (620 ± 60°C; ~0.5 ± 0.05 GPa) occurred through brittle fracturing during cooling from granulite-facies (850 ± 50°C) to amphibolite-facies (450±50°C; ~0.3±0.05 GPa) conditions in the middle crust (Fig. 15). Narrow reaction zones were formed along fractures that were dominantly formed by advection and diffusive replacement close to the host rock , and involved Al_2O_3 and Na_2O removal and K_2O addition (Fig. 16 a). Pyroxene and feldspar were replaced by hydrous minerals such as hornblende and biotite (Figs. 8 and 9).

Formation of opx–hbl schist occurred at ~700°C. Considering the stability field of hornblende, it is likely that hornblende formed by the decomposition of pyroxenes, and opx–hbl schist is possibly the hydration product of mafic granulite. Further hydration had occurred along fractures at amphibolite-facies condition (Fig. 15). Mass transport occurred mostly by advection and diffusion (Fig. 20 b). Primary host rock hydration involved the decomposition of anorthite and formation of muscovite and zoisite symplectites (Fig. 9 e). Subsequently, fluid infiltration caused decomposition of pyroxene, and led to the formation of actinolite and cummingtonite in the actinolite–cummingtonite and actinolite–orthopyroxene zones. Fluid infiltration into the reaction zones caused K_2O, CaO, and Al_2O_3 removal (Fig. 16 b), and the zoisite–muscovite symplectites reacted with surrounding hornblende to form tchermakite–spinel symplectite (Fig. 9 f). Stilpnomelane and brucite–serpentine in the actinolite–cummingtonite zone formed after hydration of the host rock. The estimated temperature of 450°C corresponds to the last hydration events. In the last stage, at the lowest *P–T* conditions, the reaction zones in opx–hbl schist formed.

Cross-cutting relationships among reaction zones with different hydration widths (Fig. 5 a) suggest episodic pulses of fluid flow with various durations of fluid infiltration. These pulses occurred repeatedly during hydration of the mafic granulite and opx–hbl schist (620°C and 0.5 GPa to 450°C and 0.3 GPa). The rise in fluid pressure triggered fracturing, and the fluid flowed into the main fracture and infiltrated the wall rock mainly along grain boundaries. The fluid infiltration in the wall rock was coupled to the dissolution–precipitation replacement of apatite. The timescales of fluid

infiltration into the wall rock are constrained to be 1–14 h, representing short pulses of fluid infiltration (Fig. 30). The permeability of the wall rock (reaction zones ± host rock) was as low as 10^{-24}–10^{-20} m^2 in both the mafic granulite, opx–hbl schist and opx–hbl gneiss (Table 6). The permeability of a single fracture (10^{-9}–10^{-8} m^2) is more than ten orders of magnitude higher than that of the wall rock, and the spatially averaged crustal permeability may have been enhanced by several orders of magnitude (10^{-16} to 10^{-10} m^2) as compared with the intact crust (10^{-24} to 10^{-20} m^2). These single fractures acted as effective pathways for fluid flow over durations of tens of hours.

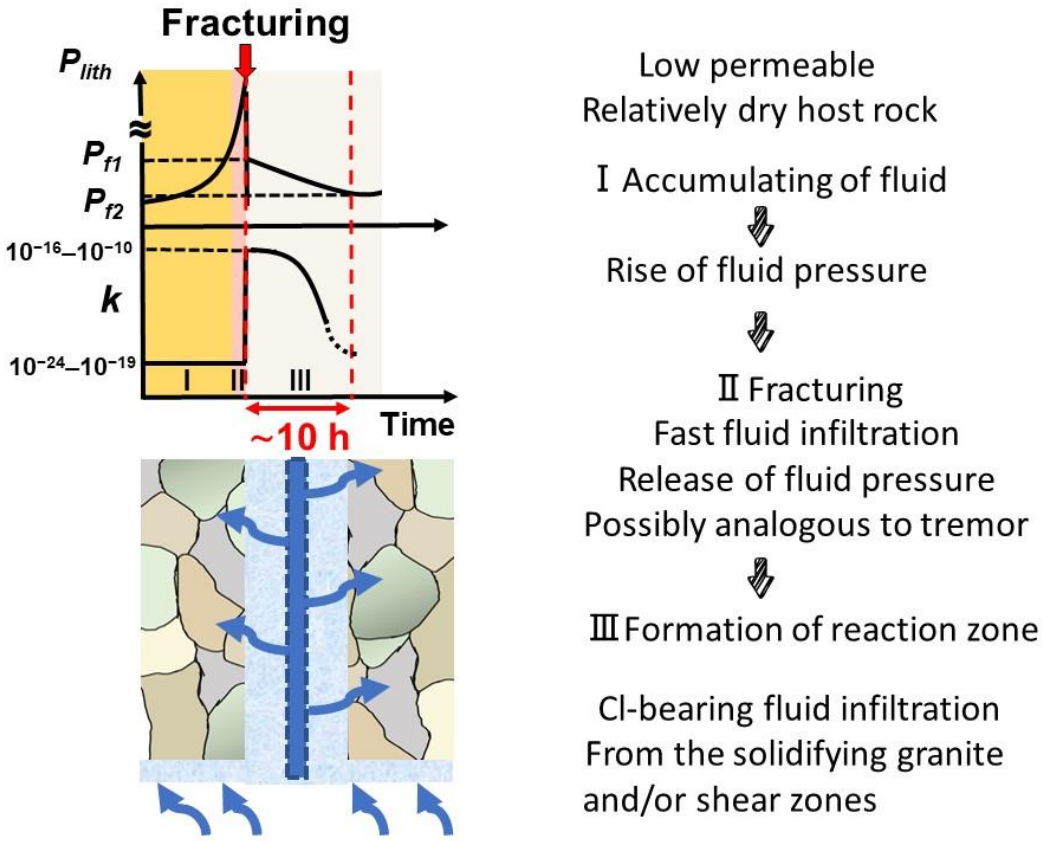

Fig. 30 Rapid fluid infiltration model in low-permeability metamorphic rocks triggered by crustal fracturing. Stage I is the pre-fracturing stage. Fluid pressure increases under lithostatic conditions with time, and permeability is constant in this stage. Stage II is the fracturing stage caused by an increase in fluid pressure. At the timing of fracturing, fluid pressure suddenly drops, and the permeability increases. Stage III is the post-fracturing stage and the host rock continues to react until all the fluids are removed. Permeability decreases due to fracture sealing.

5.4. Rapid fluid infiltration in the middle–lower crust

My results provide the first geological evidence of episodic fluid flow in the crust driven by fluid accumulation in nearly impermeable host rocks. The extremely short timescales of fluid infiltration estimated in this study relate to rapid fluid infiltration related to crustal fracturing. Timescales of fluid infiltration estimated for the mafic granulite and opx–hbl schist are extremely short (1–14 h) as compared with previous studies (e.g., John et al., 2012; Kleine et al., 2016; Taetz et al., 2018). For example, Kleine et al. (2016) described late-stage fluid flow along fractures in greenschist-facies quartz–mica schists from Delfini, northwest Syros, with timescales estimated to be 100–15000 yr, possibly associated with short and fast fluid pulses. Eclogite veins in blueschists from the Tianshan have estimated fluid flow timescales of ca. 200 yr, which are suggested to relate to fluids released by dehydration in a series of short pulses from the subducting slab (John et al., 2012). A fluid flow duration of 1–4 months has been estimated for garnet–quartz–phengite veins within eclogite-facies rocks, and linked to pulses of high pore-fluid pressure and slip events (Taetz et al., 2018). Compared with these studies, my fluid flow timescales are very short.

At a confining pressure of 0.3–0.6 GPa, fluid pressure at the onset of fracturing should have reached near lithostatic levels in order to cause fracturing (e.g., Fyfe, 1978; Manning and Ingebritsen, 1999; Cox, 2010). The permeability of the host rock estimated in this study is extremely low (10^{-24}–10^{-20} m^2) as compared with the permeability of the middle–lower crust (10^{-18} m^2; Hanson, 1995; Ingebritsen and Manning, 2010; Williams and Narasimhan, 1989). Such low-permeability host rocks can accumulate fluids and reach high fluid pressures (e.g., Katayama et al., 2012). The permeability of the fractured crust is much higher (10^{-16} to 10^{-10} m^2), which allows significant amounts of fluid to be transported along the fractures as compared with the host rocks. The short timescales (1–14 h) and high fluid pressures provide evidence of rapid fluid infiltration associated with fracturing, possibly related to high-fluid-pressure fracturing events (Fig. 30) such as earthquake clusters and slow-slip earthquakes (Fig. 30), (Hacker et al., 2003; Katayama et al., 2012). Although earthquakes are common at subduction zone boundaries and active volcanoes (Becken et al., 2011; Gao and Wang, 2017), non-volcanic earthquakes have also been detected in the crust at 30 km depths in southwest Japan (Obara, 2002). The duration of each earthquake is generally a few

minutes to a few days (Chouet, 1996; Obara, 2002). The triggering mechanism for such tremors is considered to be fluid over-pressure caused by fluid infiltration (Cruz-Atienza et al., 2018; Obara, 2002) and associated upward migration of fluids into the overlying crust (Nakajima and Uchida, 2018).

The mafic granulite and opx–hbl schist are surrounded by granite and diorite (Fig. 2). The sampling location is also close (~2 km) to the Sør Rondane Suture (Osanai et al., 2013, 1992; Fig. 2), which is a shear zone in the SW terrane. In the SRM, Cl-bearing fluid infiltration is located close to tectonic boundaries and/or shear zones (Higashino et al., 2013, 2019a; Kawakami et al., 2017). Release of Cl-bearing fluids is also related to granitic dyke intrusion (Uno et al., 2017). This suggests that the Cl-bearing fluids might have migrated from the nearby solidifying granite and/or shear zones into the mafic granulite and opx–hbl schist via fractures, which may have formed as a result of a short seismic event. Shear fractures (Fig. 5) infilled with minerals were also observed in outcrops (Fig. 5). The low-permeability nature of the host rock enabled the accumulation of fluid and increase in pressure, which subsequently caused fracturing and a rapid fluid flow event (Fig. 30).

5.6 Permeability fluctuations in the middle–lower crust

Compared with the previously estimated "normal" permeability of the middle–lower crust (10^{-18} m^2; Hanson, 1995; Ingebritsen and Manning, 2010; Williams and Narasimhan, 1989), the permeability of the host rocks (10^{-24} to 10^{-20} m^2) is two to four orders of magnitude lower. Middle–lower crustal permeability data were obtained by analysis of metamorphic rocks (e.g., Ingebritsen and Manning, 2002, 2010; Manning and Ingebritsen, 1999). For example, the "geothermal–metamorphic" dataset is based on regional and contact metamorphic rocks from the middle–lower crust. Higher values have been proposed for fault zone metamorphism and metamorphism with pulses of thermal heating (i.e., the "high permeability" dataset; Ingebritsen and Manning, 2010). These permeabilities are based on the time-integrated fluid flux estimated for metamorphic rock samples. The time-integrated fluid flux is related to changes in chemical composition along an assumed flow path due to alteration reactions. To estimate the permeability, the time-integrated fluid flux is divided by the duration of fluid infiltration and the pressure gradient. These average long-term (>1 Myr) fluid fluxes are likely to have been influenced by multiple infiltration events. The fluid pressure gradient is also assumed to be the difference between the lithostatic and hydrostatic pressures, which is representative of spatially and temporally averaged fluid flow during metamorphism (Manning and Ingebritsen, 1999). Therefore, these data mostly represent an average of accumulated fluid flow events that are representative of long-term permeability (i.e., >1 Myr). In this study, I consider that the low permeability of the host rock contributed to the increase in fluid pressure and enabled subsequent fracturing and episodic rapid fluid flux, representing "instantaneous" permeability for a dynamic short-lived fluid infiltration event (Figs. 30, 31).

In fact, permeabilities as low as 10^{-24} to 10^{-20} m^2 have also been reported from experimental measurements of crustal rocks under crustal *P–T* conditions (Katayama et al., 2012; Shmonov et al., 2003). Such a low permeability for the middle–lower crust has also been proposed based on the decrease of permeability with increasing deformation (Zhang et al., 1994a, b). The calculated permeability of the fractured crust is consistent with those estimated from migration of hypocentres in crustal earthquake clusters (i.e., 10^{-13}–10^{-15} m^2; Nakajima and Uchida, 2018; Okada et al., 2015). It is possible that Myr-scale averaged permeability may represent a spatial and temporal

average of background permeability associated with short-term, episodic pulses of fluid flow that occurs on typical earthquake recurrence timescales (10–10000 yr). My estimated fluid flow timescales are comparable to geophysical observations (e.g., Nakajima and Uchida, 2018). As such, it is clear that fluid flow timescales and permeabilities in the middle–lower crust can be highly variable.

Accumulation of fluids in the low-permeability rocks leads to an increase in fluid pressure to near lithostatic conditions (i.e., the pre-fracturing stage) and this subsequently causes fracturing (i.e., the fracturing stage). The fluid flux may have been limited resulting in a short duration of fluid infiltration. After fracturing, the permeability increases, and the fluid pressure drops. Fluid infiltration from fluid-conducting fractures into wall rocks promotes mass transport, and may cause the permeability to decrease due to sealing by mineral reactions and deformation (Fig. 30). Previous estimates of the permeability in the middle–lower crust fall within the range of the host rock and fracture permeabilities (Fig. 31). This indicates that even in deep crustal conditions, fracture permeability can be relatively high when associated with crustal hydrofracturing.

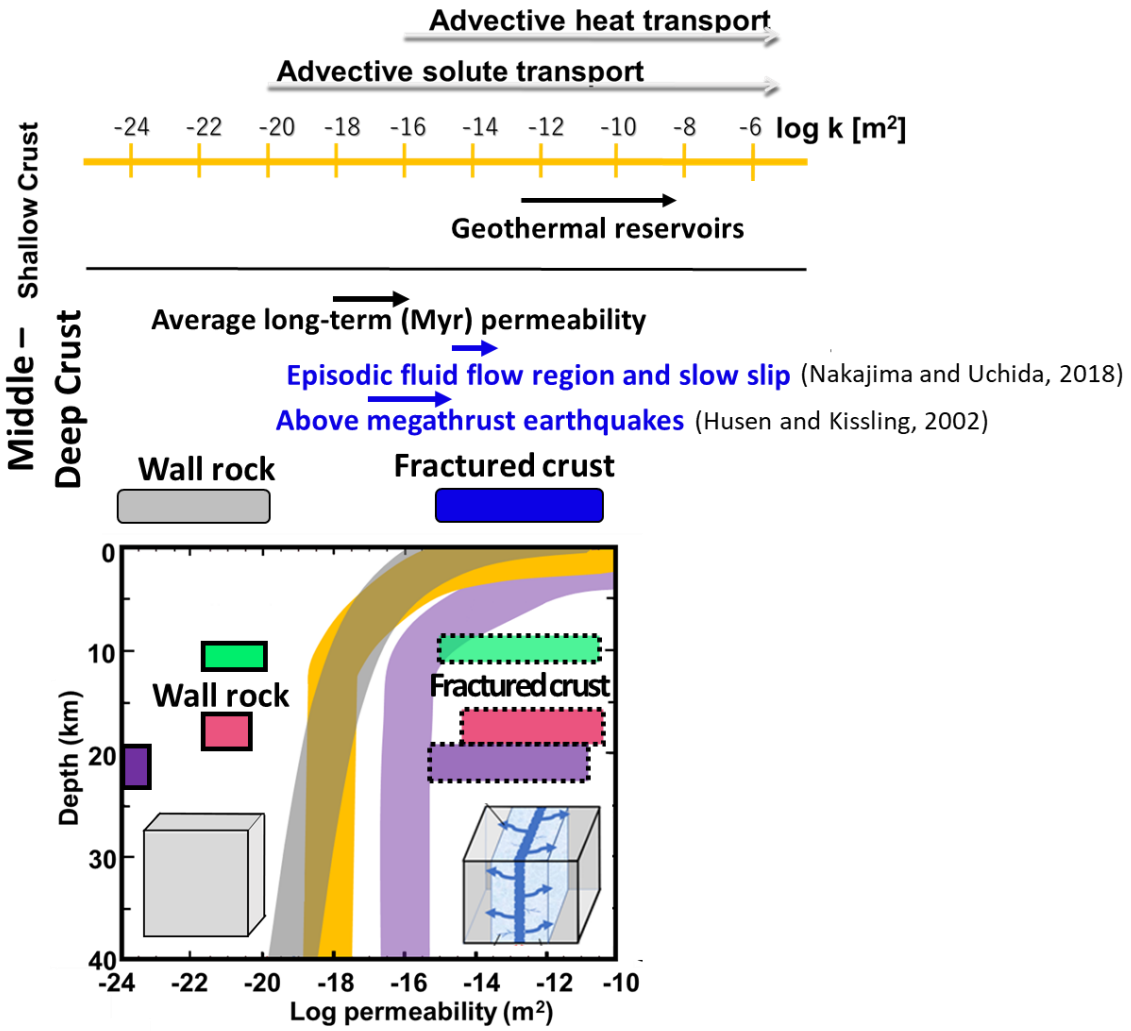

Fig. 31 Permeability evolution in the crust estimated for the wall rocks and fractured crust in comparison with values of geological processes. A comparison between the estimated permeabilities of the host rock and spatio-averaged “fractured crust” in the mafic granulite (pink), opx–hbl schist (green) and opx–hbl gneiss (purple). Curves showing permeability variations with depth are from Manning and Ingebritsen (1999), Ingebritsen and Manning (2002), and Ingebritsen and Manning (2010).

5.7 Conclusion

In this chapter I described formation mechanism of the hydration reaction zones, spatiotemporal evolution of studied areas, and provide overview of fluid fluxes in the crust, and finally suggest permeability fluctuation model in the middle-lower crust. Obtained timescales (i.e., tens of hours) corresponds to the duration of fluid activity on the scale of a grain boundary. Timescales estimated in this study not necessarily the same as the timescale of brittle fracturing. Based on the relationships between reaction zone formation, Cl transport, and estimated timescales I suggest that reaction zones were formed mostly simultaneously with cl-bearing fluid infiltration.

I introduce permeability fluctuation model in the crust, describing evolution from the low-permeable wall rock to the highly permeable fractured crust. Crustal fracturing is triggered by the fluid infiltration and fluid pressure rise. Previous permeability data describe myr-scale averaged permeability which possibly represent average of background permeability associated with episodic pulses of fluid flow. Such pulses may occur on typical earthquake recurrence timescales (10–10000 yr). Timescales estimated in this work is comparable geophysical data (e.g., Nakajima and Uchida, 2018). I estimated numerically permeability fluctuation in the crust and proposed model explaining that even middle-lower crust can transport significant amount of fluids when associated with crustal hydrofracturing and fluid flow timescales and permeabilities in the middle–lower crust can be highly variable.

Chapter 6
Conclusion

6. Conclusions

In this thesis, hydration processes in partially hydrated mafic granulite, opx–hbl schist, and opx–hbl gneiss from the SRM, East Antarctica were investigated. I focused on Cl-bearing fluid infiltration timescales and wall rock and fractures permeabilities estimations. Geophysical observations suggest possibility of fluid transport in the crustal conditions, however numerical parameters as well as mechanism of hydrological properties evolution were unknown. In this thesis I presented unique evidence of rapid fluid infiltration in the crust in low-permeability rocks driven by a high fluid-pressure gradient and hydraulic fracturing. This mechanism could occur periodically in the crust and account for permeability fluctuations over several orders of magnitude during the transition from fracturing to sealing.

In chapter 2, I divided samples into several zones based on microtextural observations, hydrous minerals modes variations, and elemental transport. Reaction zones in each sample fingerprint fluid infiltration characteristics were analysed. *P–T* conditions of fluid infiltration in the SW terrane, SRM estimated for reaction zone formation in the opx–hbl gneiss (0.54 – 0.62 GPa and 720-740 °C) was formed during compression stage followed by fluid infiltration in mafic granulite (~0.55 GPa and ~650°C) correspond to the decompression cooling part of the *P–T* path, whereas the *P–T* conditions for reaction zones in opx–hbl schist (~0.3 GPa and ~450°C) correspond to the latest metamorphic stage. This suggests that these fluid infiltration events occurred after the collision of the East African–Antarctic Orogen and during uplift of the entire collisional zone.

In the chapter 3, I constrained timescales of fluid infiltration and analysed fluid mobile elemental profiles and applied reactive transport model with local equilibrium.

In the chapter 4, I estimated fluid pressure gradient by thermodynamic modeling and calculated wall rock, fractures and spacio-averaged permeabilities of the crust. I also calculated time-integrated fluid fluxes through the reaction zones and through the fracture. Finally, I proposed fluid infiltration model in the crustal conditions in chapter 5. Rapid infiltration of Cl-bearing fluids (1–14 h) into low-permeability (10^{-24} to 10^{-20} m^2) host rocks occurred through crustal fracturing. Low-permeability media led to the accumulation of fluid and promoted fluid-assisted fracturing. Significant amount of fluid flowed through the main facture, and infiltrated the host rock via grain boundaries

± microfractures, which led to apatite–fluid reactions, as well as hydration reactions. The permeability then increased by several orders of magnitude (~10^{-16} to 10^{-10} m^2) and the fluid pressure dropped. The contrast between the host rock and fracture permeability provides information about the permeability evolution from the low-permeability matrix to high-permeability fractured rocks.

References

Adachi, T., Hokada, T., Osanai, Y., Nakano, N., Baba, S., Toyoshima, T., 2013. Contrasting metamorphic records and their implications for tectonic process in the central Sør Rondane Mountains, eastern Dronning Maud Land, East Antarctica. Geol. Soc. London, Spec. Publ. 383, 113 LP – 133. https://doi.org/10.1144/SP383.4

Ague, J.J., 1994. Mass transfer during Barrovian metamorphism of pelites, south-central Connecticut. I: evidence for changes in composition and volume. Am. J. Sci. https://doi.org/10.2475/ajs.294.8.989

Ague, J.J., Baxter, E.F., 2007. Brief thermal pulses during mountain building recorded by Sr diffusion in apatite and multicomponent diffusion in garnet. Earth Planet. Sci. Lett. 261, 500–516. https://doi.org/10.1016/j.epsl.2007.07.017

Ague, J.J., Rudnick, L.R., 2003. Fluid Flow in the Deep Crust, Treatise on Geochemistry.

Anderson G. M., 2005. Thermodynamics of natural systems. Cambridge University Press.

Anderson, J.L., Smith, D.R., 1995. The effects of temperature and fO2 on the Al-in-hornblende barometer. Am. Mineral. 80, 549–559. https://doi.org/10.2138/am-1995-5-614

Aranovich, L.Y., Newton, R.C., 1996. H2O activity in concentrated NaCl solutions at high pressures and temperatures measured by the brucite-periclase equilibrium. Contrib. to Mineral. Petrol. 125, 200–212. https://doi.org/10.1007/s004100050216

Asami, M., Suzuki, K., Grew, E.S., 2005. Monazite and zircon dating by the chemical Th-U-total Pb isochron method (CHIME) from Alasheyev bight to the Sør Rondane Mountains, East Antarctica: A reconnaissance study of the Mozambique suture in eastern Queen Maud land. J. Geol. 113, 59–82. https://doi.org/10.1086/425969

Audet, P., Bürgmann, R., 2014. Possible control of subduction zone slow-earthquake periodicity by silica enrichment. Nature 510, 389–392. https://doi.org/10.1038/nature13391

Baba, S., Osanai, Y., Nakano, N., Owada, M., Hokada, T., Horie, K., Adachi, T., Toyoshima, T., 2012. Counterclockwise P-T path and isobaric cooling of metapelites from Brattnipene, Sør Rondane Mountains, East Antarctica: Implications for a tectonothermal event at the proto-Gondwana margin. Precambrian Res. 234, 210–228. https://doi.org/10.1016/j.precamres.2012.10.002

Baumgartner, L.P., Rumble, D., 1988. Transport of stable isotopes: I: Development of a kinetic continuum theory for stable isotope transport. Contrib. to Mineral. Petrol. 98, 417–430. https://doi.org/10.1007/BF00372362

Bear, J., 1988. Dynamics of fluids in porous media. Dover publications, New York.

Becken, M., Ritter, O., Bedrosian, P.A., Weckmann, U., 2011. Correlation between deep fluids, tremor and creep along the central San Andreas fault. Nature 480, 87–90. https://doi.org/10.1038/nature10609

Bégué, F., Baumgartner, L.P., Bouvier, A.S., Robyr, M., 2019. Reactive fluid infiltration along fractures: Textural observations coupled to in-situ isotopic analyses. Earth Planet. Sci. Lett. 519, 264–273. https://doi.org/10.1016/j.epsl.2019.05.024

Beinlich, A., John, T., Vrijmoed, J.C., Tominaga, M., Magna, T., Podladchikov, Y.Y., 2020. Instantaneous rock transformations in the deep crust driven by reactive fluid flow. Nat. Geosci. 1–5. https://doi.org/10.1038/s41561-020-0554-9

Bickle, M.J., McKenzie, D., 1987. The transport of heat and matter by fluids during metamorphism. Contrib. to Mineral. Petrol. 95, 384–392. https://doi.org/10.1007/BF00371852

Bijeljic, B., Muggeridge, A.H., Blunt, M.J., 2004. Pore-scale modeling of longitudinal dispersion. Water Resour. Res. 40, 1–9. https://doi.org/10.1029/2004WR003567

Bröcker, M., 1990. Blueschist-to-greenschist transition in metabasites from Tinos Island, Cyclades, Greece: Compositional control or fluid infiltration? Lithos 25, 25–39. https://doi.org/10.1016/0024-4937(90)90004-K

Bruce D. Rohrlach and Robert R. Loucks, 2005. Multi-million-year cyclic ramp-up of volatiles in a lower crustal magma reservour trapped below the tampakan copper-gold deposit by mio-pliocene crustal compression in the southern philippines.

Chouet, B.A., 1996. Long-period volcano seismicity: its source and use in eruption forecasting. Nature 380, 309–316. https://doi.org/10.1038/380309a0

Connolly, J.A.D., 2009. The geodynamic equation of state: What and how. Geochemistry, Geophys. Geosystems 10. https://doi.org/10.1029/2009GC002540

Cox, F., 1995. Faulting processes at high fluid pressures: An example of fault valve behavior from the Wattle Gully Fault, Victoria, Australia. J. Geophys. Res. 100, 23–32.

Cox, S.F., 2016. Injection-driven swarm seismicity and permeability enhancement: Implications for the dynamics of hydrothermal ore systems in high fluid-flux, overpressured faulting regimes - An invited paper. Econ. Geol. 111, 559–587. https://doi.org/10.2113/econgeo.111.3.559

Cox, S.F., 2010. The application of failure mode diagrams for exploring the roles of fluid pressure and stress states in controlling styles of fracture-controlled permeability enhancement in faults and shear zones. Geofluids 10, 217–233. https://doi.org/10.1111/j.1468-8123.2010.00281.x

Cruz-Atienza, V.M., Villafuerte, C., Bhat, H.S., 2018. Rapid tremor migration and pore-pressure waves in subduction zones. Nat. Commun. 9. https://doi.org/10.1038/s41467-018-05150-3

Dipple, G.M., Ferry, J.M., 1992. Metasomatism and fluid flow in ductile fault zones. Contrib. to Mineral. Petrol. 112, 149–164. https://doi.org/10.1007/BF00310451

Doherty, A.L., Webster, J.D., Goldoff, B.A., Piccoli, P.M., 2014. Partitioning behavior of chlorine and fluorine in felsic melt-fluid(s)-apatite systems at 50MPa and 850-950 °C. Chem. Geol. 384, 94–109. https://doi.org/10.1016/j.chemgeo.2014.06.023

Fournier, R.O., 1991. THE TRANSITION FROM HYDROSTATIC TO GREATER THAN HYDROSTATIC FLUID PRESSURE IN PRESENTLY AC'T/VE CONTINENTAL HYDROTttERMAL SYSTEMS IN CRYSTAI•INE ROCK. Geophys. Res. Lett. 18, 955–958.

Fuhrman, M.L., Lindsley, D.H., 1988. Ternary-feldspar modeling and thermometry. Am. Mineral. 73, 201–215.

Fukuyama, M., Nishiyama, T., Urata, K., Mori, Y., 2006. Steady-diffusion modelling of a reaction zone between a metamorphosed basic dyke and a marble from Hirao-dai, Fukuoka, Japan. J. Metamorph. Geol. 24, 153–168. https://doi.org/10.1111/j.1525-1314.2006.00631.x

Fyfe, W.S., 1978. The evolution of the earth's crust: Modern plate tectonics to ancient hot spot tectonics? Chem. Geol. 23, 89–114. https://doi.org/10.1016/0009-2541(78)90068-2
Gao, X., Wang, K., 2017. Rheological separation of the megathrust seismogenic zone and episodic tremor and slip. Nature 543, 416–419. https://doi.org/10.1038/nature21389
Gerdemann, S.J., O'Connor, W.K., Dahlin, D.C., Penner, L.R., Rush, H., 2007. Ex situ aqueous mineral carbonation. Environ. Sci. Technol. 41, 2587–2593. https://doi.org/10.1021/es0619253
Goldfarb, R.J., Newberry, R.J., Pickthorn, W.J., Gent, C.A., 1991. Oxygen, hydrogen, and sulfur isotope studies in the Juneau gold belt, southeastern Alaska; constraints on the origin of hydrothermal fluids. Econ. Geol. 86, 66–80. https://doi.org/10.2113/gsecongeo.86.1.66
Goto, A., Banno, S., 1990. Hydration of basic granulite to garnet-epidote amphibolite in the Sanbagawa metamorphic belt, central Shikoku, Japan. Chem. Geol. 85, 247–263. https://doi.org/10.1016/0009-2541(90)90003-P
Hack, A.C., Thompson, A.B., 2011. Density and viscosity of hydrous magmas and related fluids and their role in subduction zone processes. J. Petrol. 52, 1333–1362. https://doi.org/10.1093/petrology/egq048
Hacker, B.R., Peacock, S.M., Abers, G.A., Holloway, S.D., 2003. Subduction factory 2. Are intermediate-depth earthquakes in subducting slabs linked to metamorphic dehydration reactions? J. Geophys. Res. Solid Earth 108. https://doi.org/10.1029/2001jb001129
Hanson, R.B., 1995. The hydrodynamics of contact metamorphism. Geol. Soc. Am. Bull. 107, 595–611. https://doi.org/10.1130/0016-7606(1995)107<0595:THOCM>2.3.CO
Hara, J., Tsuchiya, N., 2005. An experimental and modeling study of Na-rich hydrothermal alteration. Geofluids 5, 251–263. https://doi.org/10.1111/j.1468-8123.2005.00115.x
Higashino, F., Kawakami, T., Satish-Kumar, M., Ishikawa, M., Maki, K., Tsuchiya, N., Grantham, G.H., Hirata, T., 2013. Chlorine-rich fluid or melt activity during granulite facies metamorphism in the Late Proterozoic to Cambrian continental collision zone-An example from the Sør Rondane Mountains, East Antarctica. Precambrian Res. 234, 229–246. https://doi.org/10.1016/j.precamres.2012.10.006
Higashino, F., Kawakami, T., Tsuchiya, N., Satish-Kumar, M., Ishikawa, M., Grantham, G., Sakata, S., Hirata, T., 2019a. Brine Infiltration in the Middle to Lower Crust in a Collision Zone: Mass Transfer and Microtexture Development Through Wet Grain-Boundary Diffusion. J. Petrol. 60, 329–358. https://doi.org/10.1093/petrology/egy116
Higashino, F., Kawakami, T., Tsuchiya, N., Satish-Kumar, M., Ishikawa, M., Grantham, G.H., Sakata, S., Hattori, K., Hirata, T., 2015. Geochemical behavior of zirconium during Cl-rich fluid or melt infiltration under upper amphibolite facies metamorphism - A case study from Brattnipene, Sør Rondane Mountains, East Antarctica. J. Mineral. Petrol. Sci. 110, 166–178. https://doi.org/10.2465/jmps.150220
Higashino, F., Rubatto, D., Kawakami, T., Bouvier, A.S., Baumgartner, L.P., 2019b. Oxygen isotope speedometry in granulite facies garnet recording fluid/melt–rock

interaction (Sør Rondane Mountains, East Antarctica). J. Metamorph. Geol. 1037–1048. https://doi.org/10.1111/jmg.12490
Holland, T., Blundy, J., 1994. Non-ideal interactions in calcic amphiboles and their bearing on amphibole-plagioclase thermometry. Contrib. to Mineral. Petrol. 116, 433–447. https://doi.org/10.1007/BF00310910
Holland, T., Powell, R., 1996. Thermodynamics of order-disorder in minerals: I. Symmetric formalism applied to minerals of fixed composition. Am. Mineral. 81, 1413–1424. https://doi.org/10.2138/am-1996-11-1214
Holland, T.J.B., Powell, R., 1998. An internally consistent thermodynamic data set for phases of petrological interest. J. Metamorph. Geol. 16, 309–343. https://doi.org/10.1111/j.1525-1314.1998.00140.x
Huber, M.L., Perkins, R.A., Laesecke, A., Friend, D.G., 2009. New international formulation for the viscosity of H 2 O. J. Phys. Chem. Ref. Data. 38.2, 101–125. https://doi.org/10.1163/_q3_SIM_00374
Ingebritsen, S.E., Manning, C.E., 2010. Permeability of the Continental Crust: Dynamic Variations Inferred from Seismicity and Metamorphism. Front. Geofluids 193–205. https://doi.org/10.1002/9781444394900.ch13
Ingebritsen, S.E., Manning, C.E., 2002. Diffuse fluid flux through orogenic belts: Implications for the world ocean. Proc. Natl. Acad. Sci. U. S. A. 99, 9113–9116. https://doi.org/10.1073/pnas.132275699
Jacobs, J., Bauer, W., Fanning, C.M., 2003. Late Neoproterozoic/Early Palaeozoic events in central Dronning Maud Land and significance for the southern extension of the East African Orogen into East Antarctica. Precambrian Res. https://doi.org/10.1016/S0301-9268(03)00125-6
Jamtveit, B., Bucher-Nurminen, K., Austrheim, H., 1990. Fluid controlled eclogitization of granulites in deep crustal shear zones, Bergen arcs, Western Norway. Contrib. to Mineral. Petrol. 104, 184–193. https://doi.org/10.1007/BF00306442
John, T., Gussone, N., Podladchikov, Y.Y., Bebout, G.E., Dohmen, R., Halama, R., Klemd, R., Magna, T., Seitz, H.M., 2012a. Volcanic arcs fed by rapid pulsed fluid flow through subducting slabs. Nat. Geosci. 5, 489–492. https://doi.org/10.1038/ngeo1482
John, T., Gussone, N., Podladchikov, Y.Y., Bebout, G.E., Dohmen, R., Halama, R., Klemd, R., Magna, T., Seitz, H.M., 2012b. Volcanic arcs fed by rapid pulsed fluid flow through subducting slabs. Nat. Geosci. 5, 489–492. https://doi.org/10.1038/ngeo1482
Jonas, L., John, T., King, H.E., Geisler, T., Putnis, A., 2014. The role of grain boundaries and transient porosity in rocks as fluid pathways for reaction front propagation. Earth Planet. Sci. Lett. 386, 64–74. https://doi.org/10.1016/j.epsl.2013.10.050
Katayama, I., Terada, T., Okazaki, K., Tanikawa, W., 2012. Episodic tremor and slow slip potentially linked to permeability contrasts at the Moho. Nat. Geosci. 5, 731–734. https://doi.org/10.1038/ngeo1559
Kawakami, T., Higashino, F., Skrzypek, E., Satish-Kumar, M., Grantham, G., Tsuchiya, N., Ishikawa, M., Sakata, S., Hirata, T., 2017. Prograde infiltration of Cl-rich fluid into the granulitic continental crust from a collision zone in East Antarctica (Perlebandet, Sør Rondane Mountains). Lithos 274–275, 73–92. https://doi.org/10.1016/j.lithos.2016.12.028

Kleine, B.I., Zhao, Z., Skelton, A.D.L., 2016. Rapid fluid flow along fractures at greenschist facies conditions on Syros, Greece. Am. J. Sci. 316, 169–201. https://doi.org/10.2475/02.2016.03
Kuleci, H., Schmidt, C., Rybacki, E., Petrishcheva, E., Abart, R., 2016. Hydration of periclase at 350 ◦ C to 620 ◦ C and 200 MPa: experimental calibration of reaction rate. Mineral. Petrol. 110, 1–10. https://doi.org/10.1007/s00710-015-0414-2
Kusebauch, C., John, T., Whitehouse, M.J., Klemme, S., Putnis, A., 2015. Distribution of halogens between fluid and apatite during fluid-mediated replacement processes. Geochim. Cosmochim. Acta. https://doi.org/10.1016/j.gca.2015.08.023
Lanari, P., Vidal, O., De Andrade, V., Dubacq, B., Lewin, E., Grosch, E.G., Schwartz, S., 2014. XMapTools: A MATLAB©-based program for electron microprobe X-ray image processing and geothermobarometry. Comput. Geosci. 62, 227–240. https://doi.org/10.1016/j.cageo.2013.08.010
Lasaga A. C., 1998. Kinetics in the earth sciences. Princeton Series in geochemistry.
Li, Z., Tainosho, Y., Kimura, J., Shiraishi, K., 2005. Characterization of the Mefjell plutonic complex from the Sør Rondane Mountains , East Antarctica : Implications for the petrogenesis of Pan-African plutonic rocks of East Gondwanaland. Isl. Arc 14, 636–652.
Lichtner, P.C., Oelkers, E.H., Helgeson, H.C., 1986. Interdiffusion with multiple precipitation/dissolution reactions: Transient model and the steady-state limit. Geochim. Cosmochim. Acta 50, 1951–1966. https://doi.org/10.1016/0016-7037(86)90251-6
Lindsley, D.H., 1983. Pyroxene thermometry. Am. Mineral. 68, 477–493.
Manning, C.E., Ingebritsen, S.E., 1999. PERMEABILITY OF THE CONTINENTAL Crust : IMPLICATIONS OF GEOTHERMAL DATA CRUST ' AND METAMORPHIC SYSTEMS. Rev. Geophys. 127–150.
Márton, I., Moritz, R., Spikings, R., 2010. Application of low-temperature thermochronology to hydrothermal ore deposits: Formation, preservation and exhumation of epithermal gold systems from the Eastern Rhodopes, Bulgaria. Tectonophysics 483, 240–254. https://doi.org/10.1016/j.tecto.2009.10.020
Moré, J.J., Sorensen, D.C., 1983. Computing a Trust Region Step. SIAM J. Sci. Stat. Comput. https://doi.org/10.1137/0904038
Nakajima, J., Uchida, N., 2018. Repeated drainage from megathrusts during episodic slow slip. Nat. Geosci. 11, 351–356. https://doi.org/10.1038/s41561-018-0090-z
Nakatani, T., Nakamura, M., 2016. Experimental constraints on the serpentinization rate of fore-arc peridotites: Implications for the upwelling condition of the slab-derived fluid. Geochemistry Geophys. Geosystems 17, 1312–1338. https://doi.org/10.1002/2015GC006205.Received
Neuman, S.P., 1995. On Advective Transport in Fractal Permeability and velocity Fields. Water Resour. Res. 31, 1455–1460. https://doi.org/10.1029/95WR00426
Obara, K., 2002. Nonvolcanic deep tremor associated with subduction in southwest Japan. Science (80-.). 296, 1679–1681. https://doi.org/10.1126/science.1070378
Obara, K., Hirose, H., 2006. Non-volcanic deep low-frequency tremors accompanying slow slips in the southwest Japan subduction zone. Tectonophysics 417, 33–51. https://doi.org/10.1016/j.tecto.2005.04.013
Oelkers, E.H., Helgeson, H.C., 1988. Calculation of the thermodynamic and transport

properties of aqueous species at high pressures and temperatures: Aqueous tracer diffusion coefficients of ions to 1000°C and 5 kb. Geochim. Cosmochim. Acta 52, 63–85. https://doi.org/10.1016/0016-7037(88)90057-9

Ohmi, S., Obara, K., 2002. Deep low-frequency earthquakes beneath the focal region of the Mw 6.7 2000 Western Tottori earthquake. Geophys. Res. Lett. 29, 54-1-54–4. https://doi.org/10.1029/2001gl014469

Okada, T., Matsuzawa, T., Umino, N., Yoshida, K., Hasegawa, A., Takahashi, H., Yamada, T., Kosuga, M., Takeda, T., Kato, A., Igarashi, T., Obara, K., Sakai, S., Saiga, A., Iidaka, T., Iwasaki, T., Hirata, N., Tsumura, N., Yamanaka, Y., Terakawa, T., Nakamichi, H., Okuda, T., Horikawa, S., Katao, H., Miura, T., Kubo, A., Matsushima, T., Goto, K., Miyamachi, H., 2015. Hypocenter migration and crustal seismic velocity distribution observed for the inland earthquake swarms induced by the 2011 Tohoku-Oki earthquake in NE Japan: Implications for crustal fluid distribution and crustal permeability. Geofluids 307–323. https://doi.org/10.1002/9781119166573.ch24

Osanai, Y., Nogi, Y., Baba, S., Nakano, N., Adachi, T., Hokada, T., Toyoshima, T., Owada, M., Satish-Kumar, M., Kamei, A., Kitano, I., 2013. Geologic evolution of the Sør Rondane Mountains, East Antarctica: Collision tectonics proposed based on metamorphic processes and magnetic anomalies. Precambrian Res. 234, 8–29. https://doi.org/10.1016/j.precamres.2013.05.017

Osanai, Y., Shiraishi, K, Takahashi, Y., Ishizuka, H., Tainosho, Y., Tsuchiya, N., Sakiyama, T., Kodama, S., 1992. Geochemical characteristics of metamorphic rocks from Sør Rondane Mountains, East Antarctica.

Oyanagi, R., Okamoto, A., Tsuchiya, N., 2020. Silica controls on hydration kinetics during serpentinization of olivine: Insights from hydrothermal experiments and a reactive transport model. Geochim. Cosmochim. Acta 270, 21–42. https://doi.org/10.1016/j.gca.2019.11.017

Passarella, M., Mountain, B.W., Seward, T.M., 2017. Experimental Simulations of Basalt-fluid Interaction at Supercritical Hydrothermal Condition (400°C – 500bar). Procedia Earth Planet. Sci. 17, 770–773. https://doi.org/10.1016/j.proeps.2017.01.022

Pedrosa, E.T., Putnis, C. V., Putnis, A., 2016. The pseudomorphic replacement of marble by apatite: The role of fluid composition. Chem. Geol. 425, 1–11. https://doi.org/10.1016/j.chemgeo.2016.01.022

Philpotts, A., Ague, J., 2009. Principles of igneous and metamorphic petrology. Cambridge University Press.

Piccoli, P.M., Candela, P.A., 1994. Apatite in felsic rocks: a model for the estimation of initial halogen concentrations in the Bishop tuff (Long valley) and tuolumne intrusive suite (Sierra Nevada batholith) magmas. Am. J. Sci. 294, 92–135.

Pollington, A.D., Baxter, E.F., 2010. High resolution Sm-Nd garnet geochronology reveals the uneven pace of tectonometamorphic processes. Earth Planet. Sci. Lett. 293, 63–71. https://doi.org/10.1016/j.epsl.2010.02.019

Powell, R., Holland, T., 1999. Relating formulations of the thermodynamics of mineral solid solutions: Activity modeling of pyroxenes, amphiboles, and micas. Am. Mineral. 84, 1–14. https://doi.org/10.2138/am-1999-1-201

Reynard, B., 2016. Mantle hydration and Cl-rich fluids in the subduction forearc. Prog. Earth Planet. Sci. 3. https://doi.org/10.1186/s40645-016-0090-9

Reynard, B., Mibe, K., de Moortèle, B. Van, 2011. Electrical conductivity of the serpentinised mantle and fluid flow in subduction zones. Earth Planet. Sci. Lett. 307, 387–394. https://doi.org/10.1016/j.epsl.2011.05.013

Rohrlach, B.D., Loucks, R.R., 2005. Multi-Million-Year Cyclic Ramp-Up of Volatiles in a Lower Crustal Magma Reservoir Trapped Below the Tampakan Copper-Gold Deposit By Mio-Pliocene. Super Porphyry Copp. Gold Depos. A Glob. Perspect. V.2 2, 369–407.

Saar, M.O., Manga, M., 2004. Depth dependence of permeability in the Oregon Cascades inferred from hydrogeologic, thermal, seismic, and magmatic modeling constraints. J. Geophys. Res. Solid Earth 109. https://doi.org/10.1029/2003JB002855

Saishu, H., Okamoto, A., Otsubo, M., 2017. Silica precipitation potentially controls earthquake recurrence in seismogenic zones. Sci. Rep. 7, 1–10. https://doi.org/10.1038/s41598-017-13597-5

Saito, S., Ishikawa, M., Arima, M., Tatsumi, Y., 2016. Laboratory measurements of Vp and Vs in a porosity-developed crustal rock: Experimental investigation into the effects of porosity at deep crustal pressures. Tectonophysics 677–678, 218–226. https://doi.org/10.1016/j.tecto.2016.03.044

Schliestedt, M., Matthews, A., 1987. Transformation of blueschist to greenschist facies rocks as a consequence of fluid infiltration, Sifnos (Cyclades), Greece. Contrib. to Mineral. Petrol. 97, 237–250. https://doi.org/10.1007/BF00371243

Shelly, D.R., Beroza, G.C., Ide, S., Nakamula, S., 2006. Low-frequency earthquakes in Shikoku, Japan, and their relationship to episodic tremor and slip. Nature 442, 188–191. https://doi.org/10.1038/nature04931

Shiraishi, K., Dunkley, D.J., Hokada, T., Fanning, C.M., Kagami, H., Hamamoto, T., 2008. Geochronological constraints on the Late Proterozoic to Cambrian crustal evolution of eastern Dronning Maud Land, East Antarctica: a synthesis of SHRIMP U-Pb age and Nd model age data. Geol. Soc. London, Spec. Publ. 308, 21 LP – 67. https://doi.org/10.1144/SP308.2

Shmonov, V.M., Vitiovtova, V.M., Zharikov, A. V., Grafchikov, A.A., 2003. Permeability of the continental crust: Implications of experimental data. J. Geochemical Explor. 78–79, 697–699. https://doi.org/10.1016/S0375-6742(03)00129-8

Sibson, R.H., 1994. Crustal stress, faulting and fluid flow. Geol. Soc. London, Spec. Publ. 78, 69 LP – 84. https://doi.org/10.1144/GSL.SP.1994.078.01.07

Taetz, S., John, T., Bröcker, M., Spandler, C., Stracke, A., 2018. Fast intraslab fluid-flow events linked to pulses of high pore fluid pressure at the subducted plate interface. Earth Planet. Sci. Lett. 482, 33–43. https://doi.org/10.1016/j.epsl.2017.10.044

TSUBOKAWA, Y., ISHIKAWA, M., KAWAKAMI, T., HOKADA, T., SATISH–KUMAR, M., TSUCHIYA, N., GRANTHAM, G.H., 2017. Pressure–temperature–time path of a metapelite from Mefjell, Sør Rondane Mountains, East Antarctica. J. Mineral. Petrol. Sci. 112, 77–87. https://doi.org/10.2465/jmps.160919

Ujiie, K., Saishu, H., Fagereng, Å., Nishiyama, N., Otsubo, M., Masuyama, H., Kagi, H., 2018. An Explanation of Episodic Tremor and Slow Slip Constrained by Crack-Seal Veins and Viscous Shear in Subduction Mélange. Geophys. Res. Lett. 45, 5371–5379. https://doi.org/10.1029/2018GL078374

Uno, M., Okamoto, A., Tsuchiya, N., 2017. Excess water generation during reaction-inducing intrusion of granitic melts into ultramafic rocks at crustal P–T conditions in the Sør Rondane Mountains of East Antarctica, Lithos. Elsevier B.V. https://doi.org/10.1016/j.lithos.2017.04.016

Warren-Smith, E., Fry, B., Wallace, L., Chon, E., Henrys, S., Sheehan, A., Mochizuki, K., Schwartz, S., Webb, S., Lebedev, S., 2019. Episodic stress and fluid pressure cycling in subducting oceanic crust during slow slip. Nat. Geosci. 12, 475–481. https://doi.org/10.1038/s41561-019-0367-x

Watanabe, N., Hirano, N., Tsuchiya, N., 2008. Determination of aperture structure and fluid flow in a rock fracture by high-resolution numerical modeling on the basis of a flow-through experiment under confining pressure. Water Resour. Res. 44, 1–11. https://doi.org/10.1029/2006WR005411

Webster, J.D., Goldoff, B.A., Flesch, R.N., Nadeau, P.A., Silbert, Z.W., 2017. Hydroxyl, Cl, and F partitioning between high-silica rhyolitic melts-apatite-fluid(s) at 50-200 MPa and 700-1000 °c. Am. Mineral. 102, 61–74. https://doi.org/10.2138/am-2017-5746

Webster, J.D., Tappen, C.M., Mandeville, C.W., 2009. Partitioning behavior of chlorine and fluorine in the system apatite-melt-fluid. II: Felsic silicate systems at 200 MPa. Geochim. Cosmochim. Acta 73, 559–581. https://doi.org/10.1016/j.gca.2008.10.034

Wei, C., Powell, R., 2003. Phase relations in high-pressure metapelites in the system KFMASH. Contrib. to Mineral. Petrol. 145, 301–315. https://doi.org/10.1007/s00410-003-0454-1

Whitney, D.L., Evans, B.W., 2010. Abbreviations for names of rock-forming minerals. Am. Mineral. 95, 185–187. https://doi.org/10.2138/am.2010.3371

Williams, C.F., Narasimhan, T.N., 1989. Hydrogeologic constraints on heat flow along the San Andreas fault: a testing of hypotheses. Earth Planet. Sci. Lett. 92, 131–143. https://doi.org/10.1016/0012-821X(89)90041-1

Yardley, B.W.D., Rhede, D., Heinrich, W., 2014. Rates of retrograde metamorphism and their implications for the rheology of the crust: An Experimental Study. J. Petrol. 55, 623–641. https://doi.org/10.1093/petrology/egu001

Zhang, S, Cox, S.F., Paterson, M.S., 1994. The influence of room temperature deformation on porosity and permeability in calcite aggregates. J. Geophys. Res. 99. https://doi.org/10.1029/94jb00647

Zhang, S., Paterson, M.S., Cox, S.F., 1994. Porosity and permeability evolution during hot isostatic pressing of calcite aggregates. J. Geophys. Res. 99, 15,741-15,760.

Acknowledgements

I would like to acknowledge many of the people that I have cooperated with and learned from throughout my PhD. I was very fortunate to have met many excellent scientist and fellow graduate students, and completed my PhD research with the greatest support.

First of all, I would like to acknowledge my supervisor Professor Noriyoshi Tsuchiya without whom I will never have a chance to become a Tohoku University student and conduct research using samples from Antarctica and having a chance to visit most wonderful places on the Earth.

I am deeply indebted to Professor Takeshi Komai and Professor Tatsuki Tsujimori for the valuable discussions, advices, patient, and motivation during past several years. I would like to express my deepest gratitude to Professor Masaoki Uno for the greatest support and his kindness during all 5 years and keep believing even when I could not meet expectations. I would like to acknowledge Professor Atsushi Okamoto. I appreciate scientific discussions and questions making me think deeply and discover more. I also appreciate Yamada R. and Hirano N. for the knowledges and technical skills they shared to me. Thank you for bringing me to the various fields and conferences and teaching about geology and geological approaches in Japan. I could understand what are trends now and what will be important in near future and which problems are important for the science and society. I also grateful to having chance to teach younger students and become friends with them. I realize that there are many talented and excellent students in Tohoku University who are also great people, and I appreciate to have a chance to study from them and become better human, I hope. I wish humanity would never stop their endless way to discover nature and young people will have a will and chance to follow it.

I would like to thank to all members of JARE-51. T. Kawakami, M. Ishikawa, M. Satish-Kumar, G. Grantham for the unique samples from Antarctica. R. Oyanagi, and K. Yoshida are thanked for critical comments on the previous version of the figures and manuscript and strict care. M. Toriumi is thanked for continued support, inspiration, constructive discussions and amount of energy and motivation he shares to others. I also appreciate PhDs students, Amanda Fajar Febiani and Alviani Vani Novita struggling and share this moment together, my labmates for mental and snacks support, my friends

Nguyen Chi Long, Natt Sutthikulkarn and Yoshida K. for keep being inspired about science, my parents for willing to sell everything if I will not graduate and made me terrifying, and all people I could not mentioned but deeply thankful to in my heart.

Publications

Papers

Diana Mindaleva, Masaoki Uno, Fumiko Higashino, Takayoshi Nagaya, Atsushi Okamoto, Noriyoshi Tsuchiya. Rapid fluid infiltration and permeability enhancement during middle–lower crustal fracturing: Evidence from amphibolite–granulite-facies fluid–rock reaction zones, Sør Rondane Mountains, East Antarctica : *Lithos,* 2020, 105521, ISSN 0024-4937, https://doi.org/10.1016/j.lithos.2020.105521.

Mindaleva Diana, Masaoki Uno, Atsushi Okamoto, Noriyoshi Tsuchiya. Crustal permeability revealed by metamorphic processes and rapid infiltration of geofluids. Geothermal volcanology workshop proceedings, 2019, p. 125-128, 550.36

Oral presentations in international conferences

Diana Mindaleva, Masaoki Uno, Atsushi Okamoto, Noriyoshi Tsuchiya "Crustal permeability revealed by metamorphic processes and rapid infiltration of geofluids" Geothermal Volcanology Workshop 2019, Petropavlovsk-Kamchatsky, Institute of Volcanology and Seismology FEB RAS,

Diana Mindaleva, Masaoki Uno, Atsushi Okamoto, Noriyoshi Tsuchiya "Geological evidences of short fluid activity at crustal P-T conditions in the low permeable metamorphic rocks triggered by crustal fracturing"　International Joint Workshop on Slow Earthquakes 2019

Poster presentations in international conferences

Diana Mindaleva, Masaoki Uno, Atsushi Okamoto, Noriyoshi Tsuchiya. Multiply hydration events of pyroxenite and amphibolite in the middle crustal conditions, Sør Rondane Mountains, East Antarctica,　日本地球惑星科学連合(JpGU)2017 年大会 2017

Diana Mindaleva, Masaoki Uno, Fumiko Higashino, Atsushi Okamoto, Noriyoshi Tsuchiya. Short fluid infiltration events in the low permeable metamorphic rocks at amphibolite‐granulite facies conditions linked to crustal fracturing. International

Workshop on Water Dynamics 16th, 2019

Diana MINDALEVA, Masaoki UNO, Atsushi OKAMOTO, Noriyoshi TSUCHIYA . Short fluid infiltration events in the low permeable metamorphic rocks at crustal P-T conditions, International Workshop on Water Dynamics 17th 2020

Oral presentations in domestic conferences

Diana Mindaleva, Masaoki Uno, Atsushi Okamoto, Takayoshi Nagaya, Noriyoshi Tsuchiya. Investigation of Mass Transport and Reactive Mechanism by Cl Bearing Fluid Infiltration during Multiple Hydration Events, Sør Rondane Mountains, East Antarctica, 極域科学シンポジウム(Polar Science Symposium) 第 8 回 2017

Diana Mindaleva, Masaoki Uno, Fumiko Higashino, Takayoshi Nagaya, Ryosuke Oyanagi, Atsushi Okamoto, Noriyoshi Tsuchiya. Time scales of Cl-bearing fluid infiltration and permeability estimated by reactive transport modelling for granulite/amphibolite-hosted reaction zones, Sør Rondane Mountains, East Antarctica. 日本地球惑星科学連合(JpGU)2018 年大会

Diana Mindaleva, Masaoki Uno, Fumiko Higashino, Atsushi Okamoto, Noriyoshi Tsuchiya. 東南極セールロンダーネ山地，グラニュライト・角閃岩相反応帯における多元微量元素解析による含 Cl 流体の浸透の時間スケール 日本鉱物科学会(JAMS)2018 年年会 2018

Diana Mindaleva, Masaoki Uno, Fumiko Higashino, Atsushi Okamoto, Noriyoshi Tsuchiya. Timescales of Cl-bearing fluid infiltration estimated by multiple trace elements profiles in apatite for granulite/amphibolite-hosted reaction zones, Sør Rondane Mountains, East Antarctica. 極域科学シンポジウム(Polar Science Symposium) 第 9 回, 2018

Poster presentations in domestic conferences

Diana Mindaleva, Masaoki Uno, Fumiko Higashino, Atsushi Okamoto, Noriyoshi Tsuchiya. Fluid pressure gradients and permeability estimated from reaction zones water activities at amphibolite‐granulite facies conditions. 変成岩などシンポジウム 蒲郡シンポジウム 2019

Diana Mindaleva, Masaoki Uno, Fumiko Higashino, Atsushi Okamoto, Noriyoshi Tsuchiya. Short fluid infiltration events in the low permeable metamorphic rocks triggered by crustal fracturing at amphibolite‐granulite facies conditions. 日本地球惑星科学連合(JpGU) 2019 年大会 2019

Diana Mindaleva, Masaoki Uno, Atsushi Okamoto, Noriyoshi Tsuchiya. Crustal permeability and timescales estimated from metamorphic fluid-rock reaction zones. 日本鉱物科学会（JAMS）2019